

Spherical Individual Cell-Based Models

Limitations and Applications

Der Fakultät für Mathematik und Informatik
der Universität Leipzig
eingereichte

DISSERTATION

zur Erlangung des akademischen Grades

DOCTOR RERUM NATURALIUM
(Dr. rer. nat.)

im Fachgebiet
Informatik

vorgelegt
von Diplom-Physiker Axel Krinner

geboren am 11. November 1976 in München

Leipzig, den 3. Februar 2010

Contents

Abstract	v
Introduction	1
Bioinformatics and Systems Biology	1
Where Do the Data Come From? A Few Examples	3
Agent-Based/Individual-Based Modeling	9
Organization of the Thesis	10
1 The Spherical Cell Model	13
1.1 Background: The Biological Cell	13
1.2 One Cell and its Morphology	14
1.3 Interaction	14
1.3.1 The Hertz model: Elastic, repulsive forces	14
1.3.2 Adhesion energy	15
1.3.3 Total potential	16
1.4 Cellular Motion	17
1.4.1 Isolated cells	17
1.4.2 Cell populations	19
1.4.3 Friction	20
1.5 Cell Proliferation	20
1.6 Transport and Consumption	21
2 Migration and Related Phenomena	23
2.1 Cell Motion	23
2.1.1 Single cell motion	23
2.1.2 Cell populations	26
2.1.3 Discussion	29
2.2 Cell Sorting	31
2.2.1 Sorting and differential adhesion	31
2.2.2 Long-range attraction	32
2.3 Compression and relaxation	33
2.3.1 Experiment and theoretical model	33
2.3.2 Simulations	34
2.4 Discussion: Limitations of Spherical Models and Possible Applications	36

3	Modeling Oxygen-Dependent Expansion and Differentiation of Mesenchymal Stem Cells	39
3.1	Introduction	39
3.2	Modeling MSC Differentiation, Lineage Specification and Growth	41
3.2.1	Differentiation	41
3.2.2	Lineage commitment	41
3.2.3	Induction of a functional phenotype	42
3.2.4	Cell proliferation	43
3.2.5	Oxygen distribution	43
3.3	Results	43
3.3.1	Low oxygen tension increases colony forming potential of MSCs	43
3.3.2	Expansion at low oxygen tension increases the chondrogenic differentiation potential of MSCs	45
3.3.3	Short term exposure of MSCs to low oxygen tension mimics continuous expansion at these conditions	48
3.3.4	Low oxygen tension impairs MSC differentiation	49
3.4	Model Parameters and Robustness	49
3.5	Discussion	50
4	Individual Fates of Mesenchymal Stem Cells <i>in vitro</i>	55
4.1	Introduction	55
4.2	Simulation Strategy	56
4.3	Results	57
4.3.1	Monitoring individual cell fates	57
4.3.2	Regeneration of the population structure	58
4.3.3	Linking biomechanics and differentiation	59
4.3.4	Modeling the organization of the stem cell pool	60
4.4	Discussion	60
5	Differentiation, Aging and Senescence	63
5.1	Introduction	63
5.2	Experimental Results	64
5.2.1	Clonal heterogeneity of MSC <i>in vitro</i>	64
5.2.2	Spatial heterogeneity of MSC populations	66
5.3	Modeling Stem Cell Organization and Aging <i>in vitro</i>	66
5.4	Simulation Results	68
5.4.1	Spatial age-structure of MSC colonies <i>in vitro</i>	68
5.4.2	Functional heterogeneity of MSC <i>in vitro</i>	69
5.4.3	Aging of MSC <i>in vivo</i>	69
5.5	Discussion	71
6	Intracellular Processes: Wnt Signaling	73
6.1	Introduction	73
6.2	Background and Experiments	74
6.3	PDE System for Activator and Inhibitor	76
6.4	Individual Cell-Based Model for wnt Signaling	79
6.5	Results	86
6.5.1	Simulated concentric co-culture	86
6.5.2	Simulations of a random co-culture	89

6.6 Discussion	90
7 Conclusion	93
Acknowledgements	97
Appendix	99
A.1 Abbreviations	99
A.2 Details of Implementation	99
A.3 Materials and Methods	100
A.4 Simulation Parameters	104
A.4.1 Parameters used in Chapter 3	104
A.4.2 Parameters used in Chapter 4	105
A.4.3 Parameters used in Chapter 5	106
A.4.4 Parameters used in Chapter 6	107
List of Figures	108
List of Tables	110
Bibliography	111
Curriculum Vitae	129
Selbstständigkeitserklärung	131

Abstract

Over the last decade a huge amount of experimental data on biological systems has been generated by modern high-throughput methods. Aided by bioinformatics, the '-omics' (genomics, transcriptomics, proteomics, metabolomics and interactomics) have listed, quantified and analyzed molecular components and interactions on all levels of cellular regulation. However, a comprehensive framework, that does not only list, but links all those components, is still largely missing. The biology-based but highly interdisciplinary field of *systems biology* aims at such a holistic understanding of complex biological systems covering the length scales from molecules to whole organisms. Spanning the length scales, it has to integrate the data from very different fields and to bring together scientists from those fields. For linking experiments and theory, hypothesis-driven research is an indispensable concept, formulating a cycle of experiment, modeling, model predictions for new experiments and, finally, their experimental validation as the start of the new iteration.

On the hierarchy of length scales certain unique entities can be identified. At the nanometer scale such functional entities are molecules and at the micrometer level these are the cells. Cells can be studied *in vitro* as independent individuals isolated from an organism, but their interplay and communication *in vivo* is crucial for tissue function. Control over such regulation mechanisms is therefore a main goal of medical research. The requirements for understanding cellular interplay also illustrate the interdisciplinarity of systems biology, because chemical, physical and biological knowledge is needed simultaneously.

Following the notion of cells as the basic units of life, the focus of this thesis are mathematical multi-scale models of multi-cellular systems employing the concept of individual (or agent) based modeling (IBM). This concept accounts for the entity cell and their individuality in function and space. Motivated by experimental observations, cells are represented as elastic and adhesive spheres. Their interaction is given by a model for elastic homogeneous spheres, which has been established for analysis of the elastic response of cells, plus an adhesion term. Cell movement is modeled by an equation of motion for each cell which is based on the balance of interaction, friction and active forces on the respective cell. As a first step the model was carefully examined with regard to the model assumptions, namely, spherical shape, homogeneous isotropic elastic body and a priori undirected movement.

The model examination included simulations of cell sorting and compression of multi-cellular spheroids. Cell sorting could not be achieved with only short range adhesion. However, it sorting completed with long range interactions for small cell numbers, but failed for larger aggregates. Compression dynamics of multi-cellular spheroids was apparently reproduced qualitatively by the model. But in a more detailed survey neither the time scales nor the rounding after compression could be reproduced. Based on these results, the applications consistent with the assumed simplifications are discussed. One already established application is colony growth in two-dimensional cell cultures. In order to model cell growth and division, a two-phase model of the cell cycle was established. In a growth phase the

cell doubles its volume by stochastic increments, and in a mitotic phase it divides into two daughter cells of equal volume. Additionally, control of the cell cycle by contact inhibition is included in the model.

After examination of its applicability, the presented model is used for simulations of *in vitro* growth of mesenchymal stem cells (MSC) and subsequent cartilage formation in multi-cellular spheroids. A main factor for both processes is the oxygen concentration. Experimental results have shown, that i) MSC grow much better *in vitro* at low than at high oxygen concentrations and ii) the MSC progeny harvested from low oxygen culture produce higher amounts of the cartilage components aggrecan and collagen II in multi-cellular spheroids than the ones from high oxygen culture.

In order to model these processes, IBM was extended by a stochastic model for cellular differentiation. In this model cellular differentiation is captured phenomenologically by two additional individual properties, the degree of differentiation and the lineage or cell type, which are subject to fluctuations, that are state and environment dependent. After fitting the model parameters to the experimental results on MSC growth in monoclonal expansion cultures at low and high oxygen concentrations, the resulting simulated cell populations were used for initialization of the simulations of cartilage formation in multi-cellular spheroids. The model nicely reproduced the experimental results on growth dynamics and the observed number of functional cells in the spheroids and suggests the following explanation for the difference between the two expansion cultures: due to the stronger pre-differentiation found after expansion in high oxygen, the plasticity of these cells is smaller and less cell adopt the chondrogenic phenotype and start to produce cartilage. Moreover, the model predicts an optimal oxygen concentration for cartilage formation independent of expansion culture and a de-differentiating effect of low oxygen culture within 24h. Because all simulations comply with the concept of hypothesis-driven research and follow closely the experimental protocols, they can easily be tested and are currently used for optimization of a bioreactor for cartilage production.

Cell populations are composed of individual cells and regulation of population properties is performed by individual cell, but knowledge about individual cell fates is largely missing due to the problem of single cell tracking. The IBM modeling approach used for modeling MSC growth and differentiation generically includes information of each individual cell and is therefore perfectly suited for tackling this question. Based on the validated parameter set, the model was used to generate predictions on plasticity of single cells and related population dynamics. Single cell plasticity was quantified by calculating transition times into stem cell and differentiated cell states at high and low oxygen concentrations. At low oxygen the results predict a frequent exchange between all subpopulations, while at high oxygen a quasi-deterministic differentiation is found.

After quantifying the plasticity of single cells at low and high oxygen concentration, the plasticity of a cell population is addressed in a simulation closely following a regeneration experiment of populations of hematopoietic progenitor cells. In the simulation the regeneration of the distribution of differentiation states in the population is monitored after selection of subpopulations of stem cells and differentiated cells. Simulated regeneration occurs on the time scales estimated from the single cell transition times except the unexpectedly fast regeneration from differentiated cells in the high oxygen environment, which favors differentiation. The latter case emphasizes the importance of single outlier cells in such system, which in this case repopulate less differentiated states with their progeny.

In general, cell proliferation and regeneration behavior are influenced by biomechanical and geometrical properties of the environment e.g. matrix stiffness or cell density. Because in the model cells are represented as physical objects, a variation of friction is linked to cell

motility. The cultures of less motile cells become denser at the same size and the effects of contact inhibition of growth more pronounced. This variation of friction coefficients allows the comparison of cultures with varying degrees of contact inhibition regarding their differentiation structure and the results suggest, that stalled proliferation is sufficient to explain the well-known differentiation effects in confluent colonies.

In addition, the composition of the simulated stem cell pool was analyzed regarding differentiation. In contrast to the established pedigree models, where stem cell can only be produced by asymmetric division, this model predicts that most of the cells in stem cell states descend from progenitor cells of intermediate differentiation states.

A more detailed analysis of single cell derived clones revealed properties that could not be described by the model so far. First, a differentiation gradient was observed in larger colonies, that was the opposite of the one predicted by the model. Second, the proliferative activity turned out to depend not only on oxygen, but also to be a property of individual clones persisting over many generations. Because the relation slow growth/pre-differentiation also holds for single cell derived clones, the general model of differentiation is extended by another heritable individual property. Motivated by the decline of proliferation and differentiation in culture and the high metabolic and epigenetic activity during cell division, each division event is assumed to de-stabilize stem cell states. Consequently, in the model the cells age in terms of cell divisions determines the fluctuations in stem cell states and the environment the mean fluctuation strength.

Including this novel concept, that links aging to growth and differentiation dynamics, into the model reproduces the experimental results regarding differentiation gradient and persistent clonal heterogeneity. The spatial differentiation pattern can largely be explained by the spatio-temporal growth pattern of the mono-clonal cell assembly: cells close to the border of the cell assembly have undergone more cell divisions than those in the interior and therefore their stem cell states are less stable. Heterogeneity of single-cell derived clones depends on the age of the first cell in the clone. When the stem cell fluctuations equal the mean fluctuations strength, the proliferative activity passes a maximum at a certain age due to the destabilization of stem cell states. Thereafter the proliferative activity decreases, because more time is spent in non-proliferative differentiated states. Considering the number of divisions the cells have already undergone *in vivo* and after the initial expansion *in vitro*, it can be assumed that all cells have already passed this maximum. Interestingly, the model also predicts an optimal age for directed differentiation, when cells stably differentiate, but have not lost the required plasticity. According to the model, this clonal heterogeneity may be caused purely *in vitro*, but hypothetical simulation of *in vivo* aging yielded results consistent with experiments on MSC from rats of varying age.

Finally, the detailed molecular regulation mechanisms in a multi-scale tissue model of liver zonation was studied, in which the key molecular components were explicitly modeled. Hence, this model resolved the intracellular regulation in higher resolution than the above considered differentiation models which had summarized the intracellular control and differentiation mechanisms by a few phenomenological, dynamical variables. The metabolic zonation of the liver is essential for many of the complex liver functions. One of the vitally important enzymes, glutamine synthetase, (GS) is only synthesized in a strictly defined pattern. Experimental evidence has shown that a particular pathway, the canonical wnt pathway, controls expression of the gene for GS. A model for transport, receptor dynamics and intracellular regulation mechanism has been set up for modeling the spatio-temporal formation of this pattern. It includes membrane-bound transport of the morphogen and an enzyme kinetics approach to β -catenin-regulation in the interior of the cell. As an IBM this model reproduces the results of co-culture experiments in which two-dimensional ar-

rangements of liver cells and an epithelial liver cell line give rise to different patterns of GS synthesis. The two main predictions of the model are: First, GS-synthesis requires a certain local cell number of wnt releasing cells. And second, a simple inversion of geometry explains the difference between the specific GS pattern found in the liver and in the co-culture experiments.

Summarizing the results presented in this thesis, it can be concluded that properties such as the occurrence of memory effects and single cells pursuing fates far off the population average could be essential for biological function. Considering the role of single cells in many tissues, the use of individual based methods, that are able to take such effects into account, can be expected to be a very valuable tool for the problems of systems biology.

Publications and Submissions related to the work presented in this thesis

1. **Krinner, A**, Zscharnack M, Bader A, Drasdo D, Galle J (2009)
The Impact of the Oxygen Environment on Mesenchymal Stem Cell Expansion and Chondrogenic Differentiation.
Meeting Abstracts Bone-Tec 2008
Tissue Engineering A **15**(5): O13-O14
2. **Krinner A**, Zscharnack M, Bader A, Drasdo D, Galle J (2009)
Impact of the oxygen environment on mesenchymal stem cell expansion and chondrogenic differentiation. *Cell Proliferation* **42**: 471-484.
3. Galle J, **Krinner A**, Buske P, Drasdo D, Loeffler M (2009)
On the impact of single cell biomechanics on the spatio-temporal organization of regenerative tissue.
in World Congress on Medical Physics and Biomedical Engineering, September 7 - 12, 2009, Munich, Germany (ed. Olaf Dössel and Wolfgang C. Schlegel) IFMBE Proceedings 25/X: 185-188. Springer Heidelberg.
4. **Krinner, A**, Zscharnack M, Drasdo D, Galle J (2009)
Impact of oxygen environment on mesenchymal stem cell expansion & chondrogenic differentiation.
Meeting Abstracts World Conference on Regenerative Medicine, Leipzig, Germany.
Regenerative Medicine **4**(6): S111.
5. **Krinner, A**, Zscharnack M, Drasdo D, Galle J (2009)
Individual Fates of Mesenchymal Stem Cells *in vitro*.
Meeting Abstracts Combined Meeting of ESGCT, DGGT, ISCT and GSZ, 2009
Human Gene Therapy **20**(11): 1383.
6. **Krinner A**, Hoffmann M, Loeffler M, Drasdo D, Galle J.
Individual Fates of Mesenchymal Stem Cells *in vitro*.
BMC Systems Biology under revision.
7. **Krinner A**, Zscharnack M, Bader A, Drasdo D, Stolzing A, Galle J.
Lost in Translation - On the Heterogeneity of Mesenchymal Stem Cell Populations.
Submitted.
8. Galle J, Bader A, Grill W, Fuchs B, Käs JA, **Krinner A**, Müller K, Schiller, Schulz R, von Butlar, M, Löffler M.
Stem Cells in Cartilage Repair: State of the Art and Methods to monitor Cell Growth, Differentiation and Cartilage Regeneration.
Submitted (invited to *Current Medicinal Chemistry*).
9. **Krinner A**, Gehardt R, Drasdo D.
Modelling Regulation of Glutamine Synthetase by Wnt.
In Preparation.

Introduction

Bioinformatics and Systems Biology

Around the turn of the millennium the amount of information on biological systems started growing very rapidly. Genome projects for many different species ranging from viruses and bacteria to plants and mammals have been completed [1]. Sequencing uses only fragments of DNA and the question arises, how the sequence can be reconstructed from these fragments, how to assemble the genome. By computational methods the problem of genome assembly can be solved even for the amount of data produced by high-throughput sequencing. However, bioinformatical methods are not only applied for genome assembly, but also for many other problems related to sequence data. Only attaching biological information to a sequence makes it useful. This entails identifying known structures and predicting new elements. Additionally, information on evolution and phylogeny can be derived from genome comparison. Finally, all the data must be stored, managed and made accessible to queries. Indeed, many problems of bioinformatics are directly related to genomics, the study of the genomes, but high-throughput data and the related problems are produced by all other -omics, too [2]: transcriptomics studies the transcriptome, the set of all RNAs produced in a cell at a time, which in contrast to the genome is very dynamic. Proteomics addresses the proteome, the set of all proteins occurring in a cell, metabolomics the set of all metabolites with the sub-fields of sugars, lipids, amino acids and nucleotides and, finally, interactomics the interactions of molecules [3].

Despite the huge progress in acquiring data on many levels of molecular control, many aspects of the complex dependencies at the various levels of regulation remain unclear. In other words, as Kitano states: ‘Identifying all the genes and proteins in an organism is like listing all the parts of an airplane (... and) by itself it is not sufficient to understand the complexity underlying the engineered object’ [4]. All the molecular information is important and necessary for understanding the organization of the organisms made of these molecules, but the complexity, that emerges from their interaction, exists on a higher level of organization. An interdisciplinary research approach which combines biology with computer sciences, mathematics, systems theory and engineering sciences into one ‘systems biology’ is expected to make a major contribution to this understanding. Therefore the so-called discipline of *systems biology* pursues a holistic multi-scale approach and aims at developing close-to-reality models of physiological processes at all levels which have to be considered: molecules, cells, tissues and entire organisms (see Fig. 1).

An illustration of the length scales involved in this approach, which cover several orders of magnitude, is given by a carcinogenic mutation. The function of many important regulatory molecules depends on single amino acids. A mutation of a single nucleic acid in the gene for such a regulatory molecule may lead to unregulated, excessive growth and a tumor. The tumor itself damages surrounding tissue that is essential for the function of the affected

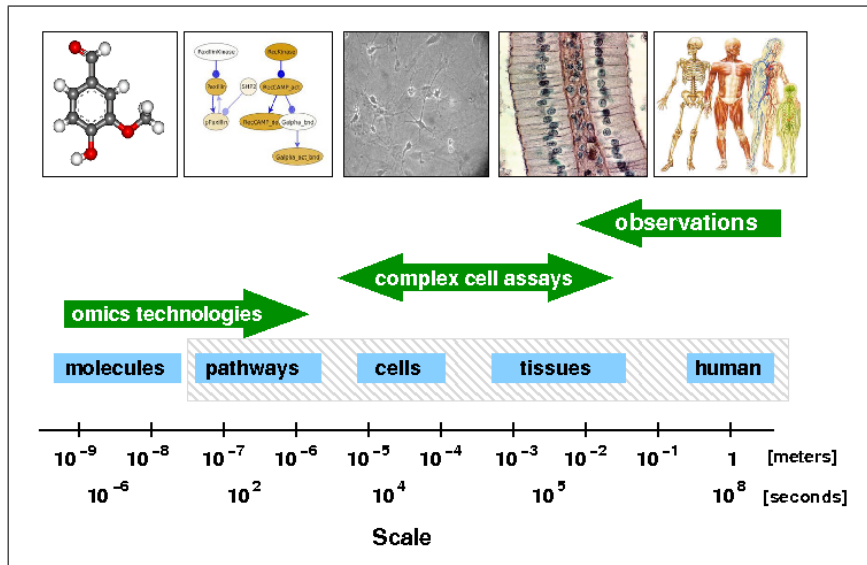


Figure 1: Length scales in Systems Biology The length scales addressed in Systems Biology stretch from nanometer scale over several orders of magnitude to meters. Molecular regulatory action as found in transcription or in single events within a pathway happens on the nanometer scale. Pathways themselves include a whole cascade of molecular events and, for example, connect the cell's surface to the nucleus. The cells themselves harboring these pathways have diameters of several micrometers. Their functional compounds, the tissues, stretch from micrometer to several centimeters to form organisms like a human body measuring up to meters.

organ. Decline of the function of an organ clearly affects the organism. Hence, a mutation on the sub-nanometer scale may propagate to the meter-scale of the whole organism (see Fig. 1). The notion of such relations makes systems biology to seek integration of all these levels into an understanding of the whole system. Approaches cover target prediction, e.g. of micro RNAs [5] and models for folding into functional structures [6, 7], models for *in vitro* cell colonies [8, 9] up to flux models for the metabolism of single organs [10] and compartment models for cell numbers and effects on the level of an organism [11].

An important aspect of systems biology is the close collaboration of modelers and experimentalists [12]. The concept of interactive hypothesis-driven research clearly defines this general request for experiment and theory to generate synergies (see Fig. 2, [4]). Experimental 'wet lab' procedures yield data used by the 'dry lab' for development of models that fit the data. *In silico* experiments with these models are used to generate predictions and new hypotheses. After the 'theoretical turn' the hypotheses are fed back to the 'wet lab world' and follow-up experiments are designed to test the models. Well designed experiments are able to evaluate the predictions and their results are used for a new iteration of the cycle. Thus, each of these goal-oriented iterations bundles efforts in 'wet' and 'dry lab' and yields more sophisticated experimental and theoretical concepts.

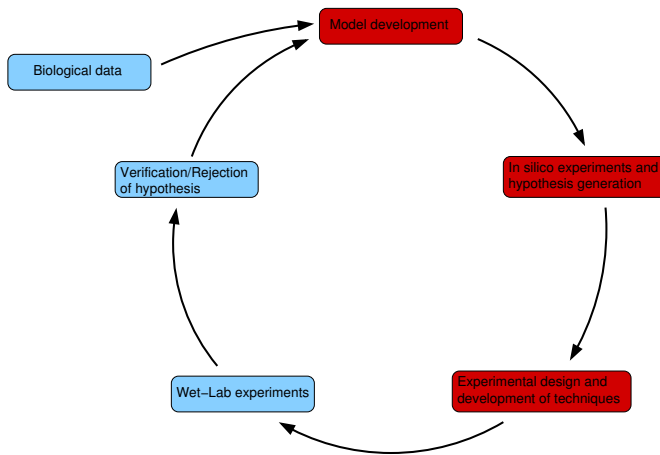


Figure 2: Iterative hypothesis-driven research A cycle of research includes alternating experimental (blue) and theoretical (red) efforts. Wet-Lab experiments generate data that are integrated into theoretical models. After fitting the model to the data it generates predictions and hypotheses. In the next step these predictions are used for designing a further experimental setup. The resulting experiment evaluates the hypothesis and initiates a new interactive cycle.

Where Do the Data Come From? A Few Examples

After unraveling the structure of the DNA molecular biologists have started to sequence and assemble genomes and annotate putative elements for a long list of species (see for example <http://www.ncbi.nlm.nih.gov>). This sequence data motivates projects like ENCODE (ENCyclopedia Of DNA Elements), which aims at identifying all functional elements in the human genome (<http://www.genome.gov/10005107>, [13]). The combination of sequencing and computational analysis has unraveled many aspects of biological regulation that remain to be integrated into a system-level understanding.

The most prominent group of the transcription-translation machinery, the proteins, provide vital function in metabolism, cellular structure and signaling. New experimental techniques like fluorescence correlation spectroscopy, fluorescence resonance energy transfer, circular dichroism spectroscopy, the engineering of small functional mutations and many additional method advances have produced an explosion of insight into protein dynamics, structure and, thus, specific function and their role in the organism ([6] and references therein).

The presence of proteins in a cell population has been probed since the 1980's by western blotting, an analytical technique using gel electrophoresis to separate the molecules and detect them with antibodies, even in activated phosphorylated states [14]. The disadvantage of this procedure is the averaging over many cells from one sample without the possibility to resolve information on single cell level or even sub-cellular localization. This problem is solved by the application of radioactive markers or staining dyes *in situ*. Techniques using radioactive markers are extremely sensitive, because almost every single disintegration can be detected and since every biologically relevant element is available as a radioactive isotope, they can be integrated into virtually every molecule, which can then be located by autoradiography. Disadvantages are the lack of flexibility compared to staining dyes and that the technique is not suited for high-throughput methods. In contrast, staining dyes highlight features of interest like proliferative activity by attaching dyes to related molecules, which subsequently can be detected (e.g. see [15]). Improvement of the staining technique is introduced by the use of fluorescent dyes, which substantially lower the signal-to-noise ratio. Different wavelengths of excitation (illuminating) and emission (detected) light allow detection of much smaller protein concentrations. Applied in confocal microscopy they even

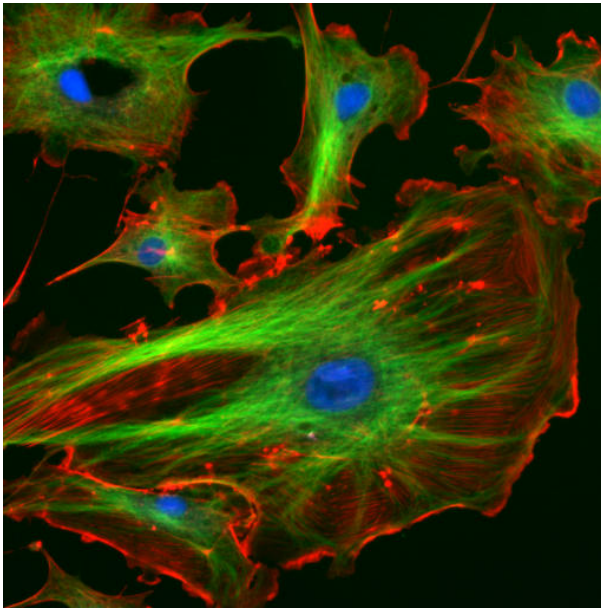


Figure 3: Fluorescence micrograph of endothelial cells. Nuclei are stained blue with DAPI, microtubules are marked green by an antibody bound to FITC and actin filaments are labeled red with phalloidin bound to TRITC. From WikiCommons.

allow *in vivo* imaging, as shown for bovine pulmonary artery endothelial cells in Fig. 3, and reconstruction of three-dimensional structures [16]. Fluorescence microscopy has also been applied by our experimental collaborators to detect commitment to the chondrogenic lineage in cell cultures derived from mesenchymal stem cells (MSC, see Chapter 3 and 5).

Another group of regulatory molecules, the RNAs made of ribonucleic acid, are considered increasingly important for cellular function. Their functions stretch from information transfer as messenger RNA (mRNA) over active participation in protein synthesis as transfer and ribosomal RNA (tRNA, rRNA) to regulation by non-protein-coding RNAs like implemented by microRNA (miRNA) and small interfering RNA (siRNA) post-transcriptional regulatory mechanisms. Employing the principle of RNA interference experimentally, allows transient knock-down of a target protein by inhibiting its translation and thus provides an important tool for studying protein function [17].

A more sophisticated method permits inducible and permanent gene knock-out in mice by site specific DNA recombination of the *loxP-Cre* recombination system. Introducing the binding sites (*loxP*-sites) for the recombination enzyme *Cre* up- and downstream of the knock-out gene in one mating partner and an inducible *Cre* gene with a cell type-specific promoter in the other yields inducible knock-out mechanisms in cells of defined types of the F1 generation [18,19]. After activation of the enzyme, it cuts out the target gene and causes a permanent knock-out [20]. In a similar way one can generate knock-ins, causing e.g. an over-expression or inducible constitutive expression of the desired protein. An example for the use of a knock-out system is given in the experimental results on liver zonation (see Chapter 6).

Biophysics has also contributed substantially to understanding tissue organization, since cellular function is directly related to physical properties. Measurements of elastic and adhesive properties of tissues and single cells by micropipette aspiration techniques [21], atomic force microscopy (AFM) [22], optical stretcher [23] or phase-sensitive acoustic microscopy [24] have revealed for example that some cancer cells and malaria infected red blood cells can be distinguished by their mechanical properties [25].

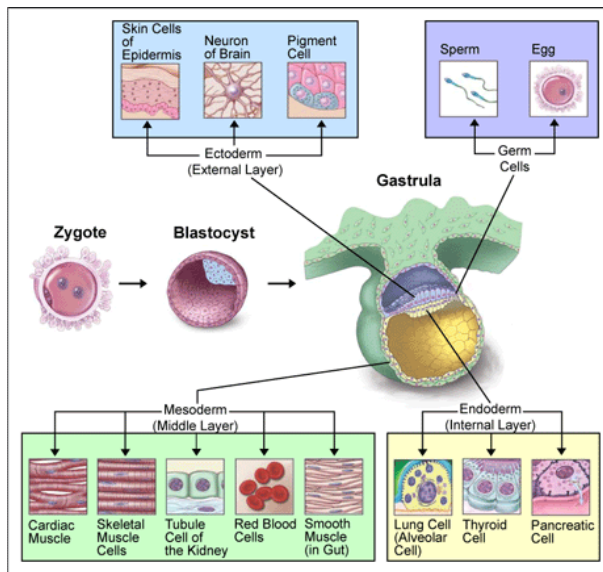


Figure 4: Cellular differentiation from the zygote to functional cells. During early development in mammals, the blastula is formed by the progeny of the proliferating zygote. During gastrulation the morphology of the embryo is restructured and the three germ layers are established. On top and bottom some of the fully differentiated cell-types arising from the germ layers are shown. From WikiCommons.

The combination of experimental techniques, computation, data storage and analysis has facilitated the generation of a huge amount of data. High-throughput experimentation, but also clinical studies of great extent have contributed considerably to this information pool, which remains to be fully understood and integrated. However, on the investigated length scales some basic entities of matter and modeling can be identified. Atoms and molecules are such entities of matter, while cells occupy a similar position in organs and organisms and, finally, individual organisms in ecosystems and society. In the following section the unique position of single cells regarding system-level understanding will be outlined.

Significance of Single Cells

Cells are the basic entity of life. The strongest evidence for this unique position is that all life is based on cells [17]. Although a vast variety of species exists, concerning the basic principles it does not matter if bacteria or mammals are considered. All cells use heritable genetic information, undergo metabolism to maintain homeostasis and follow the principle *Omnis cellula e cellula* (Every living cell comes from another living cell) by Rudolf Virchow [17, 26]. Especially for almost all metazoa the importance of a cell can be illustrated by reformulating Virchow's principle to *Every living organism comes from a zygote*. A zygote is produced by fertilization and combines the information of the two haploid germ cells. Thus, the moment of fertilization represents the first time the complete genetic information of the unique organism exists. During development the whole organism is produced from this first cell by cell division, cell death, differentiation and rearrangement processes. An adult human body is composed of some 10^{14} cells of about 210 cell types, arranged in the main organ systems like respiratory, circulatory and reproductive system (see Fig. 4). Despite their totally different shape and function, all these cells carry the same genetic program inside. This single global program gives rise to all the different cell fates. In close proximity, individual cells of very different types are found. For example, the function of the intestine depends on the amount of the mucus secreted by the goblet cells (Fig. 5). This mucus weakens chemical and shear stress and therefore the secreted amount of mucus

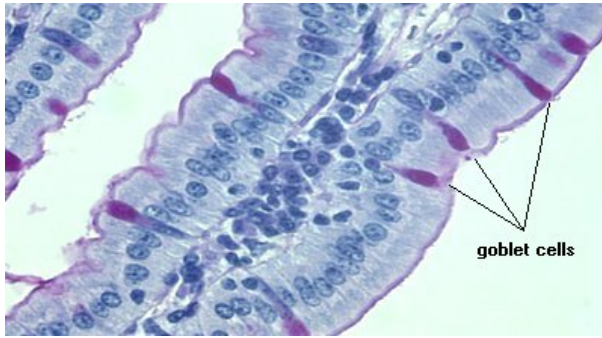


Figure 5: Goblet cells in the villus secrete the mucus that protects the absorptive cells from shear and chemical stress. Their fraction is precisely regulated and increases with the length of the intestine and the solidity of the digested food. This regulation is a nice example how important cellular properties are controlled at the length scale of individual cells. Reproduced from [27].

and the number of goblet cells depends on the intestinal position. Hence, the precise control of the density of goblet cells represents an example of functional cellular properties at the length scale of single cells, and highlights the role of the entity *cell*. But how do the cells take those important decisions on their fates?

Cellular fates Basically, each cell's fate can be seen as a sequence of cellular states. Cellular states can be seen from two different angles. First, one can focus on observations of the phenotype and have a closer look at the functional state of a cell. It is imprinted in the distribution of proteins necessary for a particular function. Therefore, an appropriate set of such proteins can serve as a marker system for a specific functional cell type. Currently such markers are frequently used to assess cellular function or malfunction. Examples used in Chapters 3 and 5 are markers of the chondrogenic lineage. Because aggrecan and collagen II are main components of cartilage, chondrocytes can be identified by probing these molecules [28]. Indicators for malfunction are the widely used cancer markers representing an important diagnostic tool [29]. However, to thoroughly understand the emergence of such functional phenotypes it is crucial to unravel the regulation leading to the production of these functional proteins.

This leads to the second notion of cellular state, the regulatory state, which is given by the abundance and localization of regulatory molecules like RNAs, transcription factors, silencers etc [17]. Part of this regulation are the epigenetic marks on histones and DNA, which recently attract increasing attention [30,31]. Quantifying the (co-)localization of all regulatory molecules and their state at once is impossible, but assessing some putative key molecules is indispensable for understanding regulatory mechanisms in the cell. Techniques for assessing the occurrence of these molecules for quantifying cellular states have been mentioned in the previous section and include various blotting techniques, molecule-specific histological and fluorescent staining for microscopy or immuno-precipitation (IP) [17,18].

On every stage the following development of the cell's state is determined by three main factors: the global program encoded in the DNA, the cell's present regulatory state and its environment. The DNA provides the global information on all cellular products and metabolism, and can be seen as the global and non-changing program [17,32]. The regulatory state is given by proteins, RNAs as well as other types of signaling and metabolic molecules, their state and localization. Note that this includes also the set of expressed genes and activation pattern of enzymes and signaling cascades [32]. Extending the view of the DNA as the global program, this second level would correspond to its state of execution. The third factor, the environment, is source and drain of raw material and waste, but also of information. One could call it in- and output of the biological program. The environment not only includes the chemical composition of the surrounding medium regarding nutrients,

oxygen and signaling molecules, but also geometrical and mechanical properties, like stiffness and assembly of the extra-cellular matrix (ECM) or properties of neighboring cells, which influence cellular fate decisions [33, 34].

Between the three factors, that determine cellular fates, are strong interdependences arising from cellular activities. The most obvious and general activity relating the three factors is metabolism. On one hand, metabolism uses the recipes of the DNA, the information on presently activated processes encoded by regulatory state and energy and chemical building blocks from the environment. On the other hand, the molecules, which are produced by metabolism, set the regulatory state and are released into the environment not only as waste but also as signaling molecules and ECM. Considering the close relation of regulation and metabolism and the weakening of the boundary between the global DNA program and epigenetics as part of the regulatory state ties the three factors together [35]. In general, the history of transcription and therefore preceding regulatory states is recorded by epigenetic marks and controls the activation of the global DNA program [36].

The Cell in its environment Of course, different functional cells need to fulfill different functional requirements. For example neurons and lymphocytes are very different cells. Neurons have to supply their stable structure for signal transduction, while lymphocytes function includes migration to the infected site and thus a very variable shape. Some elementary biological phenomena like cell sorting may even be reduced to purely physical processes. Foty *et al.* [37] claim that patterning processes of embryonic cells like envelopment of one cell type by another and cell sorting are solely governed by differential adhesion (see Sec. 2.2 and 2.4). Similarly, cellular orientation within multicellular aggregates may be explained by aligned distribution of cell-cell adhesion molecules on certain cell geometries [38, 39] and related biophysical cellular properties have been shown to affect tumor growth kinetics in simulation studies of a monolayer [9, 38]. But although these phenomena may be realized by physical effects involving unchanging cellular states, one has to keep in mind that these biophysical properties are subjected to cellular regulation.

In general, cells gather information about the biophysical properties of their environment by adhesion molecules like cadherins and integrins. Mechanical forces are transduced via the adhesion molecules into the cell's interior, where they serve as an input for regulation of cell adhesion and cytoskeletal reorganization. These systems therefore represent mechanosensors [40, 41]. The importance of this mechano-sensory view of a cell has been addressed by introducing the concept of cells as tensegrity structures [42]. By mechano-chemical transduction the mechanical signals sensed by the cell are translated and transferred into the regulation machinery as has been shown for coupling of focal adhesion complexes to extracellular signal-regulated protein kinase (ERK) pathway [43, 44]. Further examples for coupling mechanics to molecular regulation are reviewed in Discher *et al.* [45]. The spectrum of cellular responses to environmental stimuli covers all aspects of cell behavior: migration [46], differentiation [33, 47, 48], and cell death and proliferation [42] have been shown to depend on the biomechanical environment.

A very important function of differentiated cells is the generation of a specific environment. This environment includes in all tissues a varying content of extracellular matrix (ECM), whose function is not limited to providing a habitat. It also separates different tissues, bears stress and strain and contributes to transport and storage e.g. of growth factors. Most obvious is the ECM in tissues where matrix-cell ratio and mechanical stress are very high, like in bones, tendons and cartilage, but ECM is also present even in the brain or the spinal chords [17]. To guarantee a functional skeleton, in bone osteoblasts and osteoclasts are constantly remodeling their environment [49].

Another activity, that is also controlled by biophysical input as mentioned above is the cell migration. Cell migration occupies a unique position in development and homeostasis. Differentiation alone is not sufficient for establishing the immense complexity in mammalian bodies. Clearly the blueprint involves the development of cellular phenotypes carrying out specialized functions. But the precise assembly of these cells is essential for function and involves continuous rearrangement processes like gastrulation, neural tube closure or life-long wound healing and intestinal cell replacement ([17, 50] and refs. therein). Thus in addition to deciding which fate to adopt, the cells need to decide where to settle. How do the cells know which place to go to? Apart from mechanical stimuli cell motion can be triggered by chemical signaling [51].

In summary, cells do not only construct their environment and adopt their own properties according to a deterministic fate, but also the mechanical information on their environment serves as an input for the regulatory machinery of the cell. Thus, these complex interdependencies introduce a strong feedback, that a successful systems biology needs to understand in an interdisciplinary fashion.

Requirements for stability. The interdependence between regulatory state and environment could suggest, that environmental perturbations can spread into all areas of cellular organization and cause malfunction on all levels. Since formation of structures like tissues and organs, homeostasis and maintenance of function involves highly orchestrated cell behavior, the question arises how robustness can be achieved against the natural variability in conditions. Under varying conditions an exceedingly strict program, which lacks flexibility to compensate such variations, would produce very different outcomes and not the desired function. On the other hand unambiguous rules are necessary for establishing and maintaining the complex metazoan body architecture. Without abundant coordination, feedback and checkpoints such robustness cannot be realized [12]. Coordination, feedback and checkpoints require cell communication and intracellular processing of the transmitted information on all levels. Different strategies for cell-cell communication like hormones and nerves are found in even the simplest metazoan animals [52]. These means of communication are the most obvious and may already facilitate the feedback necessary for organism-wide regulation. Cell-matrix interaction may conceal many less obvious, but equally important feedback mechanisms, which may be hard to unveil, because communication processes are mainly studied by quantifying the response to a single stimulus introduced into the network or by blocking single channels of information flow. Since redundancy is another important concept in robust systems [12], this approach may not be sufficient to unveil the basic principles of organization in biological systems.

In the last paragraphs it became clear that the cells themselves control their development and integrate a variety of signals from their environment. These signals reflect environmental conditions outside the organism as well as cellular signaling over all distances within the organism [17]. Considering the number of signaling channels, cells must be understood as information processing agents. In order to guarantee survival of the organism they belong to, these agents need to cooperatively maintain physiological conditions even in an unfavorable environment and therefore aim at a global goal. To fulfill this task, they need to integrate and interpret the signals independently, each of them containing the recipe how to do so. In short, cells are:

autonomous. In principle each cell can survive outside the organism, as proven by *in vitro* experiments.

reactive. Cells adapt to their environment in many senses as discussed above.

proactive. Organization in procaryote colonies and multicellular organisms aims at the benefit of the cellular assembly.

Exactly these properties characterize the concept of agents in the field of computer science and modeling as will be shortly reviewed in the following section.

Agent-Based/Individual-based Modeling

After initially being used widely in ecological [53–55] and social sciences [56, 57] agent-based or individual-based modeling (IBM) has become a common method in biomedical research and bioinformatics [58, 59]. Although systems biology has its main focus on gene and protein interactions, system level understanding requires the understanding of multicellular organization with its feedbacks as discussed above. Hence it not only requires the modeling of the intracellular compartment, but also modeling that accounts for the cellular and multicellular level, since the cells not only receive and process information, but also generate it and spread it over many length scales. Therefore agent technologies and multi-agent systems constitute an emerging area in bioinformatics and systems biology.

A multi-agent system consists of autonomous, although reactive decision-making entities, the agents. Each agent individually assesses its situation and takes decisions on the basis of appropriate rules [60]. From these rules and the interaction of the agents complex phenomena can result, and being able to capture such *emergent phenomena* is one of the most important aspects of IBM [57]. The whole is more than simply the sum of its parts, and this simple statement is typical for biological systems. Typical indicators for the emergence of such complex behavior are the following [57]:

1. Individual behavior is nonlinear and can be characterized by thresholds, if-then rules, or nonlinear coupling. Describing discontinuity in individual behavior is difficult with differential equations.
2. Individual behavior exhibits memory, path-dependence, hysteresis, non-markovian behavior or temporal correlations, including learning and adaptation.
3. Agent interactions are heterogeneous and can generate network effects. Flow equations usually assume at least locally homogeneous mixing, but the topology of the interaction network can lead to significant deviations from predicted behavior.
4. Averages will not work. Differential equations tend to smooth out fluctuations. IBM does not, which is important because under certain conditions fluctuations can be amplified: the system may be linearly stable for small, but unstable to larger perturbations.

Each of these points is an essential feature of biological systems. Cell division is controlled by the cell cycle control system, which contains various check-points [17]. Positive auto-feedback is an essential tool for triggering developmental actions [61]. Epigenetic regulation imprints the cell's history on DNA organization [31]. Maintenance of a small population of stem cells represents a strong, but important heterogeneity in the adult organism [62], thus emphasizing the role of individual outlier cells.

Regarding cellular systems the IBM approach is intuitively closer to reality than differential equations. In contrast to widely used differential equations IBM can easily include

fluctuations on the scale of single cells. It also allows to assign different rules to different cells, to employ a varying number of cells and enables coarse graining by considering not only single agents but subgroups and aggregates with equal or similar properties [59]. In biological processes environmental conditions frequently change in space and time and the position of each individual cell may become crucial for decision making, for example in patterning processes such as the zonation of the liver (see Chapter 6, [59]). Therefore, the representation of cells as agents with a spatial representation can be expected to become crucial for modeling this sort of system. Finally, IBM permits to include stochastic fluctuations inherent in most biological processes and sometimes even necessary for certain outcomes (see Chapter 4). Summing up these advantages, IBM can be seen as the direct natural description of biological systems composed of many individual cells.

On long timescales evolution incorporates learning and problem solving as sought by the efforts in artificial intelligence. The variety in different ecosystems offers an inspiring wealth of dynamic solutions on all levels, from molecules to ecosystems. Considering this extent of individuality, it is not surprising, that ecology was the first discipline to adopt the IBM approach.

IBM has been formulated by Merelli as another level of software abstraction transcending methods, functions and objects as flexible problem-solving computational entities, which is formulated in the GeneWeaver project [58]. Already realized, more moderate applications of an agent based approach stretch from modeling cellular pathways [63] to tissue patterning [59] and stem cell analysis and simulation [64].

Motivated by the above discussion the model presented in this thesis follows the IBM philosophy. In contrast to many other realizations of IBMs on structured lattices [65–67] it is based on a spatial lattice-free representation of cells to avoid lattice-artifacts. Similar models have successfully been applied to:

- growth and pattern formation processes for epithelial cells under standard culture conditions [8, 68]
- growth of avascular tumors in suspension [9, 69, 70]
- spatial-temporal organization of regenerative tissue like in intestinal crypts [71, 72].
- morphogenesis like in blastulation and gastrulation [73].
- collective cell motion in the slime mold *Dictyostelium* [74–76].

Organization of the Thesis

The first chapter of this thesis introduces a basic individual-based model for biological cells that will be used throughout this thesis. The basic model is a biophysical model that mimics cells as homogeneous isotropic elastic spheres and includes cell-cell and cell-matrix interaction, cell motion, cell growth and diffusion of nutrients and oxygen. Additional modifications and extensions to the basic model presented in this chapter will be presented in the course of this thesis.

In the second chapter this model is applied to cellular motion, sorting of multi-cellular aggregates of different cell types and a biophysical compression experiment. The idea is to analyze to which extent this simple model of cells that neglects complex cell shapes and molecular control is already able to capture important multi-cellular observations. For modeling cellular motion, a representation of cellular filopodia replaces the random Langevin forces and in the section on cell sorting the purely contact-based Hertz model is an extended to longer interaction distances .

Oxygen-dependent *in vitro* growth and differentiation of mesenchymal stem cells (MSCs) are modeled in the third chapter. Mesenchymal stem cells are multipotent progenitor cells that persist in adult life and can form bone and cartilage. A noise-driven phenomenological model for differentiation is introduced and added to the biophysical IBM. It assigns the individual agents that represent the cells a state variable for differentiation. The emergence of functional chondrocytes, which are needed for cartilage production, is controlled by environmental information. After fitting the model to experimental data on cell proliferation, the observed differentiation behavior is reproduced with this set of parameters. Furthermore, it generates predictions on optimal culture conditions for maximizing cartilage production.

The individual-based modeling approach unfolds its potential in the fourth chapter by monitoring the fates of individual cells regarding differentiation dynamics. The analysis of individual cell fates generates the first predictions on *in vitro* MSC cell plasticity, regeneration dynamics of population structures regarding differentiation and the composition of the population's stem cell compartment. In contrast to the composition of the stem cell compartment, cell plasticity and regeneration of population structure are predicted to be closely related and to depend heavily on the environment.

A more detailed analysis of individual clones in MSC derived cell cultures reveals that growth and differentiation potential are persistent properties. The fifth chapter addresses this clonal heterogeneity, which is not captured by the stochastic differentiation model, by introducing an age related destabilization of stem cell states. Based on the results in three different species, this model for stem cell aging is used for modeling of spatial and clonal heterogeneities in MSC colonies. It predicts an optimal age for differentiation and, based on a few simple hypotheses even captures *in vivo* aging qualitatively.

Finally, in the last chapter a molecular pathway is included as a regulation mechanism into the individual cell based model. Activity of the enzyme Glutamine Synthetase (GS) is one indication of the zonation of the liver and controlled by the canonical wnt pathway. Wnt transport and signaling is modeled including receptor dynamics and intra-cellular regulation, the latter represented by an ODE based enzyme-kinetics approach. The model is applied to *de novo* glutamine synthetase induction *in vitro* and *in vivo*.

In the conclusion, the results are discussed regarding the importance of individual based modeling for biological, in particular multi-cellular systems.

1

The Spherical Cell Model

1.1 Background: The Biological Cell

The Latin word *cellula* means small room. It was an intuitive description of the functional unit of a biological cell chosen by Robert Hooke after studying cork with a microscope [77]. Exactly this separation of space addressed by *cellula* gives to the construct of a single cell its importance as the elementary unit of life. A cellular membrane divides space into the cell's interior and exterior. The interior harbors the whole metabolism of a cell and provides necessary conditions for processes like transcription, protein synthesis, cytoskeletal reorganization and signaling. The cell's exterior provides sources of e.g. nutrients necessary for the metabolic activity and information. Nutrients have to be transported into the cell, the cell needs to dispose waste, environmental information must enter the cell and signals be released into the environment. All these tasks are performed by trans-*membrane* proteins as gatekeepers for molecular traffic, receptors for molecular signals and adhesion molecules for cell attachment. These molecules, crucial for cellular functions, are situated within the membrane and guarantee the cell's interaction with it's exterior.

Besides metabolism cellular activities involve movement. Monocellular organisms search for nutrients, but multicellular ones cooperate in fascinating complex interactions involving orchestrated cell motion like in early embryonic development, wound closure and homeostasis [51]. Thus, cell motion has been the subject of intense studies of migration in populations as in the multi-cellular phases in the life cycle of *Dicytostelium* [78] or neural tube closure [50] down to the molecular basis of migration in focal adhesion sites [43].

All cellular actions including metabolism, attachment and migration finally aim at the main feature of life, self reproduction. A cell's fission into two daughter represents the only way to create new cells.

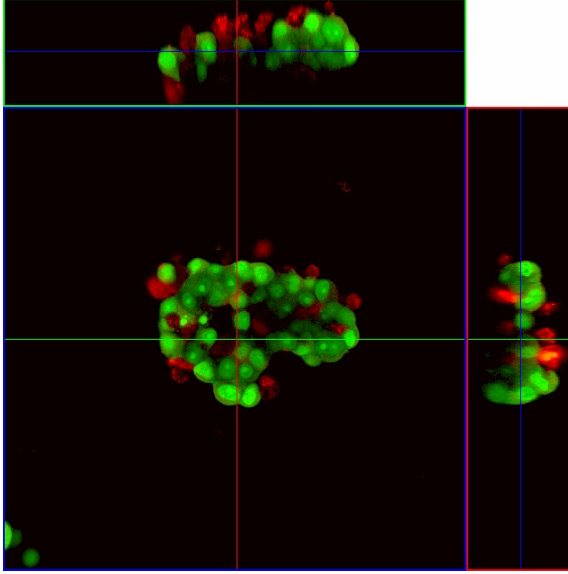


Figure 1.1: Spherical tumor cells in a hydrogel model system. In order to develop a three-dimensional model system for tumor metastasis in bone prostate tumor cells are cultivated in the hydrogel network. In the bio-compatible network they proliferate and form tumor spheroid without larger deviation from spherical cell morphology. Shown are confocal fluorescence micrographs of three sections in the planes indicated by the colored lines. With permission taken from [80].

1.2 One Cell and its Morphology

The surface tension of lipid vesicles makes them adopt a spherical shape like a bubble. Cells in suspension often do the same [79], but for biological function in an organism cells depend on the internal mechanical structures provided by the cytoskeleton. It is a general observation that for cellular polarity directional signals like e.g. extracellular contacts, chemotactic signals are required. If a cell happens to be in an environment lacking this kind of signals like suspension or multicellular aggregates it adopts an approximately spherical shape. In Fig. 1.1 this is shown in a fluorescence micrograph of prostate cancer cells cultivated in a hydrogel, which mimics the geometry of the bone marrow. This and other similar observations suggest to approximate the shape of a cell in isolation by a sphere. Hence a spherical cell shape is chosen for the model presented in this thesis. The simple spherical geometry allows to represent cells only by center position \vec{x}_i and radius R_i .

1.3 Interaction

Virtually all biological phenomena must be understood as the interplay of many cells in cooperating or competing relations. Cells deform under stress, may adhere to extracellular matrix or surfaces and may form multicellular tissues. As mentioned in the introduction, the cellular behavior depends to a great extent on the mechanical interactions with the environment, which makes these interactions crucial for modeling cellular aggregates. In the following the repulsive forces are modeled by the Hertz theory for deformation of spheres, which is used frequently in AFM labs to analyze the response of biomaterials [81, 82].

1.3.1 The Hertz model: Elastic, repulsive forces

The Hertz model provides expressions for the radius of the contact surface and the contact load at the normal contact of two elastic spheres [83, 84]. In the simulations contact areas

and contact forces determine the dynamics in each time step, and must be calculated for each cell contact. For two spheres i and j the model relates interaction force F to the radius r of the contact area and surface deflection δ by the analytic expressions [83, 84]:

$$r^3 = \frac{3}{4} \left(\frac{1 - \nu_i^2}{E_i} + \frac{1 - \nu_j^2}{E_j} \right) \frac{R_i R_j}{R_i + R_j} F. \quad (1.1)$$

$$\delta^3 = \frac{9}{16} \left(\frac{1 - \nu_i^2}{E_i} + \frac{1 - \nu_j^2}{E_j} \right)^2 \frac{R_i + R_j}{R_i R_j} F^2 \quad (1.2)$$

where ν_i denotes sphere i 's Poisson's ratios, E_i its Young's moduli and R_i its radii. The cellular radius R , Poisson's ratio ν and Young's modulus E are all experimentally measurable quantities. Typical values lie around $R = 5 - 10 \mu\text{m}$, $\nu = 0.4 - 0.5$ and $E = 400 - 2000 \text{Pa}$ [81, 85]. Given these quantities, the Hertz model allows to calculate the contact forces F and the radius of the contact areas r as a function of the cell positions for any two cells in contact ($\delta > 0$) from

$$r = \sqrt{\frac{R_i + R_j}{R_i R_j} \delta} \quad (1.3)$$

$$F = \frac{4}{3} \left(\frac{1 - \nu_i^2}{E_i} + \frac{1 - \nu_j^2}{E_j} \right)^{-1} \sqrt{\frac{R_i R_j}{R_i + R_j}} \delta^{3/2}. \quad (1.4)$$

Note, that sphere-plane interaction is given by the limit $R_j \rightarrow \infty$.

The simple form of the Hertz model comes at the cost of being based on several assumptions [86]. The material of the spheres in contact is assumed to be isotropic, homogeneous and linearly elastic, while the deformation must be small. Biological cells are neither isotropic nor homogeneous and highly non-linear in their elastic behavior [87], but for processes on a certain time scale and for small deformations the approximation by the Hertz model is reasonable. Of course, this imposes limitations for the applicability of the model, which will be discussed in appropriate context in Chapter 2, but the fact that the growth behavior of cell populations does not depend on the details of the interaction [88] supports its application.

1.3.2 Adhesion energy

In tissues and multicellular aggregates cells are tied together by cell-cell or cell-matrix contacts mediated by adhesion molecules like cadherins, integrins or ephrin and its receptor [89, 90]. To model cell adhesion the distribution of surface molecules on the cell membrane is assumed to be homogeneous. This approximation, which averages over variations in the surface density of adhesion molecules like in focal adhesions, allows to model the adhesion energy of a contact $V_{\text{adh},ij}$ proportional to the contact area A_{ij} . The constant of proportionality is given as $\epsilon_{ij} = \min(\varrho_i, \varrho_j) V_{\text{sb}}$, subsuming the number of matching adhesion molecules in the contact area due to dimerization as the minimum of their surface densities on both cells and the binding energy of a single dimer V_{sb} . The adhesion energy of a contact of two cells i and j is therefore given by

$$V_{\text{adh},ij} = -\pi \epsilon_{ij} \frac{R_i R_j}{R_i + R_j} \delta. \quad (1.5)$$

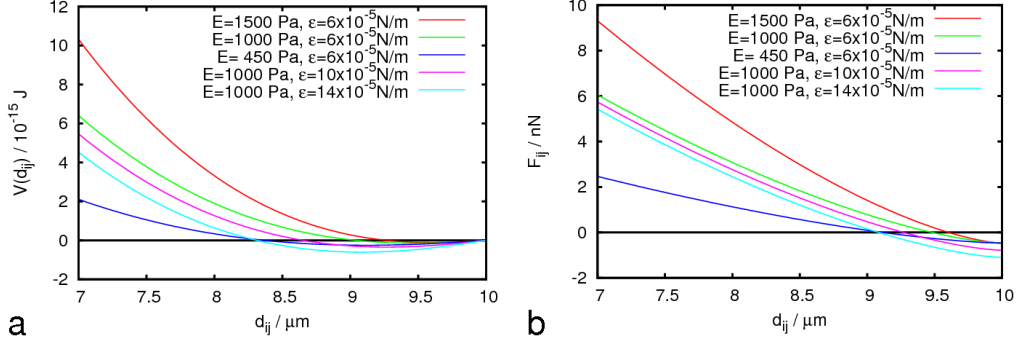


Figure 1.2: Modified Hertz Potential and Derived Force for some parameters used in the simulations. a) Shown is the modified Hertz potential V_{mod} as a function of cell-cell distance for two equal cells of radius $R = 5 \mu\text{m}$, Poisson's ratio $\nu = 0.4$, adhesion energy of $\epsilon_{ij} = 60, 100, 140 \times 10^{-6} \text{ N/m}$ and Young's Moduli $E = 450, 1000, 1500 \text{ Pa}$. b) The force F_{ij} derived by differentiation for the same parameter. The equilibrium distance is given by the root and lies around a relative deformation of 5-10%.

The strength of adhesion is given by ϵ_{ij} and depends on the cells in contact, more precisely on the cells' surface densities of adhesion molecules. Moreover it includes the contributions of several distinct adhesion molecules, each existent as ligands and receptors. However, this calculation of the adhesion energy implies that contact area can be approximated by the Hertz model. Often, adhesion increases the contact area at a given distance. This contribution is taken into account in the Johnson-Kendall-Roberts (JKR) model which moreover includes a hysteresis behavior. In the JKR-model cells detach at a larger distance than the distance at which they come into contact. However, as shown in Drasdo *et al.* [88] for simulation of growing monolayers, the modified Hertz model used in this thesis and the JKR-model yield very similar results.

1.3.3 Total potential

To obtain the full potential Eq. (1.4) is integrated to the interaction potential and the adhesive term given by Eq. (1.5) is added:

$$\begin{aligned}
 V_{\text{mod}} &= V_{\text{Hertz}} + V_{\text{adh}} \\
 &= \frac{8}{15} \left(\frac{1 - \nu_i^2}{E_i} + \frac{1 - \nu_j^2}{E_j} \right)^{-1} \sqrt{\frac{R_i R_j}{R_i + R_j}} \delta^{5/2} - \pi \epsilon_{ij} \frac{R_i R_j}{R_i + R_j} \delta.
 \end{aligned} \tag{1.6}$$

The interaction force entering into the equation of motion introduced below is derived by partial differentiation of the total potential V_{mod} with respect to the space coordinates x , y and z . For the radial symmetry, the interaction force acts in direction of the center-to-center unit vector with a modulus given by the derivative of Eq. (1.6) with respect to the deformation δ .

$$F = \frac{4}{3} \left(\frac{1 - \nu_i^2}{E_i} + \frac{1 - \nu_j^2}{E_j} \right)^{-1} \sqrt{\frac{R_i R_j}{R_i + R_j}} (R_i + R_j - d_{ij})^{3/2} - \pi \epsilon_{ij} \frac{R_i R_j}{R_i + R_j}. \tag{1.7}$$

For some parameter E and ϵ used in following simulations the potential V_{mod} and the derived force F are shown in Fig. 1.2. The adhesion parameter ϵ was chosen in accordance



Figure 1.3: Trajectory of a hematopoietic CD133+ cell. A hematopoietic CD133+ cell is followed over 4h in a culture dish. Shown is the trajectory of its geometric center of gravity. The outline of the moving cell is shown every 17 min. The resulting pattern of motion is strongly reminiscent of a Brownian particle.

to Frisch and Thoumine [91] in order to set the equilibrium distance at about 5-10% relative deformation. Eq. (1.3) and Eq. (1.7) are used for calculation of the contact area and the force, respectively, both as function of the center-to-center distance $d_{ij} = R_i + R_j - \delta$.

1.4 Cellular Motion

1.4.1 Isolated cells

In absence of external signals many migratory active cells exhibit a random walk-like behavior similar to Brownian motion [92, 93]. An example for the reminiscence of Brownian motion is shown by the trajectory of a hematopoietic CD133+ cell in Fig. 1.3. The main difference between Brownian motion and cell motion is that Brownian motion is a passive process, but cells are living and actively moving objects. And they do differ slightly from the thermally driven process of Brownian particles. As shown by Dieterich *et al.* [94] for kidney cells driven by an unknown mechanism different from inertia they exhibit at short time scales an exponent $\beta(t)$ of the mean square displacement (MSD) $\langle \Delta x^2 \rangle \propto t^{\beta(t)}$ smaller than in the ballistic regime of a Brownian particle. At long time scales, where the MSD for Brownian motion is linear in time, $\beta(t)$ decreases to ~ 1.3 . Considering the relatively short distances (about their own diameter) the cells move within a couple of hours the small deviation from Brownian motion motivates a Brownian particle modeling approach. The Brownian motion model has also been applied to living cells, and the diffusion coefficient used for quantifying cellular motion [92]. A very intuitive approach to Brownian motion has been proposed by Langevin in 1908, which is presented here in some detail [95].

The Langevin equation

The Langevin equation in absence of external forces reads as follows:

$$m \frac{d}{dt} \dot{\vec{x}} = -\gamma \dot{\vec{x}} + \vec{F}^{\text{stoch}}(t), \quad (1.8)$$

where m is the particle mass, \vec{x} its position, γ its friction coefficient and \vec{F}^{stoch} a stochastic force of modeling the random collisions of a Brownian particle with the liquids molecules. Using the equipartition theorem for f degrees of freedom at a thermal energy $k_B T$

$$\left\langle \frac{1}{2} m \dot{\vec{x}}^2 \right\rangle = \frac{f}{2} k_B T \quad (1.9)$$

and the postulate of uncorrelated random forces acting on the particle

$$\left\langle \vec{F}^{\text{stoch}}(t) \right\rangle = 0, \quad (1.10)$$

finally one obtains the solution for the mean square displacement:

$$\langle x^2 \rangle = \frac{2fk_B T}{\gamma} \left[\left(t - \frac{m}{\gamma} (1 - e^{-(\gamma/m)t}) \right) \right], \quad (1.11)$$

where f is the number of degrees of freedom and $k_B T$ the thermal energy at temperature T . In the long time limit $t \gg \gamma/m$ the solution yields with the corresponding diffusion coefficient $D = k_B T / \gamma$ and only considering translational degrees of freedom the well known result for the mean square displacement:

$$\langle x^2 \rangle = 2dDt. \quad (1.12)$$

Microorganisms and cells are subject to large friction compared to forces of inertia. As soon as they do not actively move they stall. This is reflected in a very low Reynold's numbers of $R \approx 10^{-5}$ which relates the forces of inertia to friction. A very low Reynold's number allows to neglect inertia and to simplify Eq. (1.8) to

$$\gamma \dot{\vec{x}} = \vec{F}^{\text{stoch}}(t). \quad (1.13)$$

In order to perform simulations a recipe is needed to quantify the random force in the equation of motion (1.13). For multi-cellular systems cell-cell interaction forces and contact-dependent friction have to be included (see below).

Random forces: Langevin noise as cell activity

Numeric integration of Eq. (1.13) requires a discretization of time. To derive the consistent stochastic force Eq. (1.13) is considered for time step $t_{i-1} \rightarrow t_i = t_{i-1} + \Delta t$ and associated displacement Δx_i :

$$\gamma \frac{\Delta \vec{x}_i}{\Delta t} = \vec{F}_i^{\text{stoch}}. \quad (1.14)$$

With the assumption of uncorrelated noise $\left\langle \vec{F}_i^{\text{stoch}} \vec{F}_j^{\text{stoch}} \right\rangle = c \delta_{ij}$, where c is a constant to be determined, summing over n time-steps and averaging the squared displacement yields

$$\langle (\Delta x(n\Delta t))^2 \rangle = \frac{\Delta t}{\gamma^2} n \Delta t \left\langle \left| \vec{F}^{\text{stoch}} \right|^2 \right\rangle. \quad (1.15)$$

Requiring $\langle \Delta x^2(t) \rangle = 2fDt$ and comparing coefficients gives a relation for the discrete random forces that depends on the time step Δt :

$$\left\langle \vec{F}_i^{\text{stoch}} \vec{F}_j^{\text{stoch}} \right\rangle = \frac{2dD\gamma^2}{\Delta t} \delta_{ij}. \quad (1.16)$$

This result is used in the simulations. Since Gaussian distributed random numbers obey

$$\langle X_i X_j \rangle = \sigma^2 \delta_{ij}, \quad (1.17)$$

one concludes from Eq. (1.16) to use random forces in d dimensions, which are equally distributed in direction and have a modulus drawn from a Gaussian distribution of variance

$$\sigma^2 = 2d\gamma^2 D / \Delta t \quad (1.18)$$

This approach relates the three quantities cellular friction γ (for a spherical cell in suspension Stokes friction $\gamma_{\text{Stokes}} = 6\pi\eta r$), cellular diffusion coefficient D_{cell} and the stochastic forces \vec{F}^{stoch} representing the active motility of the cell. If the cell is not floating in an aqueous environment, but is attached to some substrate, cell motion always involves rupture and formation of binding sites established by surface molecules like cadherins and integrins. During cell motion, new attachment sites called focal adhesions are formed at the leading front, which are used to pull the cell forward. They persist until they are released at the back [43]. Therefore surface attachment allows the cell to move, but also to resist being pushed. Thus, surface attachment affects both, active and passive forces. If a biological cell is subject to a mechanical stimulus, it is neither purely pushed away nor does it move in this direction without the stimulus. Active and passive motion are hard to separate. This tight relation of friction and active and passive motion is reflected by the dependence of the stochastic forces on cellular friction, and should be kept in mind when using such an Langevin approach to cell motion.

In summary, motion of an isolated cell is modeled by solving Eq. (1.14) with random forces obeying Eq. (1.18). The simulation parameter mainly controlling cell motility is the cellular diffusion coefficient D_{cell} , but into calculation of the Langevin forces in the equation of motion enter also the cell radius R_{cell} , the cellular friction coefficient γ and the time step Δt . Typical cellular diffusion coefficients are of the order $\approx 5^{-16} \text{m}^2/\text{s}$.

1.4.2 Cell populations

In populations cells interact touching, compressing, pushing, but also adhering, pulling and dragging. Regarding the equation of motion, these interactions can be grouped into forces caused by an interaction potential and friction. Both kinds of interaction require cells to be in contact and enter as additional coupling terms the equation of motion Eq. (1.14), which for cell i now reads:

$$(\Gamma_i^{\text{cs}} + \gamma_i^{\text{cm}})\dot{\vec{x}}_i + \sum_{\langle i,j \rangle} \Gamma_{ij}^{\text{cc}}(\dot{\vec{x}}_i - \dot{\vec{x}}_j) = \vec{F}_i^{\text{cs}} + \sum_{\langle i,j \rangle} \vec{F}_{ij}^{\text{cc}} + \vec{F}_i^{\text{stoch}}, \quad (1.19)$$

where both sums run over all cells j in contact with cell i . \vec{F}_i^{cs} , \vec{F}_{ij}^{cc} and \vec{F}_i^{stoch} are the interaction forces with the substrate and cell j and the stochastic Langevin force, respectively. γ_i^{cm} is the friction coefficient of the cell in a medium and a scalar, while Γ_i^{cs} and Γ_{ij}^{cc} are 3×3 matrices and separate tangential and radial components of movement by different friction constants γ_t and γ_r , respectively:

$$\Gamma_{ij} = (\gamma_r - \gamma_t)(\vec{r}_{ij} \otimes \vec{r}_{ij}) + \gamma_t \mathbf{1}, \quad (1.20)$$

where \vec{r}_{ij} is the center-to-center vector between cells i and j . For $\gamma_r = \gamma_t$ the calculation of friction forces simplifies to a scalar multiplication $\gamma \dot{\vec{x}}$. Distinction between friction of radial and tangential motion leads to a more complex system of linear equations and to dramatic

much slower simulation performance. Thus, this simple case was used in all presented simulations. Using a finite time step Δt in the simulations this yields a system of linear equations for the displacements $\Delta \vec{x}_i$:

$$(\Gamma_i^{\text{cs}} + \gamma_i^{\text{cm}})\Delta \vec{x}_i + \sum_{\langle i,j \rangle} \Gamma_{ij}^{\text{cc}}(\Delta \vec{x}_i - \Delta \vec{x}_j) = \Delta t \left(\vec{F}_i^{\text{cs}} + \sum_{\langle i,j \rangle} \vec{F}_{ij}^{\text{cc}} + \vec{F}_i^{\text{stoch}} \right). \quad (1.21)$$

1.4.3 Friction

In a cellular aggregate friction is the quantity relating force to displacement. As in Eq. (1.18), friction is related to active movement. Cells respond to a force, a mechanical stimulus, by crawling away. According to the relation active motion-passive motion mentioned above, the forces occurring in Eq. (1.21) can be interpreted as mechanical stimuli that initiate active cellular motion. A more motile cell as a larger diffusion constant in the same medium in which a less motile cell has a smaller diffusion constant. This again links active motion to the physically passive friction in the model. As for the adhesion energy, the surface distribution of adhesion molecules causing friction is assumed to be homogeneous and, thus, the friction coefficient γ_{cx} to be proportional to the contact area A_{ix} of a cell with another surface:

$$\gamma_{ix} = \eta_{ix} A_{ix}, \quad (1.22)$$

where ix denotes the type of contact, i.e. medium, substrate or cell and η_{ix} the contact type-dependent friction constant. A_{ix} is calculated from its radius r given by Eq. (1.3). Thus already an intrinsic dependence on the compression force is included.

1.5 Cell Proliferation

The cell cycle is the course of events that a cell passes between two successive divisions. This process requires to duplicate the DNA, and to provide each daughter cell with a copy of the DNA after division. The DNA is duplicated in S phase (S for synthesis) and after S phase chromosome segregation and division occurs in M phase (M for mitosis). But the cell needs also to double all other components before dividing again, which is done in the gap phases, G_1 between M and S, and G_2 between S and M. G_1 , S and G_2 phase are also termed the inter-phase [17]. Depending on external conditions like nutrient supply, cell density or other factors, many cells do not divide for a long time. They enter a quiescent resting state called G_0 . In fact many functional differentiated cells do not proliferate any more and stay in G_0 .

In the model the cell cycle is divided in inter-phase and M phase. During inter-phase, a cell doubles its volume by stochastic increments, and during the mitotic phase, a cell divides into two daughter cells of equal volume (Fig. 1.4). It has been shown that this growth process results in an approximately Γ -distributed growth time of the cells with a certain population average [9]. The population average of the growth time τ can easily be measured *in vitro* and used as an input for the simulations. For example the growth time in Chapter 3 is found to be for a fast growing clone ~ 12 h. The cell cycle length distribution can be measured by cohort experiments using radioactive thymidin [96].

Normal cells stop proliferation if they grow to a confluent monolayer. This is termed ‘contact inhibition of growth’. At high cell densities proliferation stops and cells enter the quiescent state G_0 . Here this effect is modeled similar to [88]. A cell undergoes growth

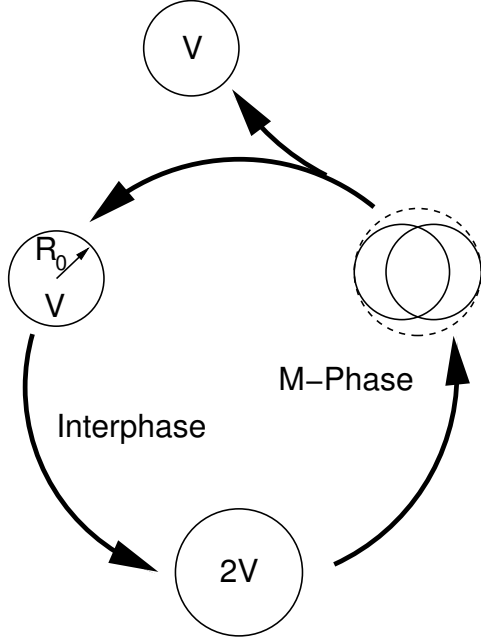


Figure 1.4: Cell cycle in the model. Subsuming S phase and the gap phases G_1 and G_2 it is assumed that a cell doubles its volume during the interphase. Afterward it divides into two daughter cells of identical volume inheriting all properties, e.g. elasticity and differentiation.

arrest if the sum of the deformation forces on it exceeds a critical value F_c :

$$\sum_{\langle ij \rangle} |\vec{F}_{ij}| + |\vec{F}_{is}| > F_c, \quad (1.23)$$

where the sum runs over all neighboring cells j . F_{ij} and F_{is} denote the contact forces exerted on cell i by a cell j and the substrate s , respectively.

1.6 Transport and Consumption

Nutrients like glucose, oxygen and signaling molecules are of essential importance for all cellular processes. In non-vascularized cell aggregates like avascular tumor spheroids the lack of nutrients causes a necrotic core beyond a certain tumor size [9], in mesenchymal stem cell culture oxygen heavily influences cell fate regarding differentiation [97] (see Chapter 3). The same accounts for the wnt signaling molecule and its inhibitor Dkk, which are studied in the context of liver zonation in Chapter 6. All three chemical species, oxygen, wnt and Dkk are transported by diffusion in these systems. If oxygen is available, it is consumed by the cells at a constant rate C , which leads to a radial oxygen gradient in the cell aggregates, which impacts cellular behavior. the oxygen gradient can be calculated by solving the reaction-diffusion equation

$$\partial_t c(\vec{x}, t) = D\Delta c(\vec{x}, t) - Cn(\vec{x}, t), \quad (1.24)$$

where $c(\vec{x}, t)$ represents the oxygen concentration of the considered substance, D its diffusion coefficient, C the consumption rate per cell and $n(\vec{x}, t)$ the cell density.

Another application of a reaction-diffusion equation, that involves more complicated processed is given in Chapter 6. The morphogenes wnt and Dkk are not consumed, but are produced by the cells, bind and unbind to surface receptors and degraded.

2

Migration and Related Phenomena

2.1 Cell Motion

Cellular motion is modeled according to Langevin's approach to Brownian particles. This fundamentally implies that the cells migrate by anchoring in a substrate (Petri dish or ECM). In the following section the results for an isolated cell driven by Langevin forces and an alternative approach are compared. The alternative approach generates forces by a representation of cellular filopodia. Both approaches are applied within cell populations. It turns out that two qualitatively different interpretations in multicellular systems are possible.

2.1.1 Single cell motion

Langevin equation

Simulations of the motion of an isolated cell in two and three dimensions were performed using Eq. (1.18) and the cell's position was recorded in each time step. In the simulations the cell performs a perfect random walk as shown exemplary by a trajectory in two dimensions over ≈ 1.4 h in Fig. 2.1a. To compare the results to theory, the mean square displacement was calculated for the total displacement and additionally for all three coordinates x , y and z in a sliding window approach from the time series of positions. Fitting the theoretical mean square displacements $\langle \Delta r^2 \rangle = 2dDt$ of Brownian motion to the resulting data reproduced the diffusion constant D in all considered cases and served as a self-consistency check (Fig. 2.1b-d). A vanishing mean displacement $\langle \Delta r \rangle = 0$ holds for all directions as implicated by the assumption of uncorrelated noise. The distribution of the stochastic forces representing the noise, which were generated in the 2D simulation is shown below in Fig. 2.4a. The small cellular diffusivity $D = 1 \times 10^{-16} \text{m}^2/\text{s}$ was chosen in the same order of magnitude as found for aggregates of embryonic cells by Mombach *et al.* [92]. For simulations on a substrate three-dimensional random forces were generated according to Eq. (1.18) and substrate adhesion ϵ was chosen to avoid loss of contact. Due to restriction of motion to the plane of substrate the results for the simulation reproduce the 2D scenario. This scenario demonstrates, that although the friction coefficients and therefore the noise amplitudes vary with the contact area to the plane, the relation friction-forces of Eq. (1.18) yields consistent results with the theory of Brownian motion.

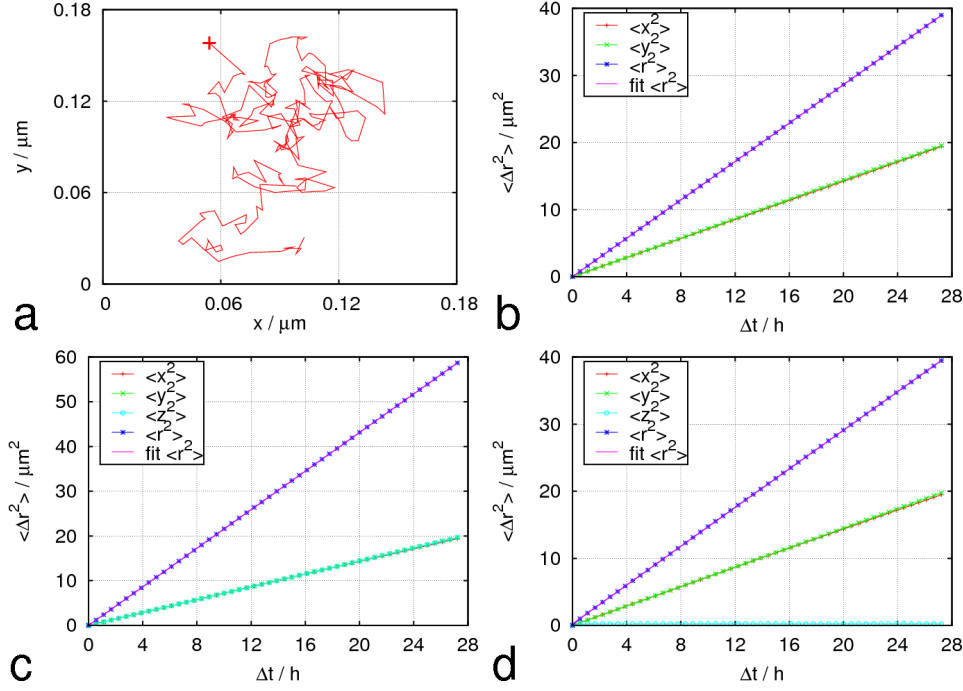


Figure 2.1: Characteristics of simulated Single Cell Motion. a) In the model a single cell performs a perfect random walk as shown exemplary by the trajectory in two dimensions covering $\approx 1.4\text{h}$ (cellular diffusion coefficient $D = 1 \times 10^{-16}\text{m}^2/\text{s}$, cell radius $R = 5\mu\text{m}$, medium viscosity $\eta = 10^3\text{Ns}/\text{m}^2$, time step $\Delta t = 20\text{s}$). b)-d): The resulting mean (square) displacements are in good agreement with $\langle \Delta r^2 \rangle = 2dDt$ as shown by linear fits for simulations in b) 2D, c) 3D, d) 3D, but on a flat substrate. The diffusion coefficient is reproduced and displacements in the spatial directions are equal as expected for uncorrelated motion, if no constraint, e.g. a substrate is present. The simulation on a substrate shows that consistent results are also produced for varying random forces due to changing substrate friction.

Filopodia

Attached to a substrate surfaces, migratory cells move by protrusions called lamelli- and filopodia. They develop focal adhesion sites in the protrusions, pull the cell body over them and release the focal adhesion sites at the rear. In order to study, if the direct implementation of the migration mechanism instead of phenomenologically mimicking active random movement by a Langevin force, a representation of filopodia was introduced into the model. We assume in our model that each cell has a fixed number of filopodia N_{filo} represented by random radial vectors emerging from the cells surface similar to Fig. 2.2. Their length l is Gaussian distributed around an mean length l_0 with a variance σ_l .

As filopodia need to be attached on the substrate filopodia are restricted to 2D and their direction is uniformly distributed in $[0, 2\pi)$. Hence the probability distribution for angle and length are

$$p(\phi) = \frac{1}{2\pi}. \quad (2.1)$$

$$p(l) = \frac{1}{\sqrt{2\pi\sigma_l^2}} e^{-\frac{(l-l_0)^2}{2\sigma_l^2}}. \quad (2.2)$$

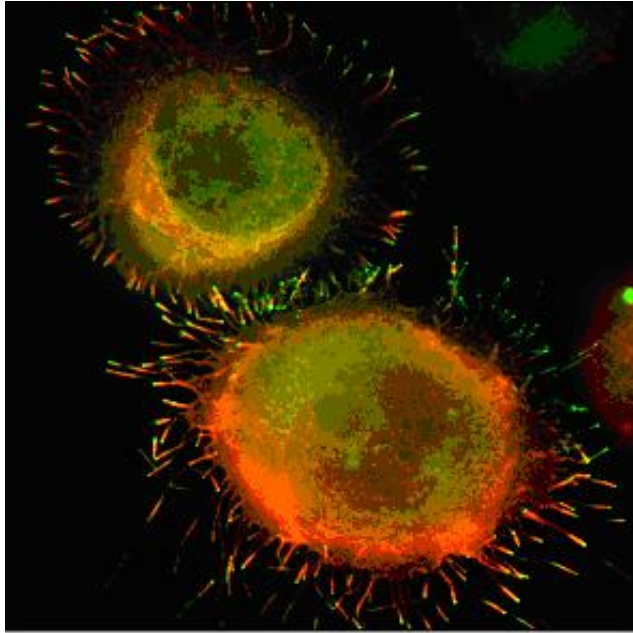


Figure 2.2: Filopodia of Macrophages. From WikiCommons.

For simplicity adhesion molecules are assumed to be uniformly distributed along the filopodia. The force F_{filo} assigned to a filopodium, which is attached to the substrate, is therefore proportional to its length l_{filo} :

$$F_{\text{filo}} = c l_{\text{filo}}, \quad (2.3)$$

where the constant of proportionality c is related to the average width, adhesion molecule density and the force of rupture of a single bond. Filopodia are sensitive extension of the cell and gather information on the environment. Because no relevant information can be obtained by a filopodium attached to the substrate, the filopodia are assumed to be newly formed in each simulation step, seeking for information. Therefore, the persistence of the filopodia is exactly one time step. The force entering into the equation of motion Eq. (1.14) instead of the Langevin force is the sum of forces of all individual filopodia, because here no filopodium is preferred by an environmental clue e.g. contact to another cell.

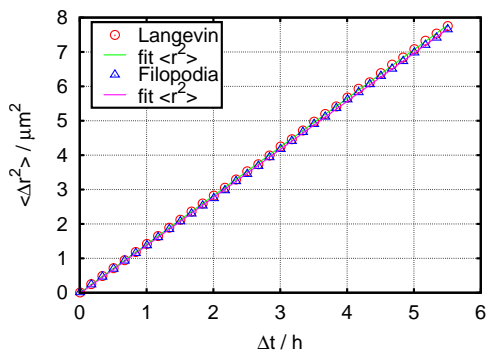


Figure 2.3: Agreement of Langevin and the alternative filopodia approach The agreement of both representations of active cell motion is shown by comparison of the mean square displacements. In the filopodia simulation their number is $N_{\text{filo}} = 6$. Although the forces are generated differently, both models are equivalent.

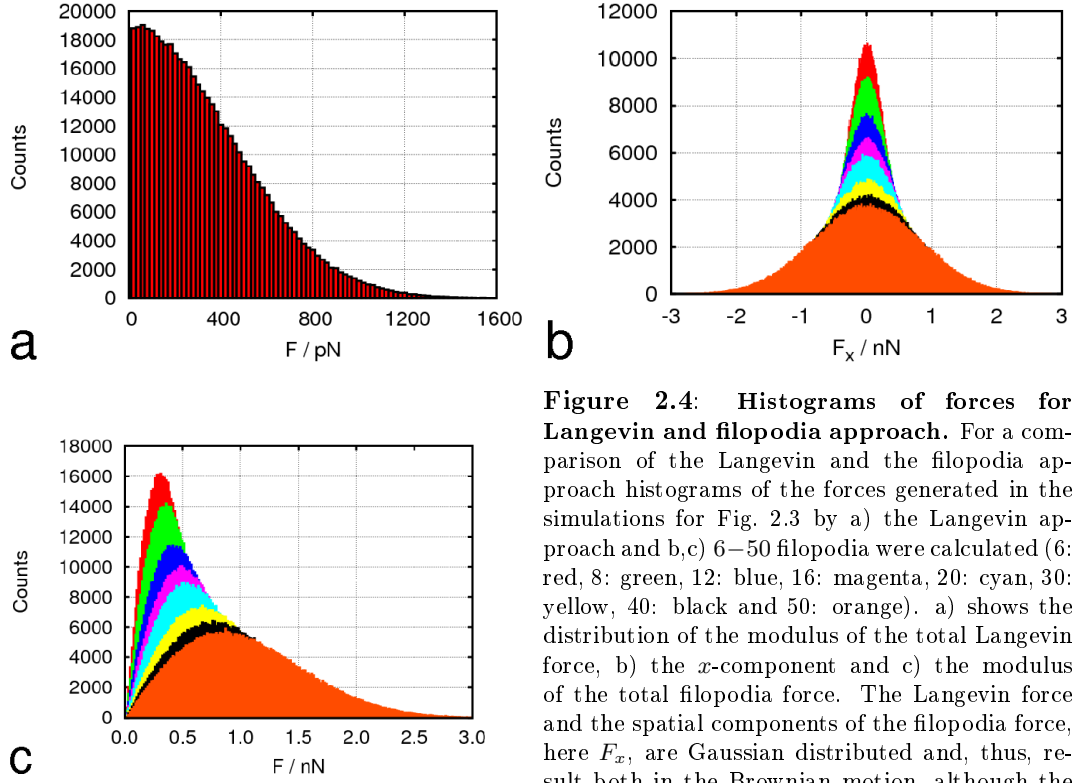


Figure 2.4: Histograms of forces for Langevin and filopodia approach. For a comparison of the Langevin and the filopodia approach histograms of the forces generated in the simulations for Fig. 2.3 by a) the Langevin approach and b,c) 6–50 filopodia were calculated (6: red, 8: green, 12: blue, 16: magenta, 20: cyan, 30: yellow, 40: black and 50: orange). a) shows the distribution of the modulus of the total Langevin force, b) the x -component and c) the modulus of the total filopodia force. The Langevin force and the spatial components of the filopodia force, here F_x , are Gaussian distributed and, thus, result both in the Brownian motion, although the distribution of the total filopodia force is clearly non-Gaussian.

The mean square displacement of a simulation of a single cell using filopodia is compared to the Langevin approach and a good agreement is found (Fig. 2.3). For further comparison the distribution of forces is shown in Fig. 2.4 for (a) modulus of Langevin forces, (b) the x -component of the total filopodia force F_x and (c) its modulus for a varying number of filopodia (6, 8, 12, 16, 20, 30, 40 and 50). In contrast to the modulus with a maximum around the force $F(l_0)$ associated with the mean length l_0 , each component, here F_x , is Gaussian distributed around zero like for the Langevin forces, causing a Brownian trajectory as in the Langevin approach. This means, the Langevin approach can be used equivalently in Eq. (1.14) to a more complex generation of the active force. The final force resulting from the joint action of all filopodia forces can be changed by the parameter for each individual filopodia, but also by N_{filo} as shown in Fig. 2.5. The total force scales with $\sqrt{N_{\text{filo}}}$ like the mean end-to-end vector of an ideal chain known from polymer physics although the step length is Gaussian distributed. The scaling of the width of the distributions of the x -component on the other hand simply follows the Central Limit Theorem [98].

2.1.2 Cell populations

Langevin equation

Modeling cell populations is the next step towards modeling tissue. Therefore simulations of various densities of non-adherent cells were performed in two dimensions on a fixed do-

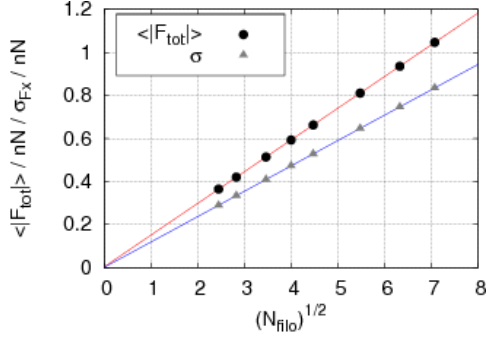


Figure 2.5: Scaling of the mean total filopodia force with filopodia number. Shown are the mean total force $|F_{tot}|$ (dots) and the standard deviation of the x -component of the total force σ (triangles) as a function of $\sqrt{N_{filo}}$ for 6 – 50 filopodia per cell. The two linear fits ($R = 1$) clearly show the scaling of both quantities with $\sqrt{N_{filo}}$.

main with periodic boundary conditions. Using the random forces as given by Eq. (1.14) and calculating the mean square displacement surprisingly reveals two effects as shown in Fig. 2.6a. First, the cells turn out to become more motile with increasing density. Second, although more motile at high densities, they slow down on longer distances. This observation contradicts the intuitive expectation, that cells slow down in higher cell densities like humans tend to move slower than normal in a crowd. To reduce the cells active forces at high friction Eq. (1.18) can be interpreted slightly different as found in [8]:

$$\langle F_i F_j \rangle = \frac{2d\gamma\gamma_0 D}{\Delta t} \delta_{ij} = \frac{2dF_T\gamma}{\Delta t} \delta_{ij}. \quad (2.4)$$

$F_T = \gamma_0 D$ is an energy equivalent subsuming the cellular diffusion coefficient and the cell's pure Stokes friction. Here friction, which increase with cell density, now enters linearly, not quadratic. The resulting mean square displacements are shown in Fig. 2.6. Now the cells slow down at higher cell densities, but the slope of mean square displacement still decreases for long distances.

In both cases the cells move faster on small distances than on longer distances for high cell densities. This effect becomes more pronounced with increasing cell density and, thus, with decreasing mean free path length. To obtain a measure for the mean free path length

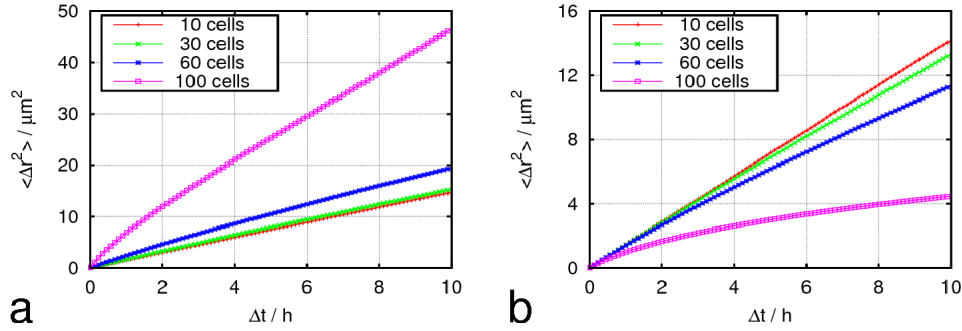


Figure 2.6: Mean square displacements of 2d simulations with Langevin forces for varying cell densities without cellular adhesion. The MSD for the two interpretations of the random forces exhibit different behavior. a) Calculation according Eq. (1.18) $\propto \gamma^2$ results in motility increasing with population density, while b) calculation according according Eq. (2.4) $\propto \gamma$ yield the contrary. In both cases the slope mean square displacements decreases for higher displacements.

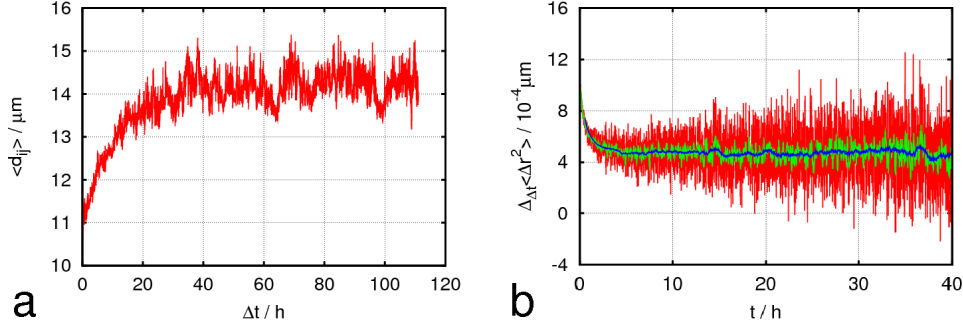


Figure 2.7: Average neighbor distance and onset of linear regime of MSD. a) The evolution of the average neighbor distance (center-to-center) is calculated by a Delaunay triangulation for 80 cells without adhesion on a $100\mu\text{m} \times 100\mu\text{m}$ domain as an estimate for the mean free path length. After equilibration a mean distance of $\sim 14.4\mu\text{m}$ is found. b) The increments of the mean square displacement $\Delta_{\Delta t} \langle \Delta r^2 \rangle = \langle \Delta r^2 \rangle (n\Delta t) - \langle \Delta r^2 \rangle ((n+1)\Delta t)$ indicate the onset of linear behavior. The noisy, original data is smoothed twice in order to allow an estimate of $\Delta t \sim 5\text{h}$ for the the onset of normal diffusion behavior proportional to t .

or average neighbor distance, each conformation was Delaunay triangulated based on the cell centers and the average Delaunay bond length was computed (see Fig. 2.7a). When this mean pathway derived from the Delaunay triangulation is compared with the onset of the linear behavior of the mean square displacement (see Table 2.1) they roughly coincide. This allows the conclusion, that cell-cell interaction limit cellular motility at higher densities. Simulations with various fixed time steps showed an influence on mean square displacement, but increase of motility persisted independent of the simulation time step (not shown).

Filopodia

Random forces: filopodia

In multicellular aggregates filopodia are used as sensory extensions of the cell. Because they are not allowed to penetrate other cells, the vectors representing them are cut off at the point of intersection with the surface of other cells, and the filopodia are regarded to be attached to the surface. In order to model filopodia as information seeking elements, the strength of interaction is assumed to depend only on the cell type. Hence, filopodia attached to the substrate are assigned a force proportional to its length, while filopodia of cell i attached to cell j are assigned a force depending on cell types. The force on cell i is assumed to act in

Nr. of cells	1	10	30	60	80	100
$\overline{d_{ij}} / \mu\text{m}$	—	32.5	22.9	15.0	14.4	12.7
$\sqrt{\langle \Delta r^2 \rangle_{\text{lin}}} / \mu\text{m}$	—	—	—	6.9	5.0	4.4

Table 2.1: Average neighbor distance and onset of linear regime of MSD for varying cell numbers. The average neighbor distance gives an estimate of the mean free path length $l = \overline{d_{ij}} - 2R$ ($R = 10\mu\text{m}$) and is calculated by a Delaunay triangulation. It coincides roughly with the root of the mean square displacement $\sqrt{\langle \Delta r^2 \rangle_{\text{lin}}}$ at the onset of its linear behavior. ‘—’ denotes no clear estimate.

the direction of the center-to-center vector and is therefore given by:

$$\vec{F}_{ij} = C_{ij}\vec{n}_{ij}, \quad (2.5)$$

where C_{ij} is a constant determined by the cell types and \vec{n}_{ji} the center-to-center vector pointing from cell j to cell i . Note, that according to *actio=reactio* an anti-parallel force of the same magnitude is exerted on the other cell. The constant C_{ij} may be viewed as a special case of differential adhesion, such that filopodia connect cells proportional to their surface density of adhesion molecules.

In biological cells an adhesion site is developed over time, if it is attached to the right structure [41, 99]. Therefore, the filopodia attached to other cells are assumed to persist until one of the following occurs:

1. a filopodium contact is replaced by Hertz contact.
2. a filopodium is elongated past a maximum length l_{\max} .
3. the strain of a filopodium $e = \Delta l/l$ in one time step exceeds a threshold e_{\max} .

Note, that if more than one filopodium connects cell i and a cell j their forces sum up.

Because in the model filopodia are not allowed to penetrate other cells, the effect of filopodia is very restricted in dense cell aggregates. In fact, the effect of filopodia is limited to the cells at the periphery of a colony. Their filopodia are not cut off, but generate forces attached to the surface, which are the only active forces entering into the equation of motion. Thus, no significant rearrangement is seen in this case.

An interesting behavior is found for the case of no adhesion. If filopodia do not to adhere to other cells, but prefer only to adhere to the substrate, an equidistant patterning of cells is observed as shown for a cell density of $60\text{cells}/10^4\mu\text{m}^2$ in Fig. 2.8.

For cells with no difference in adhesion this representation of filopodia in dense aggregates cannot generate substantial forces. They are cut at the surface of direct neighbors and do not reach beyond. Cells in the interior stick almost motionless together while forces are only generated by filopodia of cells at the boundary of the colony, which pull these cells away from the colony. Whether the cells leave the colony depends on the adhesive forces.

2.1.3 Discussion

Applying the model presented in Chapter 1 to a single isolated cell generates Brownian behavior, mimicking the experimentally observed behavior [92, 93]. For a single, isolated cell a simple representation of filopodia yields equivalent behavior to the Langevin approach, although the distributions of the moduli of the generated forces differ qualitatively. While the Langevin approach is Gaussian distributed for both, total force and spatial components, summing the forces over all filopodia yields a distribution of the total force similar to an Erlangen distribution. Nevertheless, due to the Central Limit Theorem each component of the total force is Gaussian distributed like the components of the Langevin force. Therefore both approaches give equivalent results for isolated cells in each spatial direction. Mean and width of the distributions depend on the number of filopodia and the constant of proportionality relating filopodia and force.

Contrary to intuition in cell populations motility increases with cell density if Langevin forces are calculated using Eq. (1.18), where the cell's friction coefficient γ enters quadratic in the calculation of the active forces. Friction and repulsive forces are related by the Hertz contact areas. Hence, with increasing friction both, repulsive and active forces grow, which therefore leads on average to bigger displacements. Comparison of the mean free

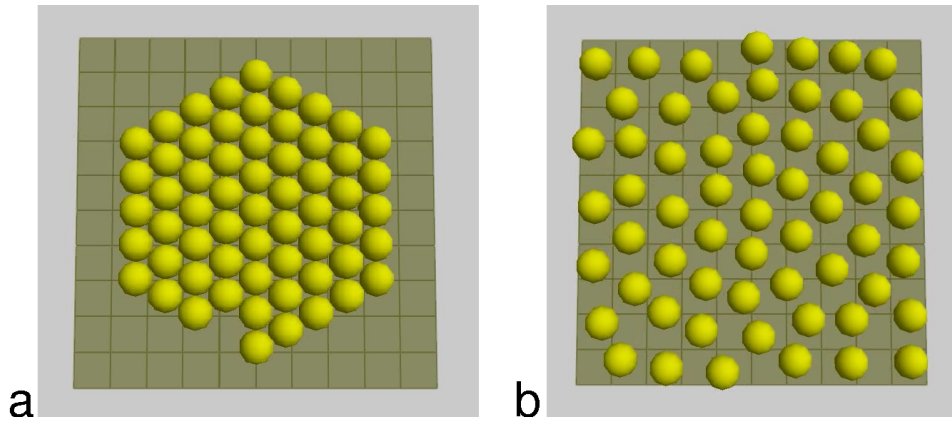


Figure 2.8: Equidistant patterning by filopodia action. Initial and final configuration of a simulation using 10 filopodia, that do not adhere to other cells. Because the filopodia generate forces only attached to the substrate, cells at the rim start to spread, the next layer follows and finally an equidistant distribution establishes.

path length and the distance associated with the onset of the linear regime of the mean square displacement confirms this conjecture. However, Christley *et al.* [100] report that in mesenchymal condensation islands, where cell density is higher, cells move slightly faster than outside, providing an example for such behavior in a system, which is of interest for medical application.

For systems of cells slowing down with density an appropriate model for active non-directed motion is given by Eq. (2.4), where an energy equivalent $F_T = \gamma_0 D$ is defined and friction γ only enters linear. This results in decreasing motility with increasing cell density as seen for most *in vitro* cultures of one cell type.

In cell populations simulated filopodia are cut off at the intersection point with the surface of a neighboring cells. They adhere to either the substrate plane or, if both cells adhere, to a neighboring cell's surface. If the colonies are dense, in the model the filopodia are always cut down and do not generate any force. This could be circumvented by probing the cells' environment more thoroughly and detect gaps using chains or semi-flexible rods. But the computation methods necessary for such an approach would be far more complicated and restrict the application of this model to small cell numbers.

Interestingly, in regeneration phenomena in the liver directed movement and cell division has been suggested to play a major role in an efficient regeneration [101]. Langevin forces support pressure relaxation inside a cell colony in an undirected way, while such a representation of filopodia could explain orientated motion into non-occupied spaces. As a consequence a faster growth dynamics can be expected. By another choice of filopodia parameter even the two scenarios shown in Fig. 2.6 could be explained. The cells should move faster if short filopodia give rise to greater forces and slow down with density if the filopodia exert smaller forces.

However, for the parameter choices in this thesis the filopodia approach is only suited for modeling two completely contrary scenarios: first a equidistant separation of single cells like found for 'proneural' groups of competent epithelial cells in *Drosophila*, which arrange using their filopodia for lateral inhibition [102]. The second scenario is condensation of cells without further motion in the interior.

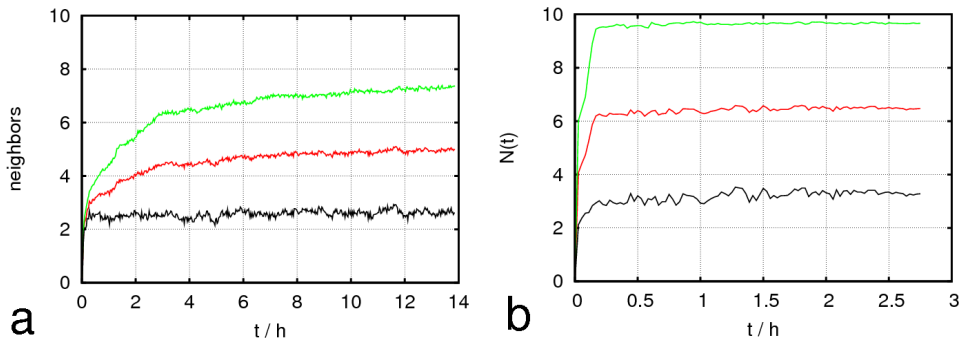


Figure 2.9: Neighbor numbers in a typical sorting process. The number of neighbor of equal cell type are used as a measure for the degree of sorting. Shown is this values for interior cells (green), all cells (red), and exterior cells (black) using a) the Hertz model and b) extended long-range interaction. Initial configuration of the 216 cell is a 3D checker board pattern. a) The cells does not sort completely within 14h for the short ranged Hertz interaction. b) For long-range interaction maximum sorting is reached within minutes.

Since in the following applications cellular aggregates or 2D colonies are considered, this representation of filopodia will not be used for further simulations, but the results for single cell motion support the use of Langevin forces as active cellular forces.

2.2 Cell Sorting

2.2.1 Sorting and differential adhesion

One of the main questions in developmental biology is how complex patterns emerge in multicellular organisms. Orchestrated cell motion is fundamental for achieving such processes. A simple and well studied case of a simple rearrangement process is cell sorting. To emphasize the importance of sorting, exceptional examples are the simple metazoa *Trichoplax adhaerens* and *Hydra*. After dissociation and re-aggregation of the cells both species are able to regenerate a vital organism [103, 104]. An explanation for cell sorting, patterning and other self-assembly processes was early given by the differential adhesion hypothesis (DAH), which states that sorting is driven by different adhesion of the involved cell types [105]. Recently it has been confirmed by transfected L cells expressing adhesion molecules in measured amount [37].

Here the DAH is incorporated into the model as two and three cell types differing in surface densities and type of adhesion molecules. According to the DAH the different adhesion strength between the cell types is expected to result in cell sorting. Simulations in two and three dimensions have been performed using initial configurations of lamellar and checkerboard patterns. As a measure of the sorting process the number of contacts of each type to the same type averaged over the population have been recorded.

Sorting is not accomplished in two and three dimensions and reasonable timescales for Hertz interaction with differential adhesion. Together with Langevin dynamics cells tend to stay in their local minima unless their Langevin forces are increased. Increasing these fluctuations causes the cells to leave the aggregate. Of course, leaving the aggregate could be impeded by further constraints added to the model of adhesion and migration. However,

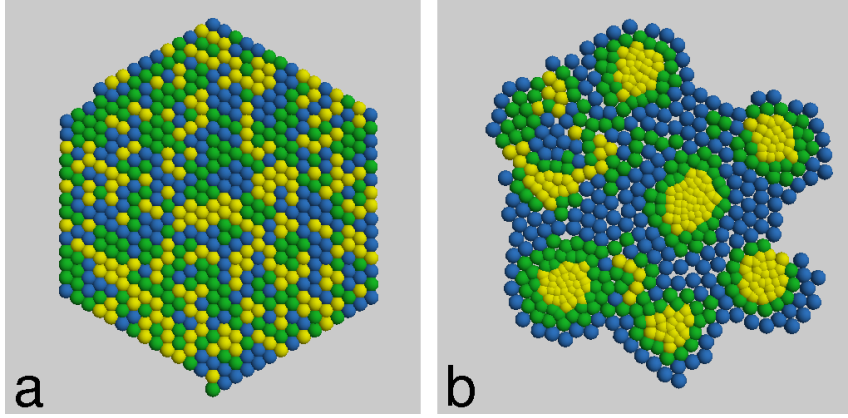


Figure 2.10: Cell sorting of 3x200 cells in 2D. Initial (a) and final configuration after 18d. Despite the small cell number ($200 + 200 + 200$ cells) and long-range attraction ($d_{\text{cutoff}} = 20\mu\text{m}$ and $\sigma_{\text{LR}} = 10\mu\text{m}$), cell sorting is not completed. Adhesion strengths are $c_{11} = 15$, $c_{12} = 10$, $c_{13} = 1$, $c_{22} = 7$, $c_{23} = 2.5$ and $c_{33} = 1.5$.

these findings do not support the DAH for the model used in this thesis, which is based on spherical cells and fluctuations according to a Langevin approach.

2.2.2 Long-range attraction

Cellular protrusions like cilia, lamelli- and filopodia allow cells to explore their environment and/or to exert forces on their environment via adhesion sites. The filopodia introduced in Sec. 1.4 are an example for such extensions. They explore the cell's environment only by random sampling. Increasing the number or frequency of these samples the cell gathers more information until it virtually knows all about its environment within the range of its extensions. This motivates a deterministic extension of the filopodia to a long-range interaction potential up to a cut-off length determined by the maximal length of filopodia. Following Palsson [75] this is done by a smooth extension of the modified Hertz potential Eq. (1.7), resulting in an interaction force given by:

$$F = \begin{cases} \frac{4}{3} \left(\frac{1-\nu_i^2}{E_i} + \frac{1-\nu_j^2}{E_j} \right)^{-1} \sqrt{\frac{R_i R_j}{R_i + R_j}} (R_i + R_j - d_{ij})^{3/2} - \pi \epsilon_{ij} \frac{R_i R_j}{R_i + R_j} & : d_{ij} \leq R_i + R_j \\ -\pi \rho V_{sb} \frac{R_i R_j}{R_i + R_j} \exp\left(\frac{-(R_i + R_j - d_{ij})^2}{2\sigma_{\text{LR}}^2}\right) & : R_i + R_j < d_{ij} < d_{\text{cutoff}} \end{cases} \quad (2.6)$$

where the decay of the long-range potential outside the contact distance is parametrized by the width of the Gaussian σ_{LR} and the range of interaction by the cutoff distance of interaction d_{cutoff} .

Using the Eq. (2.6) the sorting is improved substantially. Typical evolution of neighbor numbers are shown for Hertz and the extended long-range interaction in Fig. 2.9. For small aggregates it completes quickly in two and three dimensions. But for larger cell aggregates, still much smaller than biological systems (≈ 30.000 cells in [106]), sorting does not complete on reasonable timescales. In Fig. 2.10 initial and final configuration of a sorting simulation in two dimensions is shown. After a fast initial reorganization (see Fig. 2.9) further sorting happens increasingly slow. After 18d sorting of the cells has not

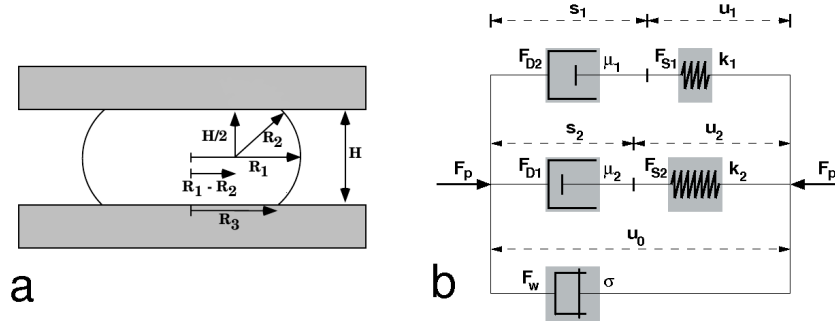


Figure 2.11: Scheme of compressed cell aggregate and generalized Kelvin-body model. a) Shown are the geometrical quantities of a compressed cell aggregate that enter the Laplace equation (2.7) used for calculation of the surface tension. b) The generalized Kelvin-body model for the dynamic response of the cell aggregates is composed of two parallel Maxwell models and a surface tension element.

completed. For the discussion see the discussion of Sec. 2.3, because limitations of the model regarding cell sorting are related to the processes relevant to compression.

2.3 Compression and relaxation

2.3.1 Experiment and theoretical model

Phase ordering in liquids is caused by co- and adherence. The comparison of liquids and cells and the analogy of the processes and phenomena has generated the DAH mentioned above [106]. This analogy to liquids also includes the concept of surface tension [107, 108]. It has been reported that aggregates of embryonic tissue cells relax after a deformation and round up again, which is reminiscent of liquids. The main difference exists in two separated time scales depending on duration of compression. For short compression times a cellular aggregate shows a very elastic response. After long lasting compression, if the rounding up completes, it does only after several hours or days [107]. However, these properties do not represent global features of cells, but are restricted to certain cell types like *Hydra* or embryonic cells. Nevertheless, the similarity to continuum mechanics motivated application of its concepts for studying cellular aggregates of living embryonic cells and their viscoelastic properties. While the relaxation process of the compression force allows estimation of the viscoelastic constants under the assumption of a particular model, an approach to the hypothesized surface tension of certain cell aggregates is given by its geometry. Analysis of the images of compressed and equilibrated aggregates yields its surface tension according to the Laplace equation:

$$\Delta p = \frac{F_{P, \text{equ}}}{\pi R_3^2} = \sigma \left(\frac{1}{R_1} + \frac{1}{R_2} \right), \quad (2.7)$$

where the radii R_1 , R_2 and R_3 are given by the evaluation of the micrographs according Fig. 2.11a. This leads to surface tensions σ for the germ cell lines covering a range of $1 \dots 20 \times 10^{-3} \text{ N/m}$ [107, 109].

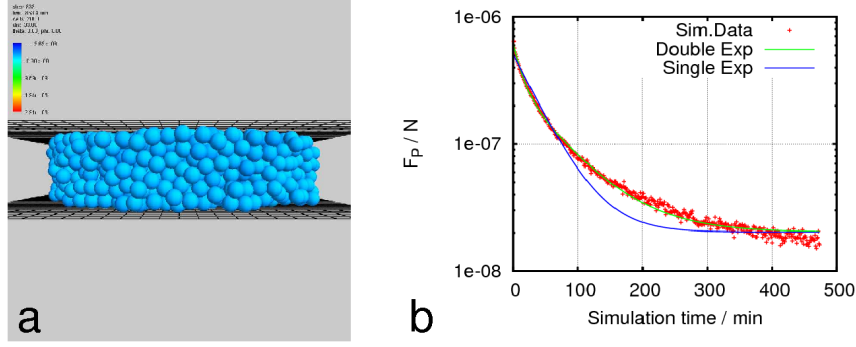


Figure 2.12: Equilibrium shape and fit of compression force. a) Equilibrium shape after compression of the cell aggregate in the reference simulation. b) Force of the same simulation over simulation time and single and double exponential fit of Eq. (2.9). The much better double exponential decay fit gives relaxation times $\tau_1 \approx 13\text{min}$ and $\tau_2 \approx 72\text{min}$.

The generalized Kelvin-body model used for modeling of the viscoelastic behavior is seen in Fig. 2.11b. The dynamics follows the differential equation

$$F_P + \left(\frac{\mu_1}{k_1} + \frac{\mu_2}{k_2} \right) \dot{F}_P + \frac{\mu_1 \mu_2}{k_1 k_2} \ddot{F}_P = \sigma u_0, \quad (2.8)$$

where F_P is the measured compressing force, μ_i and k_i the friction and spring constants, τ_i the relaxation times, σ the surface tension and u_0 a factor depending on the geometry [108]. The solution of this model approach is given by

$$F_P(t) = (\sigma + k_1 e^{-t/\tau_1} + k_2 e^{-t/\tau_2}) u_0. \quad (2.9)$$

To obtain the relaxation times a fit of the measured force according Eq. (2.9) is done.

2.3.2 Simulations

In all simulations a pellet of 2000 cells is used. The pellet is compressed symmetrically by two plates until the plates reach a defined stop positions at a distance H . During the simulation the forces on the plates, the R_1 , R_3 and the force F_P are recorded. The force F_P is measured as the sum of cell-plane interaction forces calculated according Eq. (1.7). R_1 is measured as maximum extensions in the xy -plane of all cells, R_3 for the cells in plane contact. R_2 is calculated from the cell positions by geometrical considerations. The surface tension σ is finally computed using Eq. (2.7).

Reference simulation A first simulation was performed using the parameter set given in table Table 2.2. After compression the aggregate is almost cylindrical (see Fig. 2.12), which makes calculation of R_2 and therefore σ less reliable. The relaxation of the force $F_P(t)$ shows the same qualitative behavior as in the experiments. The double exponential Eq. (2.9) fits the data very well with a correlation coefficient of $R = 0.9954$ as shown in Fig. 2.12. The resulting relaxation times turned out to be $\tau_1 \approx 13\text{min}$ and $\tau_2 \approx 72\text{min}$, and therefore very large in comparison to the experimentally determined values for embryonic cells, which are in the range of seconds: $\tau_1 = 1.9 \dots 2.7\text{s}$ and $\tau_2 = 20 \dots 45\text{s}$ [108]. The fitting result

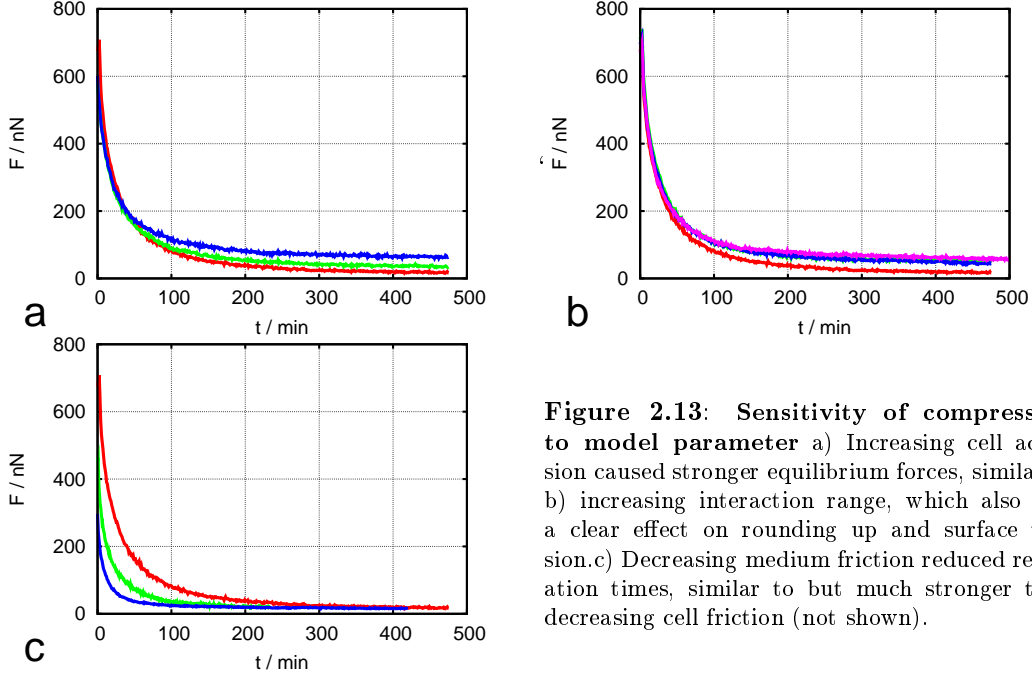


Figure 2.13: Sensitivity of compression to model parameter a) Increasing cell adhesion caused stronger equilibrium forces, similar to b) increasing interaction range, which also had a clear effect on rounding up and surface tension. c) Decreasing medium friction reduced relaxation times, similar to but much stronger than decreasing cell friction (not shown).

showed a strong interdependence of the fitting parameters and a dominant contribution of one exponential suggesting that one time scale might be dispensable. Interestingly, a fit of a single exponential decay resulted in a good correlation coefficient $R = 0.975$ and a relaxation time $\tau = 36$ min between the former two, but showed a qualitatively different behavior as seen in Fig. 2.12. Thus, the second time scale is definitely necessary for describing the measured phenomena.

Sensitivity analysis To explore the parameter space systematically for a faster relaxation process, a sensitivity analysis was performed. Different parameters were found to influence the main quantities of interest: the force on the compressing plates F_P , the surface tension σ and the relaxation times $\tau_{1/2}$. Increasing cell-cell adhesion ϵ resulted in higher forces F_P (Fig. 2.13). Extending the range of cellular interaction improved rounding of the aggregates and resulted in higher surface tension. Decreasing medium viscosity reduced relaxation times, similar to reduction of cell-cell friction. Plane velocity turned out to be a critical parameter, because interaction restricted to next neighbors in conjunction with a slow growing

Table 2.2: Parameter of the reference simulation.

N_{cells}	E_{sb}	η_{medium}	σ_{lr}	r_{lr}	D	E_{cell}	ν_{cell}	γ_{cell}	ϵ_{cell}
	J	Pa s = N s/m ²	m	m	m ² /s	Pa		Ns/m ³	N/m
2000	10^{-19}	10^3	–	–	4×10^{-16}	10^3	0.4	3×10^7	6×10^{-5}
	h	v_{plane}	E_{plane}	ν_{plane}	γ_{plane}	$Q_{\text{adh,plane}}$			
	μm	m/s	Pa		Ns/m ³	m ⁻²			
	5	5×10^{-9}	10^7	0.33	1×10^8	0			

repulsion force $F \propto d_{ij}^{3/2}$ and high friction leads to slow relaxation and therefore to huge deformations and, finally, cell-cell penetrations.

Importantly, the equilibrium force and shape depend on plane velocity. After realizing such differences to the behavior of liquids, it is not surprising that other analogies to liquids failed. In this line the surface tensions turns out not to be an intrinsic property in the model and to change with the final distance between the compressing plates H . In no simulation of the sensitivity analysis the calculated relaxation times got smaller than ~ 1 min. The aggregate expanded always in the layer in contact to the moving compression plate. The rounding up after compression was not reproduced, neither directly after compression nor after force relaxation.

2.4 Discussion: Limitations of Spherical Models and Possible Applications

In Chapter 1 a cell model has been introduced based on very fundamental properties of cells. Motivated by the observation of the spherical shape, which cells adopt in suspension, they are modeled as adhesive and elastic spherical agents that follow a Langevin equation of motion. Adhesion and interaction are included by a modified Hertz model. The cell cycle is modeled as a process divided in two phases of growth and division.

In Sec. 2.1 simulations have been analyzed regarding the characteristics of simulated cell motion of single cells and in cell populations. For cell motion two approaches were used, Langevin forces or filopodia, and both resulted in Brownian behavior. The equivalence of both approaches motivates the use of Langevin in the rest of the thesis.

In cell populations two scenarios have been derived for the Langevin approach depending on the interpretation of the stochastic force: average cell motility increases or decreases with cell density. Both of them may be used in adequate context, for example mesenchymal condensation, where cells migrate faster in the condensation centers, or confluent cultures, where cells slow down. Since most cells are expected to slow down in denser colonies, in the following Eq. (2.4) will be used. Differences in the interpretation of the stochastic force can be motivated by the observation, that the Langevin-approach for cells bases on a heuristic analogy to Brownian particles. However, different from Brownian particles the stochastic term is - for active cell migration - not a consequence of collisions with other small particles (fluid particles in the case of Brownian particles) so the fluctuation-dissipation theorem that links the autocorrelation amplitude of the fluctuations with the dissipation cannot be expected to hold for cells. Indeed, the analogy drawn by Beysens *et al.* [106] is purely formal but does not base on fundamental principles. While in fluids the proportionality constant between fluctuation and the inverse of dissipation is the temperature that can be measured, the temperature-equivalent in cells is a quantity that can be controlled by the cell itself and hence is a parameter, that depends on the cell type and its regulatory state. This justifies different choices for the amplitude of the Langevin force, that mimics the active random cell movement (the cell micro-motility).

Considering cell sorting and compression of cellular aggregates, it is clear that within the model the driving forces are energy minimization and fluctuations. Using the model presented in Chapter 1 for cell sorting revealed the complementarity of exploring the configuration space by fluctuations and instability of the aggregate. For small fluctuations, sorting was slow and did not complete for small aggregates, because the spherical cells stay in local minima. Increasing the fluctuations, i.e. random forces without directional bias or additional restrictions, to enable cells to leave such local minima results in cells detaching

from the cellular aggregate. This happens, because leaving a local minimum is always based on escape from the Hertz potential of the neighboring cells. For sorting this has to occur inside a dense aggregate and elastic interaction with the neighbors in the direction of motion requires an active force much stronger than necessary for breaking a cell-cell contact on the surface. On the surface this force disconnects the cell from the colony. This effect could be controlled by adding the constraint, that forces are always orientated toward other cells which is not considered in this thesis.

Allowing the cell to expand its information horizon by introducing an interaction potential similar to Palsson [75] immediately speeds up the sorting for small cell numbers. But the sorting does not complete at higher cell number which are still below cell numbers of ≈ 30.000 in real pellets, which are typically $200\mu\text{m}$ in diameter. In the model by Palsson cells are represented as deformable ellipsoids with an interaction radius up to beyond two cell diameters for sorting and a random force [75]. This long radius enables sorting of aggregates up to 1350 cells, which still depends on the random force. It therefore must be assumed, that cell sorting using the model of Palsson fails at higher cell numbers, too. A rigorous analysis of the correlation of interaction range and aggregate size would quantify the expected limitations.

The ‘Cellular Potts model’ by Graner and Glazier [110] could successfully mimic the cellular rearrangement during sorting in aggregates up to 2×10^4 cells [111]. Each cell is represented as an individual state, and the modifications include a target volume and surface energy for each cell. Cells move in this model in an ameboid fashion through the aggregate and complete sorting in finite time. However, this model has a number of other short-comings: the time scales can only hardly be matched with true time-scales; one reason for this is that it uses the Metropolis algorithm which needs the definition of an effective temperature. This temperature parameter has to be chosen small enough so that single cells do not decompose into individual fragments, and large enough so that no frozen aggregates emerge. Interestingly, Jiang *et al.* [112] also state a possible cooperation of the differential adhesion hypothesis and chemotaxis in the formation of fruiting bodies of *Dictyostelium*. This confirms the conjecture that the DAH alone may not explain biological reorganization processes like sorting of large cell numbers, but that these processes require information exchange over longer distances than covered by the interaction potential. The importance of adhesion molecules shown by Foty *et al.* [37] for sorting may originate from the tri-functionality of cadherins [89], but seems likely not to be the only key mechanism for cell sorting. First attempts have shown, that chemical signaling and directed motion which is driven by larger forces to squeeze the cells along its way into favorable conformations enable the model of this thesis to complete sorting, but it has not been studied thoroughly.

Simulations of the compression of spherical aggregates reproduced qualitatively the relaxation of the compression force observed in the experiments. A double exponential decay gave a good fit and indicated two separate time scales for relaxation. However, neither the relaxation times nor the equilibrium shape in the biological experiments could be reproduced. Because the equilibrium configurations showed in general clear differences to the biological ones, derivation of the surface tension according to Eq. (2.7) did not yield the same surface tensions as found by Forgacs *et al.* [108]. This model considers the cells as a homogeneous material described by the generalized Kelvin model discussed above. It is not guaranteed that the relaxation behavior is not simply captured by a fit to its solution involving many parameter as are the results of the simulations ($R = 0.9954$).

For relaxation of the aggregate after compression two phases were clearly distinguished: viscoelastic response of single cells and rearrangement of cells. Compressed for only a short time the cells flatten inside the pellet, as was shown by micrographs, and show an sort

of elastic response after release within minutes [108]. An approach to model both, the equilibrium shape and the elastic response, could be modeled by introducing fixed cell-cell junctions and conservation of the cell volume into the model, which was out of the scope of this thesis.

After a longer time of compression, the cells start to rearrange and to adopt a regular shape again and the rounding after release takes hours to days like rounding after centrifugation (e.g. [113]). To describe this second relaxation regime the fixed junction would be release at a certain rate, to allow the cells to rearrange. However, for the rounding accounts the same discussion as for sorting. Thus, the model presented in Chapter 1 is limited in the sense that the model does not account neither for the conservation of the cell volume nor for the reorganization processes of the cytoskeleton and the adhesion complexes.

The approximation of adhesion energy and friction proportional to the contact area is useful only for slow detachment and rearrangement. The same accounts for the elastic approximation of the cytoskeleton by the Hertz potential which does not capture greater viscoelastic deformations, but yields good results for moderate ones. A non-spherical model for deformation, a viscoelastic interaction potential and slowly relaxing bonds could improve the agreement of the modeling results and the findings by Forgacs *et al.* [108]. The rounding up after compression would need the same directed motion as mentioned above that could be introduced by chemical signaling.

However, it has been shown, that growth processes in two and three dimensions, which do not involve reorganization could be well explained by this type of model (e.g. [8, 9, 88]). An advantage of the spatial individual cell-based model is, as mentioned in the introduction, the easy integration of individual spatial information. Examples are the availability of nutrients [9] and information on cell-contacts [38, 114]. Finally, the general advantage of individual cell-based models is their ability to comprise any individual cellular information, e.g. stemness or differentiation [115]. These restrictions and advantages are the basis for choosing the applications presented in the following chapters.

3

Modeling Oxygen-Dependent Expansion and Differentiation of Mesenchymal Stem Cells

3.1 Introduction

After the discussion of the limitations of the individual-based model at the end of the previous chapter, here it will be applied to oxygen-dependent phenomena of colony growth and subsequent differentiation of mesenchymal stem cells (MSC). In contrast to the last chapter, where the cells were modeled as physical agents in space using constant parameters without individuality (except deviations in adhesion for sorting), here each agent will be equipped with a cell parameter summarizing the cellular differentiation state, which depends on the environment.

The experimental results presented here have been produced by Matthias Zscharnack, Center for Biotechnology and Biomedicine, University of Leipzig. Materials and methods of the experimental procedures are given in the Appendix. Experimental results and theoretical modeling are closely related and will be presented in parallel. The computer simulations closely follow the experimental protocols, such that the simulations may be viewed as ‘experiments in silico’ (on the computer) and their results can directly be compared to those found in the experiments. The predictions derived from the simulations predict optimal conditions for chondrogenic differentiation currently used for optimization of a bioreactor. Thus, the results represent one iteration of hypothesis-driven research as motivated in the introduction.

Noise in cell regulation. Many molecules involved in regulatory processes exist at very low intracellular concentrations, which results in large spatial variations and random molecular processes [116,117]. Because the cells need to control the effect of this noise on intracellular processes like transcription, they employ stabilizing principles like genetic redundancy

and feedback [117]. On the other hand noise also offers the advantage of variability even in monoclonal populations and allows for rapid adaptation [118]. Although there is a high variability on cell level, on the level of the whole population a stable average is created based on a stable population profile or structure [119]. For hematopoietic progenitor cells the stability of this population structure regarding the expression of the stem cell marker Sca-1 has been shown experimentally. After separating subpopulations defined by a low, medium or high expression level of Sca-1, the expression profiles in the subpopulations regenerated the original profile of the original population within a couple of days [120]. In the complex organization of metazoan development and homeostasis such processes control and activate differentiation [121]. Embryonic stem cells, for example, have been shown to control the noise at genes promoting differentiation to keep their pluripotency [122].

Mesenchymal stem cells (MSCs) are multi-potent progenitor cells capable of differentiating into bone-marrow stromal cells, osteoblasts, chondrocytes, myocytes, and adipocytes. In some tissue types, such as bone-marrow stroma, fat, skeletal muscle, and synovium, MSCs persist in adult life without losing their capacity to proliferate and differentiate [123]. Under appropriate conditions they can multiply and transform into specialized cell types. These processes were found to be at least partially reversible, demonstrating a limited but significant plasticity of MSCs [124]. During the last years, the application of MSCs in tissue engineering became a major subject of regenerative medicine; in particular concerning cartilage and bone regeneration [125]. Maintenance of MSCs as well as their differentiation relies on specific environmental cues like growth factor supply and matrix elasticity [48,126]. Interestingly, there is growing evidence that stem cells are adapted to limiting metabolic conditions [127]. In agreement with this observation, low oxygen supply has been suggested to preserve early progenitor states *in vitro* [128]. Accordingly, MSC-derived cell populations show higher proliferation activity when cultivated under low oxygen tension (2-5% pO₂) compared to high oxygen tension (20-21% pO₂) (human MSCs [128], mouse MSCs [129], rat MSCs [130]). Additionally, cell populations expanded at low oxygen tension show a faster and more directed differentiation into osteoblasts, adipocytes (human MSCs [131], rat MSCs [130]) as well as chondrocytes (human MSCs [132,133]). However, studies on the direct impact of the oxygen tension on differentiation in 2D and 3D cultivations resulted in controversial findings. Malladi *et al.* [134] found for adipose-derived mouse MSCs that osteogenesis in monolayers and chondrogenesis in pellet culture is significantly impaired at 2% pO₂ compared to 21% pO₂. According to results by D'Ippolito *et al.* [128] this applies also for osteogenesis of human bone marrow-derived MSCs at 3% pO₂. In contrast, Lennon *et al.* [130] found no significant differences in osteogenesis between rat bone-marrow derived MSCs cultivated at 5% and 20% pO₂, respectively. Moreover, human adipose-derived MSCs in alginate bead culture showed an increased production of chondrogenic matrix molecules at 5% pO₂ compared to 20% pO₂ [135].

State of the art. A large number of theoretical approaches to tissue engineering aim at quantitatively describing culture conditions as the oxygen distribution, and their impact on processes like matrix formation ([136] and references therein). While many innovative tissue engineering strategies rely on stem cell expansion and differentiation, theoretical models of these systems are rather rare [137,138]. In order to provide reliable predictions about the dynamics of such systems theoretical approaches are required that account for both: i) the composition and structure of the individual cell environment and ii) particular stem cell properties like lineage plasticity and it seems, that currently such models are not available.

Modeling approach. Motivated by the recent findings on the importance of noise in cellular processes as genetic regulation and differentiation a noise-based model for the population dynamics of promyelocytic progenitor cells was presented [139]. Here this model of noise-driven differentiation is integrated into the spatial model, where it accounts also for the local environment of individual cells. Following the stem cell concepts of Loeffler and Roeder [140,141] it is a pedigree-free approach. Within the model two properties, the proliferation rate and the amplitudes of cellular state fluctuations, determine the organization of a stationary population structure with respect to cell differentiation. While the proliferation is assumed to be differentiation state-specific, the cellular state fluctuations are assumed to be sensitive to the oxygen environment. The model further assumes that cell adaptation to un-physiological high oxygen tension results in decreased cellular state fluctuations in differentiated states and thus, accumulation of cells in these states. In contrast, low oxygen tension conserves stem cell and progenitor states. The experimentally observed impact of low oxygen expansion on subsequent differentiation in pellet culture is simulated as a result of less pre-differentiation and higher lineage plasticity of progenitor and stem cells in MSC-derived cell populations.

3.2 Modeling MSC Differentiation, Lineage Specification and Growth

3.2.1 Differentiation

Cell differentiation is defined as the loss of stem cell properties. It can be accompanied by but is not identical to lineage commitment (see below). Cell differentiation is quantified by a continuous state variable α that can adopt values between zero (full stem cell competency) and one (completely differentiated cell). Each value of α may represent a set of regulatory network activation patterns. From the molecular point of view, α may depend on the abundance and sub-cellular localization of proteins and RNAs, as well as other types of signaling and metabolic molecules [142].

Each cell's α -value is assumed to fluctuate randomly with a state-dependent noise amplitude $\sigma(\alpha)$. From its current differentiation state α it adopts a new state α' with a randomization rate R . The probability of a transition $\alpha \rightarrow \alpha'$ is given by a Gaussian of width $\sigma(\alpha)$, which is restricted to $[0, 1]$ and normalized:

$$p(\alpha'|\alpha) \propto \exp\left(-\frac{(\alpha' - \alpha)^2}{2\sigma^2(\alpha)}\right), \quad (3.1)$$

where the width of the Gaussian $\sigma(\alpha)$ represents the amplitude of the fluctuations and is state-dependent (Fig. 3.1a). Cell differentiation is assumed to be reversible incorporating recent stem cell concepts [141] and to occur independently of cell proliferation as found in progenitor systems [143]. But the state dependence of fluctuation strength causes a drift such that cells tend to accumulate in low noise states. Hence, a differentiation inducing environment reduces noise in high- α states causing an accumulation of differentiated cells. The explicit dependence of the noise amplitude on the environment is given in Sec. 3.3.

3.2.2 Lineage commitment

MSCs are capable of differentiation into several lineages. At each differentiation state different lineages can be distinguished by their characteristic regulatory network activation

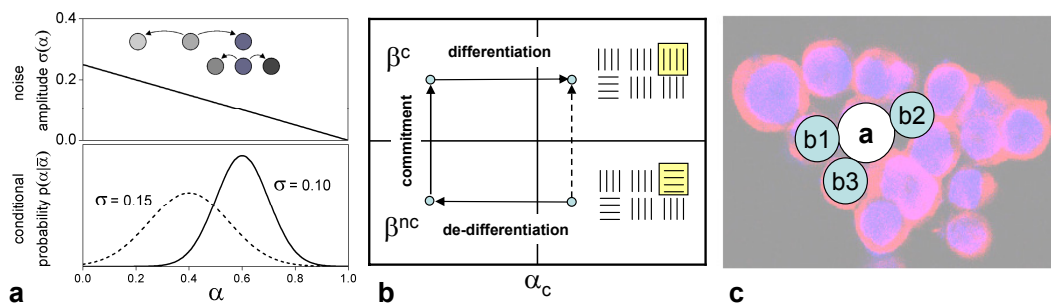


Figure 3.1: Differentiation Dynamics and Lineage Commitment a) Modeling fluctuations of the differentiation state α . Upper panel: A decrease of the noise amplitude $\sigma(\alpha)$ of the Gaussian conditional probability function $p(\alpha'|\alpha)$ with α results in an accumulation of cells at higher values of α . Lower panel: Gaussian distributions $p(\alpha'|\alpha)$ for $\alpha = 0.4$ and $\alpha = 0.6$. Their width $\sigma(\alpha)$ parameterizes the strength of α fluctuations. b) Modeling lineage specification. Different states of lineage activity β^c and β^{nc} may be characterized by different activation patterns of the regulatory network (small boxes). A transition between the states is assumed to be impossible for $\alpha > \alpha_c$ (dotted line) but may occur subsequent to de-differentiation. b) Cell-cell interaction. The induction of a chondrogenic phenotype of cell (a) requires a sufficient differentiation of the cell itself and that a defined number of neighbor cells are within the same lineage, here (b1), (b2), and (b3).

patterns. Thus, the characterization of a cellular state requires introduction of a second state variable β , which specifies the lineage. Whether a cell expresses markers of a specific lineage, e.g. the SOX-9 transcription factor for the chondrogenic lineage [144], depends on the value of β . According to the experimental observation that an entire spectrum of regulatory states may contribute to a defined lineage [120], a continuous state variable was chosen. The β -value is assumed to fluctuate as long as a cell is not fully committed. Lineage commitment is modeled as a cellular response to changing environmental conditions leading to a restriction of the accessible values of β . This can be understood as a consequence of large-scale transcriptional silencing of the genome of these cells [145]. Here a chondrogenic differentiation assay as applied in our study is modeled as a restriction of β in a way that only a spectrum of states S_{chondro} remains accessible, which is specific to the chondrogenic lineage. The dynamics of the chondrogenic lineage commitment is characterized by the transition rates $W(\beta^{nc} \rightarrow \beta^c, \alpha)$ from non-chondrogenic states β^{nc} into chondrogenic states $\beta^c \in S_{\text{chondro}}$. These transitions are assumed to be irreversible under the conditions of the assay. Sufficiently differentiated cells are no longer plastic and cannot switch lineage. Thus, the transition rates $W(\beta^{nc} \rightarrow \beta^c, \alpha)$ are larger than zero for un-differentiated cells only. For simplicity they were set to be equal W_0 for $\alpha < \alpha_c$ and zero otherwise (Fig. 3.1b).

3.2.3 Induction of a functional phenotype

In the model differentiation and lineage commitment are necessary but not sufficient to induce a lineage-specific functional phenotype within a cell. Experimental observations suggest that cell-cell interactions via N-cadherins are essential for the induction of a functional chondrogenic phenotype in MSC-spheroids [34]. Hence, within the model the induction of the chondrogenic phenotype is assumed to require: first, a chondrogenic specification of the cell ($\beta \in \{S_{\text{chondro}}\}$), second, a sufficient differentiation ($\alpha > \alpha_d$), and third, a minimum

number N_c of neighbor cells in the same lineage (Fig. 3.1c). This phenotype induction is reversible due to the general reversibility of differentiation in the model.

3.2.4 Cell proliferation

Here cell proliferation is assumed to depend on the differentiation state α of a cell. Proliferation is restricted to progenitor cells of intermediate differentiation states α with $0 < \alpha_s < \alpha_p < \alpha_d < 1$. For these states an identical average growth time τ is assumed. Stem cells ($\alpha < \alpha_s$) and differentiated cells ($\alpha > \alpha_d$) do not proliferate. During the growth process cells may frequently switch between proliferative and non-proliferative states. This will result in an effective cell growth time larger than τ .

Further, proliferation is limited by contact inhibition (see Sec. 1.5). It was demonstrated that the growth behavior of simulated cell population on long timescales is neither affected by the details of the assumptions on the precise shape of the interaction forces between cells nor by the details of the cell cycle model [88]. So, the obtained results should be robust against changes of these model details.

3.2.5 Oxygen distribution

The reaction-diffusion equation Eq. (1.24) is used to calculate the oxygen concentration $c(r, t)$ within the pellet. It is assumed to be constant and equal in all lattice sites outside the pellet. The parameters are chosen according to Malda *et al.* [146] and Zhao *et al.* [147] (see Table A.1). In order to keep the simulations feasible pellets of 20.000 cells were used in the simulations of the chondrogenic assays.

3.3 Results

3.3.1 Low oxygen tension increases proliferation and colony forming potential of MSCs.

Experiments: The growth dynamics of ovine MSCs was analyzed applying different expansion assays. Fig. 3.2a shows a typical result of a CFU-F assay performed with mononuclear cells from bone-marrow isolates. After 14 days cells expanded at low oxygen tension showed a twofold higher CFU-F potential compared to those expanded at high oxygen tension. Moreover, they formed larger and more extended colonies indicating a shorter doubling time of these cells on average. This observation was confirmed selecting individual cells from analogue cultures and analyzing the size distribution of small colonies growing from them. Cells at low oxygen tension formed significantly larger colonies compared to cells at atmospheric conditions. The colony size distributions after 5 days are summarized in Fig. 3.2b and c for 5% pO₂ and 20% pO₂, respectively.

Simulations: Motivated by the observed CFU-F dependency on the oxygen tension an oxygen level specific control of the differentiation state fluctuations was concluded. Hence, the noise-amplitude σ is modeled as a function of differentiation state α and the oxygen tension pO₂:

$$\sigma(\alpha, \text{pO}_2) = \sigma_0(1 - \alpha f(\text{pO}_2/\text{pO}_2^{\text{max}})) \quad \text{and} \quad f(x) = \frac{x^n}{x^n + k^n}, \quad (3.2)$$

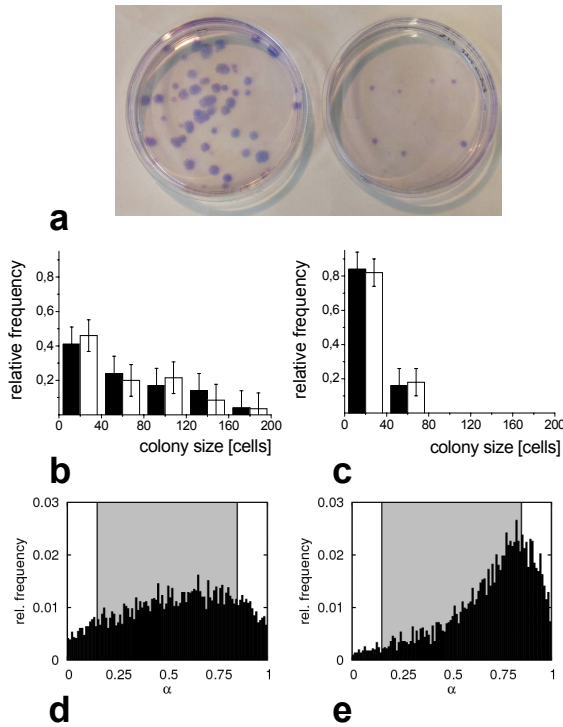


Figure 3.2: Growth dynamics of MSC populations at different oxygen tensions. a) CFU-F assay for mononuclear cells from bone marrow isolates at 5% pO₂ (left) and 20% pO₂ (right). Growth time: 14 days. b,c) Monoclonal expansion assay: size distribution of colonies grown from single cells at 5% and 20% pO₂, respectively. Experimental results (black columns) are compared with simulated results (white columns). Growth time: 5 days. For model parameters see Table A.1. d,e) Simulated equilibrium distribution of the differentiation states at 5% and 20% pO₂, respectively. The shaded regions indicate proliferative states ($0.15 < \alpha < 0.85$).

with σ_0 denoting the stem cell state fluctuation strength and $f(x)$ being a Hill function approaching 0 and 1 at low and high pO₂, respectively. pO₂^{max} refers to atmospheric oxygen tension. Simulated MSC colony growth thus depends on the randomization rate R , the stem cell state fluctuation strength σ_0 , and the parameters of the Hill function (n and k) and those specifying the proliferation rate (r and α_d with $\alpha_s = 1 - \alpha_d$). Extensive simulations were performed to explore the sensitivity of the simulation results with respect to the model parameters. The average size of the MSC clones was found to depend sensitively on the proliferation rate r and the proliferative range (α_d, α_s).

The influence of all other parameters depends on the oxygen tension pO₂. In the general case where the growth rate varies throughout the population an accumulation of fast proliferating cells occurs in the population. This effect is more pronounced in a low oxygen environment where cells enter proliferative states more frequently. This applies already for the initial expansion of the mononuclear cells isolated from the bone marrow. Thus, in order to obtain a quantitative agreement with experimental data it was necessary to assume that cells prepared at 5% pO₂ have a slightly higher proliferation rate on average compared to those prepared at 20% pO₂. An appropriate fit of the experimental data was achieved applying the parameter sets given in Table A.1 (see Fig. 3.2b,c). The simulation results refer to highly motile cells like MSCs. Less motile cells would form more dense colonies and contact inhibition of growth would strongly reduce their proliferation activity. Due to the observation that the colonies were rather sparse after 5 days of growth the simulation parameter were chosen to avoid contact inhibition of growth at both 5% and 20% pO₂.

The simulated MSC population structures at equilibrium are given in Fig. 3.2d,e. Note the different shape of the relative frequency distribution at 5% and 20% pO₂, respectively. While at 5% pO₂ a significant fraction of about 9% of non-proliferative stem cells (defined by: $\alpha < \alpha_s = 0.15$) is conserved, at 20% pO₂ this fraction amounts to 3% only. On the other

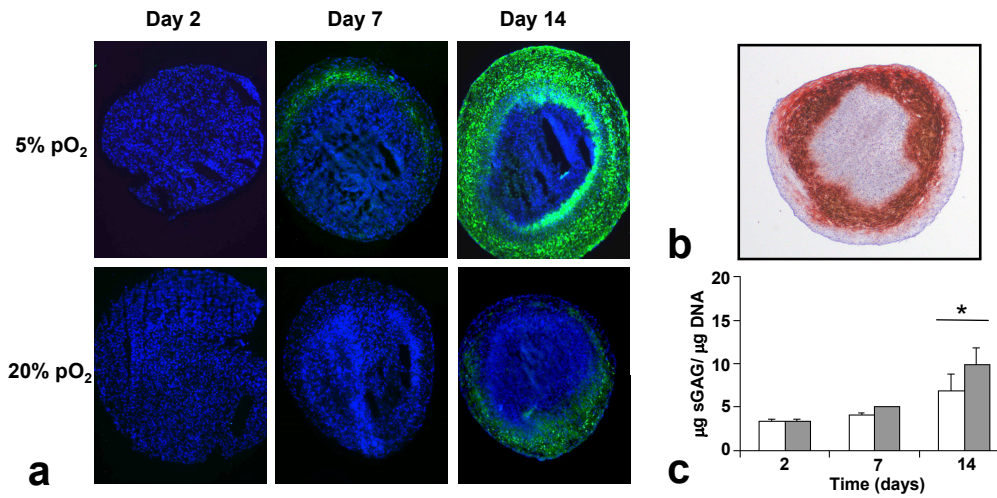


Figure 3.3: Experimental results on chondrogenic differentiation of MSCs at 20% pO₂. a) Collagen II expression in pellet of cells expanded at 5% (upper row) and 20% (lower row) pO₂. Collagen II (green), DAPI (blue). Interestingly, the differentiation starts in a defined layer beneath the surface. b) This behavior is confirmed by a second collagen II staining. c) Glycosaminoglycan concentration of chondrogenic differentiated pellets. sGAG levels were normalized to DNA content. After 14 days sGAG levels of cultures expanded at 5% pO₂ cells were significantly higher compared to cultures expanded at 20% pO₂. * $p < 0.05$; (Student's paired t-test); $n = 4$.

hand the model predicts a fraction of about 14% unspecific differentiated, non-proliferative cells (defined by $\alpha > \alpha_d = 0.85$) at 5% pO₂ compared to 26% at 20% pO₂. Identifying these cells as potentially pre-mature senescent cells the obtained fractions are larger than those identified experimentally by senescence-associated β -galactosidase staining in monolayer cultures [148]. However, the ratio found between low and high oxygen tension culture is comparable. In contrast to the simulated colony sizes the results for the population structures showed to be robust against moderate changes of the proliferation rate (see Fig. 3.9).

3.3.2 Expansion at low oxygen tension increases the chondrogenic differentiation potential of MSCs

Experiments: Chondrogenic differentiation of ovine MSCs was demonstrated by gene expression analysis (aggrecan, collagen type II, X) and immunohistochemistry (SOX-9, aggrecan, collagen type II). As an example, Fig. 3.3a,b show results on the collagen type II expression during chondrogenic differentiation at 20% pO₂. The expression of this essential marker of chondrogenic differentiation is strongly increased in pellets of cells expanded at 5% pO₂ compared to pellets of cells which were expanded at 20% pO₂. Sulfated glycosaminoglycans (sGAGs) represent a further prominent marker of chondrogenesis. In order to quantify the accumulation of chondrogenic extra-cellular matrix in pellet cultures, sGAG concentrations were determined by a DMMB assay and normalized them to the DNA content. After 14 days the pellets of cells expanded at 5% pO₂ had a 1.4-fold higher sGAG concentration ($9.8 \pm 2.0 \mu\text{g}/\mu\text{g}$; $p < 0.05$) when compared to pellets of cells expanded at 20% pO₂ ($6.9 \pm 1.9 \mu\text{g}/\mu\text{g DNA}$, Fig. 3.3c).

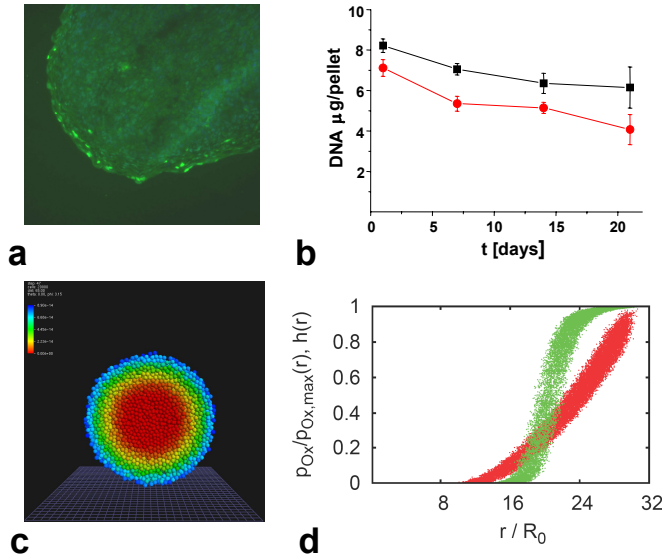


Figure 3.4: Properties of the chondrogenic pellet culture.

a) KI67 staining in a spheroid after 7 days. Proliferation occurs in some cells of the periphery only. b) DNA-content of pellets of cells expanded at 5% (black) and 20% (red) pO₂. During the first 7 days the number of cells decreases. At later times it remains approximately constant. c) Simulated equilibrium oxygen distribution within a MSC spheroid using a oxygen consumption rate of 65 fmol/h per cell. High oxygen tension: blue, low oxygen tension red. d) Oxygen concentration within the spheroid shown in c) vs. radial distance from the spheroid center r for all cells (red). Additionally the Hill function $f(pO_2(r))$ is shown (green, hill coefficient $n = 5$, dissociation constant $k = 0.3$, Eq. (3.2)). Note that both curves are smeared out due to the finite lattice constant.

Simulations: It was hypothesized that the observed differences in the synthesis of chondrogenic proteins are due to the different structure of the MSC populations after expansion at 5% and 20% pO₂ (Fig. 3.2d,e). In order to support this hypothesis the differentiation process within MSC spheroids was simulated using the resulting population structures of the expansion assays as initial conditions. However, simulations of a spheroid system require some additional assumptions about the system under consideration, in particular, with regard to the regulation of cell proliferation and the oxygen supply. Experimentally proliferation was found to stop throughout the pellets within a few days. After 7 days proliferation activity was localized at the periphery only (Fig. 3.4a). Analyzing the DNA content of the pellets an effective cell loss was observed (Fig. 3.4b). However, from day 7 onwards the number of cells stayed nearly constant. Accordingly, all simulations of the differentiation assay were performed without cell proliferation.

In monolayer culture oxygen can be considered to be abundant. In spheroids oxygen diffuses into the spheroid from its border hence an oxygen gradient is established with decreasing oxygen concentration towards the interior of the spheroid. Consequently, cells in the interior of the spheroid may suffer from a lack of oxygen [9]. For the oxygen consumption rates (C_{O_2} for Eq. (1.24)) of MSCs and chondrocytes a broad range between 1 and 100 fmol/hour per cell was reported [146, 147, 149]. In the simulations the oxygen consumption was assumed to be equal in MSCs and chondrocytes. Consequently, the oxygen gradient within the spheroids does not change during the simulated differentiation process. Thus, the oxygen consumption rate only defines how steep this stable gradient is. In a first order approximation the simulated differentiation processes of the cells depend only on the local available oxygen concentration. Thus, the oxygen consumption rate C_{O_2} can be used to scale

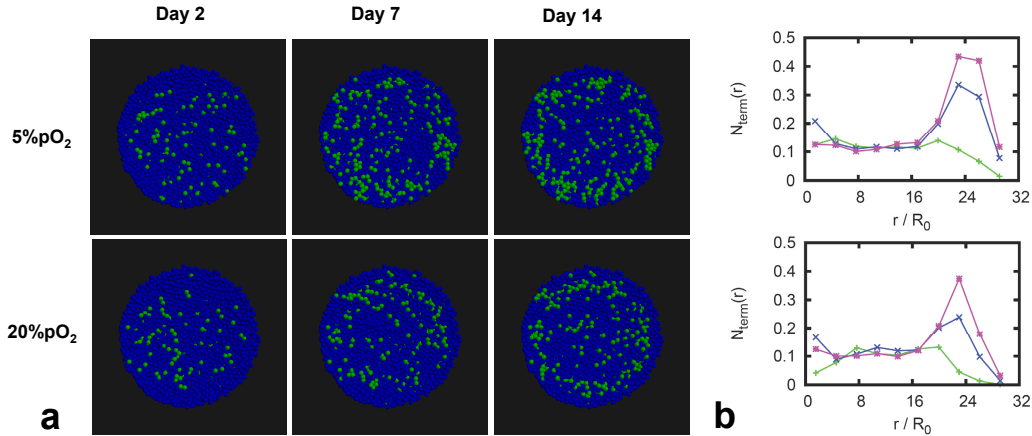


Figure 3.5: Simulated chondrogenic differentiation of MSCs in pellet culture at 20% pO₂. a) Spheroids of cells expanded at 5% pO₂ (upper row) and at 20% pO₂ (lower row). Functional differentiated chondrocytes are shown in green other cells in blue. b) Fraction of chondrocytes vs. radial distance from the spheroid centre at days 2 (green), 7 (blue) and 14 (magenta). At day 14 the total number of chondrocytes in pellets of cells expanded at 5% pO₂ is about 1.5 times larger than in pellets of cells expanded at 20% pO₂.

the width of the observed differentiation pattern in order to match with experimental values. Simulated equilibrium oxygen distributions are shown in Fig. 3.4c,d. In simulation series the dynamics of chondrogenic differentiation of MSCs was analyzed. Thereby, a vanishing chondrogenic lineage activity β_c in the initial populations was assumed. A threshold value of $\alpha_c = 0.5$ for lineage commitment was assumed motivated by the assumption only stem cells and early progenitor cells maintain lineage plasticity.

Assuming sufficiently large lineage transition rates W_0 compared to the basal randomization rate R (see Table A.1) differentiation dynamics was found in qualitative agreement with the experimental results. This is demonstrated in Fig. 3.5 showing the spatio-temporal occurrence of functional differentiated chondrocytes. Stable chondrocyte clusters appear first in a layer beneath the spheroid surface. Accordingly, related chondrogenic matrix synthesis, e.g. of collagen type II, can be assumed to start at the same position in nice agreement with the experimental results. This can be understood as follows. In the central region of the spheroids the differentiation state of the cells fluctuates due to the high noise-amplitudes associated with low oxygen supply (see Eq. (3.2)). Accordingly, cells in this region, although primed for the chondrogenic lineage (Fig. 3.6a,c), do not reach a stable functional differentiated state $\alpha > \alpha_d$. Stable differentiated cells can be frequently found at the periphery of the spheroids where the oxygen concentration is high and the fluctuations low (Fig. 3.6a,b). However, cells at the periphery that were initially in an unspecific differentiated state, stay in this state due to the small probability at high oxygen tension of starting de-differentiation until reaching $\alpha < \alpha_c$ required for switching into the chondrogenic lineage. As a result, these cells do rarely reach a chondrogenic differentiated state. Moreover, they prevent chondrogenic differentiation of neighboring cells by limiting the number of their chondrogenic specified neighbors. Optimal conditions for chondrogenesis are therefore realized within an intermediate layer, where on one hand the probability for lineage commitment and differentiation on the other hand is sufficiently high. Within this layer an oxygen tension of about 10-11% pO₂ was found. This optimal oxygen concentration is quite robust against variation

in the lineage transition rate W_0 and the oxygen consumption rate C_{O_2} (Fig. 3.11).

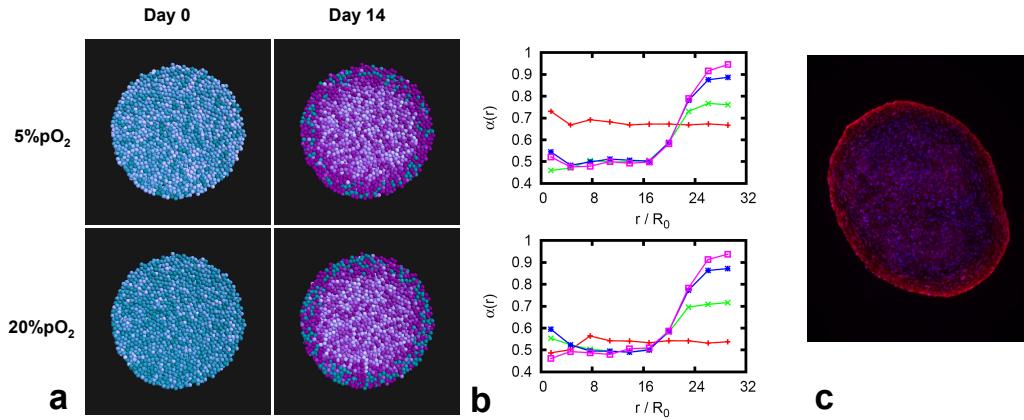


Figure 3.6: Lineage specification of MSCs in pellet culture at 20% pO₂. a) Simulated distribution after 0 and 14 days for cells expanded at 5% and 20% pO₂. Cells committed to the chondrogenic lineage are shown in magenta. Color saturation encodes the differentiation level. Chondrogenic commitment is seen throughout the spheroid except of some cells at the periphery. b) Averaged differentiation vs. radial distance from the spheroid center at day 0 (red), 2 (green), 7 (blue) and 14 (magenta). c) Expression of the chondrogenic transcription factor SOX-9 (red) after 14 days demonstrates the predicted chondrogenic commitment throughout the spheroid. A typical pellet of cells expanded at 20% pO₂ is shown (blue: DAPI staining).

According to the described scenario, the observed differences in the differentiation dynamics between populations expanded at 5% and 20% pO₂ can be mainly attributed to the different number of pre-differentiated cells in these populations. The higher the number of these cells within populations expanded under atmospheric conditions and their maintenance in unspecific differentiation states (Fig. 3.6a) is, thus, suggested to account for the impaired chondrogenesis of these populations. The proposed scenario is not observed assuming a considerable higher threshold value of lineage specification of e.g. $\alpha_c=0.85$ (Fig. 3.10). In this case only the pre-mature senescent cells cannot switch into the chondrogenic lineage. This limitation is too weak to account for the observed significant differences in the differentiation dynamics. Thus, the results suggest that plasticity of MSCs and their progeny with respect to lineage commitment is restricted to stem cells and early progenitors.

3.3.3 Short term exposure of MSCs to low oxygen tension mimics continuous expansion at these conditions

In further simulations the consequences of short term exposure of MSCs to low oxygen were analyzed. For that purpose the dynamics of the de-differentiation process were simulated that occurs in a high oxygen expansion culture (20% pO₂) decreasing the oxygen tension to 5% pO₂. The results predict that the cellular adaptation to the changed environment is already finished after about 24 hours. After this time an equilibrium population structure is reached. Thus, the model predicts that even a short term exposure of MSCs to low oxygen tension should result in an improved chondrogenic potential of these populations. This is in agreement with recent findings by Martin-Rendon *et al.* [132].

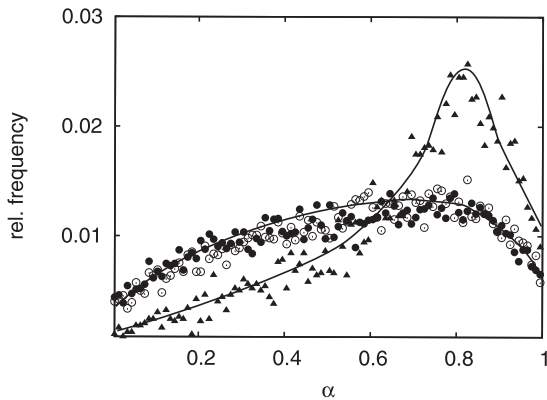


Figure 3.7: Simulation of low oxygen induced de-differentiation of MSCs. The equilibrium distribution of differentiation states in a monolayer population at 20% pO₂ (triangles) approaches the equilibrium distribution at 5% pO₂ (circles) after about 24 hours cultivation under 5% pO₂ (open circles).

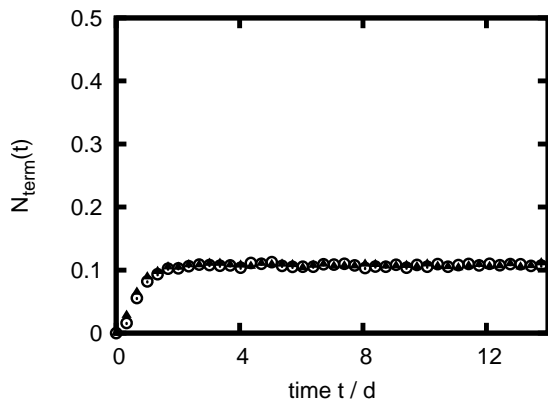


Figure 3.8: Chondrogenic differentiation at 2% pO₂: The number of cells in a functional phenotype saturates after a few hours. Strong fluctuations throughout the culture suppress further differentiation.

3.3.4 Low oxygen tension impairs MSC differentiation

According to the obtained results, low oxygen tension conserves progenitor states. Hence, the lack of oxygen is expected to impair the differentiation process throughout the pellet, and to inhibit the induction of a stable chondrogenic phenotype in all cells. Simulations of chondrogenic differentiation at 2% pO₂ demonstrate inefficient differentiation of the cells. Initially all cells switch into the chondrogenic lineage. This results in a fast saturation period, but due only about 10% of all cells exhibit a functional phenotype (Fig. 3.8). Due to strong fluctuations, in the model no cell stably enters the functional phenotype. This result is in agreement with experimental findings by Malladi *et al.* [134].

3.4 Model Parameters and Robustness

In a first step the model parameters of the monolayer expansion system were adjusted in order to fit the experimental results of the clonal expansion assays at 5% and 20% pO₂. For expansion at 20% pO₂ the best fit was achieved assuming a cell population with a proliferation rate of $r = 1.55/\text{day}$ for each cell. For simulating expansion at 5% pO₂ a good fit was obtained assuming a proliferation rate of $r = 1.55/\text{day}$ for one half and of $r = 2.1/\text{day}$ for the other half of the cells. Since the proliferative activity must be expected to vary throughout the colony, the proliferation rate used in the simulations represents an average. Due to the proliferation enhancing conditions of low oxygen concentrations, this effect is more significant at low oxygen concentrations and is reflected in the assumption of

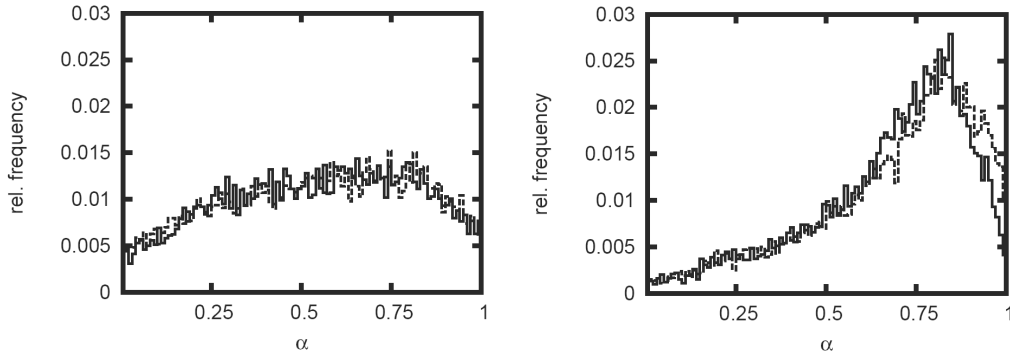


Figure 3.9: Dependence of the distribution of differentiation states on the proliferation rate. Simulation results for expansion at 5% pO₂ (left) and 20% pO₂ (right) are shown. The results for the maximum proliferation rate of 2.1/day (solid lines) used in the simulations are compared with those for the minimum rate of 1.55/day (dashed lines).

a distributed proliferation rate above. Such a moderate increase in the average proliferation rate has little effect on the distributions of the differentiation states as shown in Fig. 3.9.

In a second step the parameter set of the monolayer expansion simulations were used and the additional parameters of the spheroid system adjusted enabling the model to reproduce the experimental data. A fit was obtained assuming a lineage specification threshold $\alpha_c = 0.5$. A threshold $\alpha_c = 0.85$ does not result in a significant difference in the amount of cells differentiated into the functional phenotype between populations expanded at 5% and 20% pO₂. On the other hand $\alpha_c = 0.15$ gives a differentiation process which is much too slow (Fig. 3.10).

Interestingly, the prediction of optimal oxygen tension for chondrogenic differentiation neither depends on explicit choice of the lineage transition rate W_0 nor on oxygen consumption rate C_{O_2} of cells. In all simulations, we found the fraction of cells entering the functional phenotype to peak at about 10-11% pO₂ (Fig. 3.11).

3.5 Discussion

In this chapter a phenomenological individual-based model of MSC differentiation and lineage commitment was introduced and merged with the general model from Chapter 1. On the basis of individual-based modeling with a spatial representation of the cells a panel of experimental results can be explained consistently providing an explanation

1. why low oxygen improves the expansion of MSCs and
2. why MSC populations expanded under low oxygen show an improved potential in subsequent chondrogenic assays.

The key assumptions of the model are that the oxygen environment changes the population structure of expanding MSCs with respect to differentiation and that sufficiently differentiated cells are stable committed. The approach presented here is based on a pedigree free concept of stem cell differentiation [141]. Stem cell and progenitor differentiation are driven by stochastic fluctuations and independently for each agent. Thus, these processes are reversible in general. Recently, this concept of noise driven dynamics was applied to differentiation of promyolytic progenitors and it was demonstrated that it represents an alternative

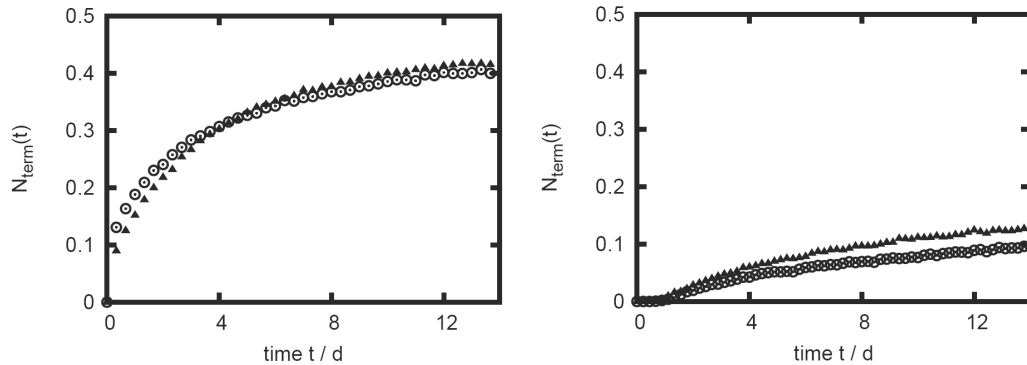


Figure 3.10: Dependence of the terminal differentiation on the lineage specification threshold: For $\alpha_c = 0.85$ (left) no significant difference between the fractions of terminal differentiated cells emerges. Assuming $\alpha_c = 0.15$ (right) does not results in a significant amount of terminal differentiated cells within 14 days. Simulations for cells expanded at 20% pO₂ (open circles) and 5% pO₂ (filled triangles) are compared. Interestingly, the prediction of the optimal oxygen tension for chondrogenic differentiation does neither depend on the explicit choice of the lineage transition rate W_0 nor on the oxygen consumption rate C_{O_2} of the cells. In all simulations the fraction of the cells entering the functional phenotype peaks at about 10-11% pO₂ (Fig. 3.11).

to common molecular network approaches describing cellular adaptation processes [139]. According to the first key assumption high oxygen tension reduces the stochastic state fluctuations (noise) of differentiated states, thereby partly inducing differentiation of the cells. Such a differentiation would also result assuming that high oxygen tension increases the fluctuation of stem cells states. In this case cells stressed by an un-physiological high oxygen tension would increase their potential for phenotypic transitions compared to noise that decreases with increasing oxygen. Here the latter was assumed, such that they become more fixed in their differentiation states.

A different way explaining the impact of the oxygen environment on MSC expansion could be to assume that low oxygen tension strongly increases the proliferation rate of the cells. Accordingly, low oxygen tension would increase the portion of progenitors within the populations as in the simulations presented here. However, proliferation is stopped in MSC pellet culture. As a consequence, differentiation would occur independently of the oxygen tension. This is in contrast to I) the experimental observation that cells in the low oxygen region of the pellet center do not differentiate and II) more general results on impaired chondrogenesis at low oxygen tension by Malladi *et al.* [134].

While the first effect could be explained also by low growth factor or glucose concentrations and related signaling in these regions, the second strongly suggests that a proliferation effect alone cannot explain the impact of oxygen tension on MSC expansion. However, there exists an effect of low oxygen culture on the proliferation rates in that at low oxygen an accelerated selection of fast proliferating cells occurs. Accordingly, further computer simulations were performed to study the effect of a moderately increased average proliferation rate at low oxygen compared to high oxygen tension simulating colony growth. These model details were found to affect the population structure in these assays only marginally. Thus, the observed effects of oxygen tension during expansion on subsequent chondrogenic differentiation are not caused by this selection process. However, long term cell culture may potentiate this effect. Consequently, the ongoing selection of high proliferative cells may become substantial also for the differentiation properties of the populations. According to the

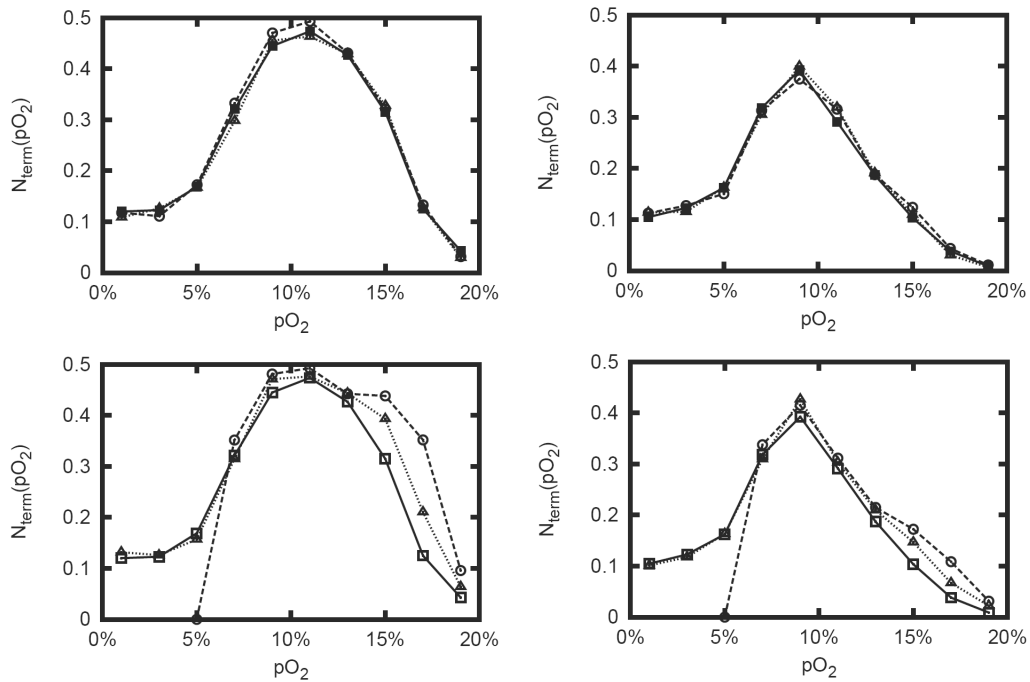


Figure 3.11: Dependence of the terminal differentiation on the lineage transition rate and oxygen consumption rate. The fraction of terminal differentiated cells is shown as function of the oxygen tension for varying lineage transition and oxygen consumption rates. Height and position of the peaks indicating the optimal oxygen tension for chondrogenic differentiation change only slightly. Left: expansion at 5% pO_2 , right: 20% pO_2 . Upper line: The lineage transition rate is varied by an order of magnitude (0.05/s: circles/dashed, 0.01/s: squares/solid, 0.005/s: triangles/dotted). Lower line: Oxygen consumption rates of 65 (open squares), 50 (filled triangles) and 30 fmol/h per cell (open circles) are compared. For 30 fmol/h per cell a minimum oxygen tension of 6% pO_2 was observed in the center of the spheroid.

second key assumption sufficiently differentiated cells stay in their lineage state and are not sensitive to the external stimuli of a differentiation assay. Consequently, a high amount of unspecific pre-differentiated cells impairs the differentiation potential of a MSC population. The model predicts that the accumulation of pre-differentiated cells during MSC expansion can be avoided either by providing stem cell niche-like conditions or by strongly activating proliferation. A complementary strategy would be to induce a chondrogenic priming already in the expansion culture, e.g. by over-expression of SOX-9 [150]. Recent results by Martin-Rendon *et al.* [132] on SOX-9 gene expression indicate chondrogenic priming as a result of low oxygen supply. Clearly, assuming such priming would profoundly increase the effects of low oxygen expansion of MSCs on their subsequent differentiation in this model. Here was demonstrated that low oxygen culture improves their chondrogenic potential independent of such preceding priming. The results predict an optimal oxygen tension for chondrogenic differentiation of about 10-11% pO_2 , which is in the upper range measured at the surface of articular cartilage [151] and below the optimal pressure of about 15% pO_2 found for cartilage formation of rabbit periosteal cells [152]. Advanced chondrogenic assays should ensure high oxygen perfusion to guaranty this oxygen concentration throughout the probe. Presumably these results can be generalized for osteochondral differentiation of MSCs of different origin

and from different species. Oxygen tensions of 2-3% pO₂ used by Malladi *et al.* [134] and D'Ippolito *et al.* [128] are too small and lead to impaired MSC differentiation. A value of about 5% pO₂ may either be comparable [130] or, as found for alginate bead culture [135], even better than 20% pO₂. Expansion at oxygen tensions below 1% pO₂ have been shown to induce adipocyte-like phenotypes in human MSCs [153] and to impair their subsequent osteogenesis [154]. Such behavior cannot be described by the current mathematical model. Here the site of matrix deposition was identified with the position where functional differentiated cells appear and compare the amount of synthesized matrix proteins with the number of these cells. Other models describe processes like that of matrix deposition in more detail [155]. In particular simulations of long term matrix deposition (>14 days) have to account for local accumulation and degradation effects. Such modeling requires detailed knowledge about matrix protein diffusion and degradation as well as cellular production rates. The present study aimed at a better understanding of the basic principles of *in vitro* MSC expansion, differentiation and lineage specification as a pre-requisite of reliable quantitative models of these processes.

4

Individual Fates of Mesenchymal Stem Cells *in vitro*

4.1 Introduction

In Chapter 3 an extension to the IBM has been introduced in order to capture MSC expansion, lineage commitment and differentiation. Based on an IBM realization of the concept of noise-driven stem cell and progenitor differentiation this model links cell plasticity to fluctuations in the differentiation state of each individual cell. Driven by the fluctuations the cells can always gain and lose stem cell properties. A panel of experimental results regarding the oxygen dependence of growth and differentiation of MSC has been consistently explained by this multi-scale computer model. Based on these validated parameters in this chapter the IBM approach further unfolds its advantages and the fates of single cells are analyzed. In contrast to the master equation, which is used as a confirmation of the calculated transition times between differentiation states, the IBM approach not only yields predictions on the plasticity of single cells in terms of the transition times, but also on composition of the stem cell pool and impact of biophysical parameters on differentiation structure via contact inhibition. The computation of the master equation was contributed by Martin Hoffmann.

Generation and maintenance of replenishing tissues relies on appropriately regulated balance between self-renewal and differentiation within a relatively small population of stem and progenitor cells. The structure of these populations is strongly influenced by environmental factors such as specific cell-cell interactions, growth factor and oxygen supply, as well as the geometry and mechanical properties of the local environment. Accordingly, changes in the environment lead to changes in cellular activity at the level of signaling, metabolism and gene expression over periods of hours or days [156, 157]. Recent evidence from both experimental and modeling initiatives indicates a high degree of heterogeneity and dynamic transition within stem and progenitor populations [115, 120, 158]. There is an ongoing debate on the fundamental dynamics underlying this kind of heterogeneity. A thorough understanding of stem and progenitor cell dynamics constitutes a prerequisite for the quantitative modeling of stem cell organization and computational tissue applications and is expected to make an important contribution to the development of novel therapeutic strategies for treating degenerative disease, injury and neoplasia.

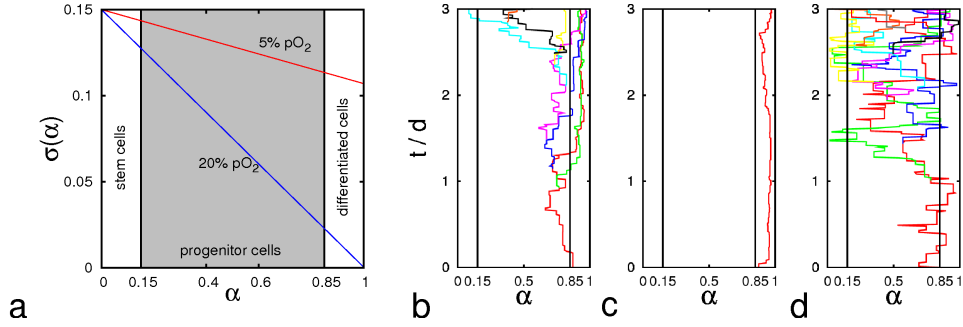


Figure 4.1: Noise profiles and typical genealogies of expanding clones. a) Shown are the two noise profiles for 20% and 5% pO_2 as used in the simulations. b-d) Genealogies for clones descending from cells starting at differentiated states $\alpha > 0.85$. b) At 20% pO_2 clones enter proliferative states only on rare occasions, but if so, they are able to give rise to an ample progeny. c) At 20% pO_2 most of these cells do not enter the proliferative states and stay quiescent. d) In contrast cells at 5% pO_2 enter proliferative states much more frequently and thus, clones grow much faster.

4.2 Simulation Strategy

Individual cell-based model The main advantage of individual cell-based simulations is, that they provide data on the level of individual cell and therefore on functionally relevant outliers. In order to unravel the contributions of single cells to the differentiation structure of the population, mean passage times into differentiated and stem cell states are calculated under different conditions. They can be seen as indicators of single cell plasticity and allow conclusions on population plasticity. Regeneration of the differentiation structure of populations from defined sub-populations is simulated and analyzed considering single clones. The question how cell interactions can affect differentiation is addressed by varying biophysical simulation parameter. Importantly, all parameter used are validated and the computer simulations correspond "one to one" to MSC protocols *in vitro* and, thus, can in principle directly be tested.

Master equation approach In addition to the stochastic individual cell-based approach a deterministic population dynamics model is used as previously described [139]. Here, the deterministic model is applied for studying the population average of dynamic properties of individual cells, therefore cell proliferation is not included. The model is then equivalent to a master equation for a Markov process [98] describing the dynamics of the average number of cells $N(\alpha)$ in state α :

$$\frac{1}{R} \frac{\partial N(\alpha(t))}{\partial t} = \int_0^1 p(\alpha|\bar{\alpha}) N(\bar{\alpha}, t) d\bar{\alpha} - N(\alpha, t) \quad (4.1)$$

with the same randomization rate R and transition probability given in Eq. (3.1) as in the IBM. Transition times $\tau(\alpha)$ from an initial α into the regimes of stem cells ($\alpha < \alpha_s$) or differentiated cells ($\alpha > \alpha_d$) were computed using an absorbing boundary approach [159].

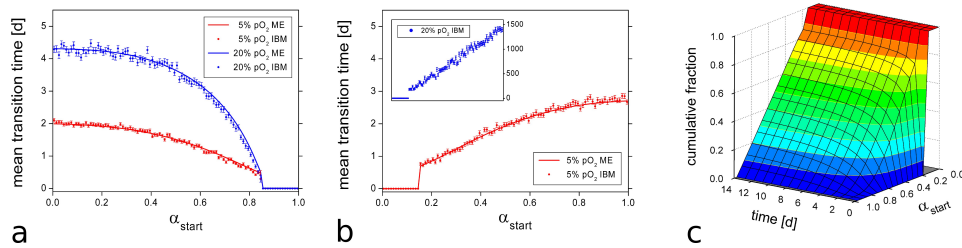


Figure 4.2: Individual cell dynamics. Mean transition times calculated by the IBM and the master equation approach (ME) to reach a) differentiated states and b) stem cell states at 5% (red) and at 20% pO₂ (blue). The transition time to stem cell states at 20% pO₂ was not calculated using the ME because the cumulative fraction of cells that have reached stem cell states converged too slowly (see c). Symbols: IBM results, Lines: Master equation. c) Fraction of cells that reach stem cell states at 20% pO₂ as a function of initial α and simulation time (ME).

4.3 Results

4.3.1 Monitoring individual cell fates

Using the IBM approach the fates of individual cells in growing populations can be monitored. Cell trajectories regarding differentiation dynamics under different culture conditions were generated and compared for low (5%) and high (20%) oxygen concentrations. Fig. 4.1 shows the noise profiles for these concentrations and results for selected clones. In order to quantify the degree of plasticity that is inherent in MSCs the average time required to adopt specific cellular phenotypes was calculated. The average transition times of a cell to reach stem cell states ($0.0 < \alpha < 0.15$) and differentiated states ($0.85 < \alpha < 1.0$) were calculated as follows: In the IBM 100.000 cells with α values equally distributed in the interval $[0, 1]$ were subjected to stochastic state fluctuations. Throughout the simulations cells that reached the specified sub-population were counted and histograms about their initial state were derived. From these histograms were calculated i) average transition times (Fig. 4.2a, b) and ii) the fractions of cells that successfully transferred within a defined time.

The results demonstrate that at low oxygen a frequent exchange between the sub-populations occurs at a time scale of 2 days. At high oxygen the average transfer time for stem cells into the pool of differentiated cells increases to about 4 days. Transfer times for differentiated cells into the stem cell pool at high oxygen are much larger (> 100 days), indicating quasi deterministic cell differentiation behavior. Applying the master equation approach confirmed the results obtained by the IBM. In Fig. 4.2c the fraction of cells having entered the stem cell pool at 20% pO₂ is shown as a function of initial value and simulation time. Only in this particular case the fraction of absorbed cells grows too slowly to calculate the average transition times. In the three other cases they were computed with high precision (less than 10^{-12} of all cells remain to be absorbed).

In vitro validation of the above results would require single cell tracking of MSCs and techniques to identify the differentiation state of the tracked cells. Currently, considerable effort is taken in order to establish tracking techniques for stem cell systems [160, 161]. Unfortunately, MSCs are particularly hard to track, because they tend to aggregate; a phenomenon known as mesenchymal condensation [100, 162]. Thus, in the following results on MSC plasticity are presented seen on the population level which can be validated in simpler experimental setups.

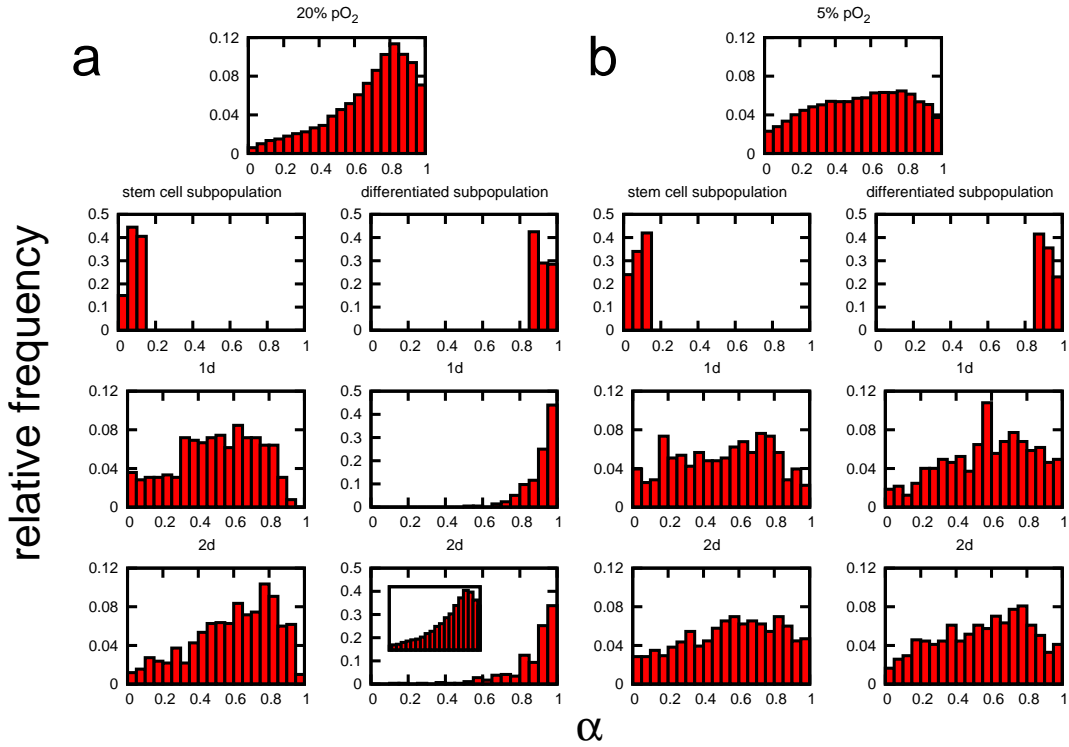


Figure 4.3: Simulated regeneration of the population structure. Shown are results for a representative regeneration simulation (a) at 20% pO_2 and (b) at 5% pO_2 . For each oxygen concentration the regeneration from stem cells (left) is compared to regeneration from differentiated cells (right). The insert shows the regenerated population structure after 8d.

4.3.2 Regeneration of the population structure

Chang *et al.* [120,158] studied how fast the distribution of differentiation marker expression within a cell population regenerates from sub-populations with defined expression level. They performed the following experiment: a population of precursor cells was generated under standard conditions and characterizes by the expression level of a particular differentiation marker. Sub-populations of cells with defined expression levels of the differentiation marker were separated. These sub-populations were cultivated under standard conditions and regeneration of the distribution of expression levels in the population was monitored over time by FACS.

Population regeneration was simulated as follows: Starting from a population that was equilibrated at low density, i.e. which shows no signs of contact inhibition of growth, selected 200 stem cells and 200 differentiated cells were selected and their development followed over 8 days in secondary cultures. Again the MSC behavior was compared at low and high oxygen tension. Fig. 4.3 shows the results for a selected realization.

At low oxygen the population structure is roughly regenerated by stem cells and by differentiated cells within about 1 day. At high oxygen the population is regenerated in about 2 days by stem cells, but it takes about 8 days if starting with differentiated cells. However, this is still a surprisingly short time taking into account the large transition times for differentiated cells into the stem cell pool. This phenomenon can be understood by

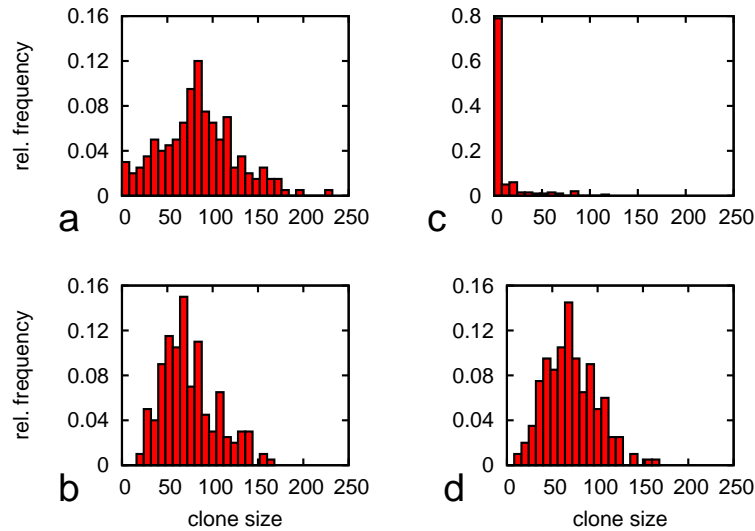


Figure 4.4: Clonal development during the regeneration. Shown are the size distributions of 200 clones grown from stem cells (a,b) and differentiated cells (c,d) after 5 days of secondary cultivation. Upper row: 20% pO₂. Lower row: 5% pO₂.

analyzing the clone size distribution of the clones evolving from the 200 initial cells. This distribution is shown in Fig. 4.4. Except for regeneration from differentiated cells at high oxygen the distribution peak is located at about 50-100 cells per clone, demonstrating that most of the clones started to grow. In the remaining case where differentiated cells were cultured at high oxygen, most of the cells remain quiescent throughout the observation time (137 out of 200 in Fig. 4.4c and only a few cells started to proliferate and formed large clones. This means the regeneration is driven by the progeny of these few cells only.

4.3.3 Linking biomechanics and differentiation

At the center of expanding MSC clones proliferation becomes contact inhibited. The quiescent region grows with colony size until all cells will stop proliferation, when an expanding *in vitro* culture becomes confluent. Such changes in proliferation activity impact the population structure of MSC colonies. Fig. 4.5 compares the α -distributions of different MSC populations at high oxygen (20% pO₂). Shown are the α -distributions in a low density population without any sign of contact inhibition, in growing clones with weak and strong contact inhibition induced by variation of the cell-substrate friction constants and in a confluent and thus quiescent population. The fraction of differentiated, non-proliferative cells ($\alpha > \alpha_d$) increases from about 25% in the low density population to about 90% in the confluent population. A comparable induction of spontaneous differentiation in MSC can be observed *in vitro* (per. communication, A. Stolzing). These simulation results implicate that if regeneration refers to the growth of a few large clones, as in the case of differentiated cells at high oxygen, the effect of contact inhibition becomes more relevant for population regeneration. The α -distribution in large clones significantly differs from that of a low density culture. Moreover, due to the increased number of differentiated cells, these populations show a lower CFU capacity (compare [97]).

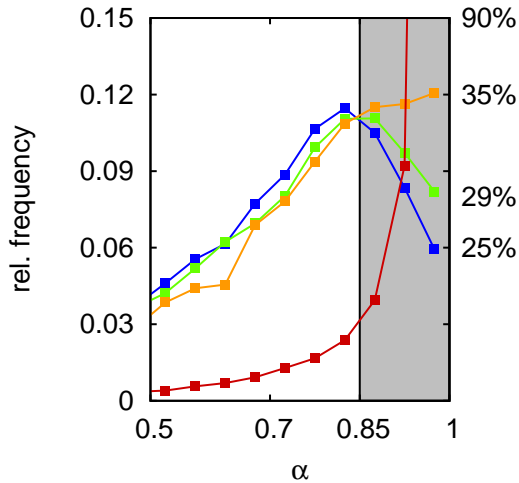


Figure 4.5: Impact of contact inhibition of growth on regeneration. The figure shows the equilibrium distribution of differentiation states without contact inhibition of growth (red) and without proliferation (cyan) at 20% pO_2 . For comparison two additional distributions obtained for cells with low (green) and high (blue) cell-substrate friction are shown. These distributions refer to regeneration experiments from differentiated cells after 7.5 days.

4.3.4 Modeling the organization of the stem cell pool

Additional information on MSC plasticity *in vitro* can be obtained by performing the regeneration experiments described above in parallel for all sub-populations. Splitting the mother population into a number of sub-populations according to the expression of a differentiation marker, applying the ‘regeneration protocol’ suggested above to each of these sub-populations and quantifying the number of stem cells in each sub-population after a fixed regeneration time would allow to quantify the fraction of stem cells in a MSC population descending from a particular sub-population.

In additional simulations this concept was followed. However, instead of splitting the mother population into sub-populations, each individual cell of the mother population was separated and expansion of the clones generated by the individual cells was followed. For different time points we quantified the clonal composition of the common stem cell pool ($0 < \alpha < \alpha_s = 0.15$) of all clones in terms of the initial values of the cells that induced the clones. Fig. 4.6 shows this clonal composition of the stem cell pool after 5 days of clonal expansion. At low oxygen (5% pO_2) the fraction of stem cells that originate from stem cells is about 11%. At high oxygen (20% pO_2) this fraction decreases to only 5%. In both cases most of the cells in the stem cell pool originate from progenitor cells. At low oxygen tension all progenitors equally contribute to this pool, while at high oxygen tension most cells originate from progenitors with a high α value between 0.7 and 0.8.

4.4 Discussion

Recent experimental findings indicate that cells can regain stem cell properties under defined environmental conditions. These results challenge the commonly agreed stem cell paradigm. This paradigm treats ‘stemness’ as a fixed property essentially intrinsic to stem cells and assumes a deterministic and irreversible differentiation scenario for each cell [163]. As an alternative a novel concept of functional stem cells has been developed that assigns the interaction between cells and their growth environment a greater emphasis [141, 164]. This concept does not exclude certain preferred trends in the differentiation sequence, but enables reversible developments for individual cells. Here the first quantitative predictions on the environmental dependent plasticity of MSCs *in vitro* are provided applying this novel

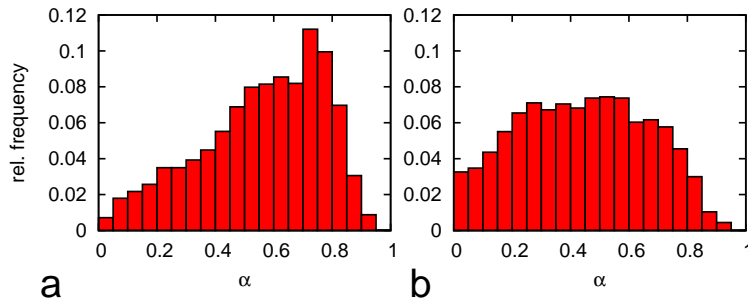


Figure 4.6: Simulated clonal competition in the stem cell pool. The histograms show the composition of the stem cell pool ($0 < \alpha < 0.15$) regarding the origin of each cells clone for populations expanded at a) 20% and b) 5% pO₂ for 5 days.

concept. The predictions cover: i) the average transition times of individual cells into stem cell and differentiated states, ii) the time scales of the regeneration of the distribution of differentiation marker expression in a MSC population from sub-populations of stem and unspecific differentiated cells, and iii) the origin of the cells forming the *in vitro* stem cell pool of MSC. Moreover, they state that all these properties depend on the environment. The results also provide estimates of the time scales of MSC adaptation to changed environmental conditions. Thereby, the results are in good agreement with experimental findings demonstrating that changes in the oxygen environment force an adaptation of MSC behavior within 24 hours only [132].

In all simulations an oxygen dependence of the state fluctuations was considered. In contrast, biophysical features, as cell-cell and cell-substrate interactions, were assumed to affect the regenerative potential of the MSC by interfering with their proliferation control mechanisms only. A direct feedback of these interactions on the noise amplitudes was not considered. However, recent results demonstrate that lineage specification and proliferation of MSC populations can be triggered by substrate elasticity [48] and substrate micro-structure [33]. Thus, a suggestion is to perform the proposed experiments on MSC plasticity on substrates that vary with respect to their elasticity and micro-structure. These experiments would provide information on whether mechano-signaling can affect the kinetics of state transitions in MSCs and thus, can be used to time regeneration processes *in vitro*. The results on the composition of the stem cells pool suggest that most of the stem cells in MSC populations expanding *in vitro* originate from progenitor cells. Thus, their mother cells underwent differentiation and de-differentiation processes and were proliferative active. Recent experimental results suggest that these cellular activities result in changes in the cellular phenotype called stem cell aging [165]. A model that attempts to consistently describe these phenomena is proposed in the following chapter. Most of the results could be validated by *in vitro* experiments on the population level. A number of suggestions were given in the course of this chapter. However, more detailed studies would require tracking of individual cell fates in a single expanding MSC population. Such experiments would provide additional information on cell-cell communication in the expanding population, which was suggested to impact MSC expansion [166]. As already mentioned above, the tracking of MSC involves particular problems. Long term monitoring of MSC fates will require therefore sophisticated marker systems for both the clonal origin and the differentiation state of the cells. A number of stem cell and differentiation markers of MSC have been suggested. Good candidates are early transcription factors [144, 167]. Long-term fluctuations in differentiation marker

expression in single cells would directly proof the concept of noise-driven stem cell organization. For the generality of this concept, we expect such fluctuations to underlie somatic stem cell organization independent of tissue and species.

By the novel results presented in this chapter the general suitability of the IBM approach for studying the organization of stem cell populations is demonstrated. Stem cell maintenance, expansion and environmental adaptation may in particular rely on single cell plasticity and therefore understanding single cell behavior is pre-requisite to unveil the general principles of the organization of stem cell populations. For addressing such questions, IBM provides the natural concept by representing the population as the union of individual cells.

5

Differentiation, Aging and Senescence

5.1 Introduction

In this chapter an additional property of individual cells is introduced in order to model clonal heterogeneity of MSCs. Based on the hypothesis, that ‘age’ is responsible for this heterogeneity, the differentiation dynamics is assumed to depend on the cell’s history. This assumption introduces another property of biological systems, that qualifies individual or agent-based modeling for studying them. The cells are assigned a memory for their history. Moreover, the age in terms of divisions depends via contact inhibition on the spatial variation of pressure and closely links biomechanics and regulation in a different way, than proposed in the last chapter. The experimental results were contributed by Matthias Zscharnack, Center for Biotechnology and Biomedicine, University of Leipzig and Alexandra Stolzing, Fraunhofer Institute for Cell Therapy and Immunology, Leipzig.

The organization of tissue stem cells is still a matter of debate. The ‘pedigree concept’ of stem cell organization treats ‘stemness’ as a fixed property essentially intrinsic to stem cells. It is based on observation of hierarchical arrangements of regenerating tissues. However, experimental findings dealing with tissue plasticity phenomena have indicated that cell- environment interactions can actually influence stem cell organization in a variety of ways leading to the development of novel stem cell concepts [141]. These concepts assign the interaction between cells and their growth environment a greater emphasis. However, they do not exclude certain preferred trends in the differentiation sequence, but they enable reversible developments for individual cells, allowing the system to flexibly react to changing demands. According to these concepts a fundamental property of stem cell populations is their dynamic functional heterogeneity. In the models by Roeder and co-workers [115, 140] individual cells gain and lose stem cell properties depending on whether they are in quiescent or proliferative states, respectively.

Therapeutic applications of autologous MSC require an excessive *in vitro* expansion of the isolated cells [168, 169]. For this purpose various culture protocols have been suggested

in order to isolate stem cells with high regenerative potential [170–172]. However, it has been demonstrated that such massive MSC replication is unavoidably associated with continuous changes of the cell’s functional competence. During expansion the MSC show a decreasing proliferation potential [171,173]. Moreover, the efficiency of differentiating into local tissue after transplantation was found to severely decrease during expansion [174]. In summary these phenomena have been described as ‘*in vitro* aging’ of MSC [165].

The underlying cell intrinsic processes as well as the induced heterogeneity were not considered in our previous approaches to MSC culture. Senescence has been implicated as a major cause of this decline in MSC function [175]. The accumulation of this phenotype, as in replicative senescence, has been demonstrated to be a continuous process in MSC [176]. Interestingly, expansion at low oxygen pressure and low glucose culture decreases the number of accumulating senescent cells compared to high oxygen pressure and high glucose culture, respectively [148,165]. Recent experiments demonstrated that artificial *in vitro* aging and *in vivo* aging of MSC induce related changes on the cellular as well as on the molecular scale [177,178]. Under homeostatic conditions, there are limited demands on the self-renewing stem cells *in vivo* and so these cells divide infrequently, sparing them the perils of DNA-replication and mitosis. However, under regenerative stress the metabolic activity of *in vivo* stem cells increases and becomes comparable to that of their *in vitro* counterpart. In both cases the stem cells are exposed to higher levels of DNA-damage-inducing metabolic side products such as reactive oxygen species (ROS) [179]. It has been suggested that the damages produced thereby induce not only aging of the stem cells but of the whole organism. In fact, excess replicative demands alone can induce progeroid phenotypes [180]. However, whether replication itself or actually the subsequent induction of damages impairs stem cell function remains to be determined.

In the following experimental results on the clonal heterogeneity of MSC populations from different species are presented, demonstrating persistent individual heterogeneity on long time scales. This heterogeneity is related to a functional decline in individual MSC during *in vitro* expansion by an additional term in the noise driven differentiation of the hybrid model used in Chapter 3 and 4. ‘MSC aging’ is modeled by de-stabilizing stem cell states in course of each cell division. It is demonstrated that the model is capable of both explaining the clonal heterogeneity regarding MSC expansion *in vitro* and the experimentally observed differences in the chondrogenic potential of the individual clones. Moreover, the model predicts *in vitro* and *in vivo* aging to base on the same principles.

Regarding *in vitro* aging our computer simulations are again closely following standard culture protocols to enable hypothesis-driven research. In this way, the finally provided hypotheses are experimentally testable and can be expected to give further insight into *in vitro* and *in vivo* stem cell heterogeneity and aging.

5.2 Experimental Results

5.2.1 Clonal heterogeneity of MSC *in vitro*.

The growth of rat, ovine and human bone-marrow derived MSC was investigated. First, single-cell derived clones of passage one (P1) were generated by the limited dilution method. In order to support efficient colony forming hypoxic conditions were used [148]. After 5 days of growth at 5% pO₂ the number of cells of the individual clones were counted. As shown in Fig. 5.1a, a broad distribution of the individual clone sizes was found for all three species investigated, indicating heterogeneity in the initial exponential expansion of the clones. Interestingly, selected clones continued growing at different rates also in the next passages

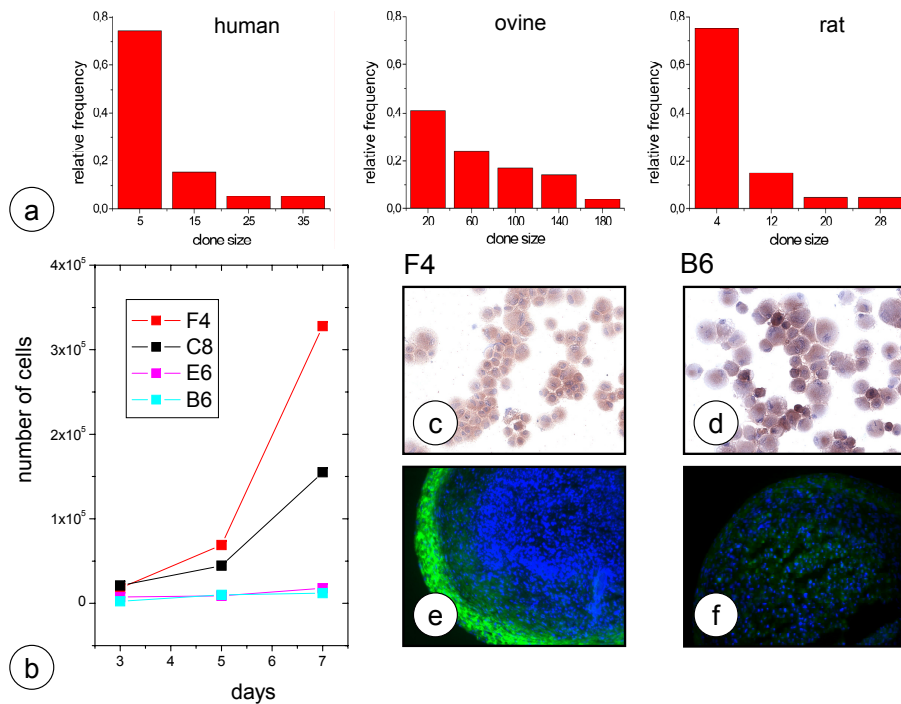


Figure 5.1: Properties of single cell-derived MSC clones. a) Distribution of the size of individual clones of human, ovine and rat MSC after 5 days in P1. b) Growth behavior of 4 selected ovine MSC clones 4 in P3 (initially 10^4 cells). c, d) Spontaneous pre-differentiation of a fast (F4) and a slow (B6) proliferating clone in monolayer culture as demonstrated by aggrecan staining (Cytospins). Only the slow proliferating clone shows a clear positive staining (dark brown). e, f) TGF- β induced chondrogenesis in pellet culture. Aggrecan staining (green) following 14 days of culture is prominent only in the pellet derived from cells of the fast proliferating clone. DAPI: blue.

(P2, P3) under standard culture conditions (20% pO₂). Thus, the clonal heterogeneity is inherited over many generations independent of environmental oxygen. This is demonstrated in Fig. 5.1b showing the growth behavior of 4 ovine clones selected out of 36 in P3. Subsequent to expansion the rate of both spontaneous pre-differentiation in monolayer culture and TGF- β induced chondrogenic differentiation in pellets was analyzed using established markers including SOX-9, aggrecan, and collagen II. Slow proliferating clones showed a clear tendency for spontaneous pre-differentiation, while fast proliferating clones did not (Fig. 5.1c,d). In contrast only fast proliferating clones did undergo effective chondrogenesis in pellet culture (Fig. 5.1e,f). These properties appeared to change continuously with the proliferation capacity in agreement with Wagner *et al.* [176]. No evidence for a critical, switch-like behavior in the ovine MSC was found. Rat and human MSC showed comparable behavior demonstrating that persistent functional heterogeneity is a general feature of MSC clones. Assuming that the observed heterogeneity has a functional component, one would expect that each of the individual clones provides specific growth signals and consequently affects the growth behavior of the population containing all clones (MIX). Thus, additional measurements on ovine MSC were performed analyzing whether the common mother population of selected clones shows significant growth benefits compared to the individual clones.

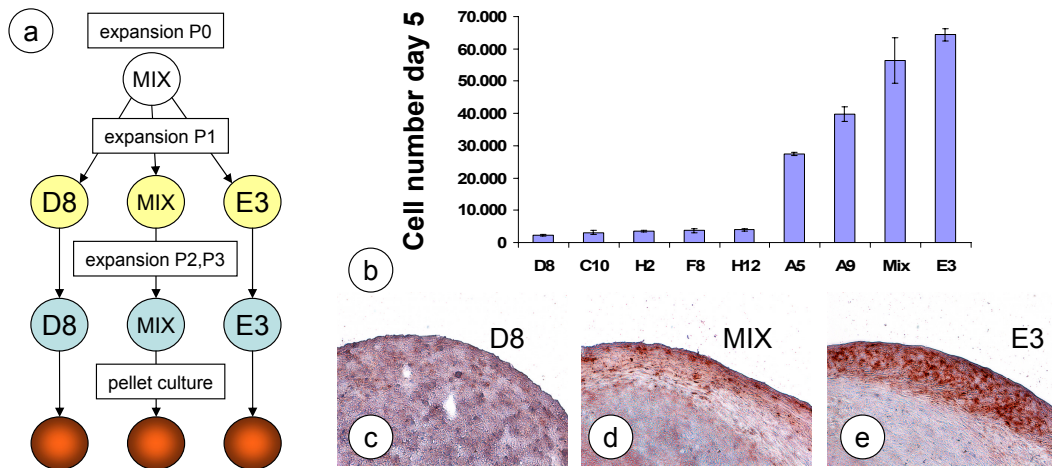


Figure 5.2: MSC clones grow independently. a) Schema of the experiment. b) Number of cells grown from 750 cells after 6 days of culture. The results for 8 out of 36 clones are compared with the result for the mixed population (MIX). Clone E3 grows faster than the mixed population. c-e). Comparison of the chondrogenic potential of the slowest clone D8, with those of the MIX and E3 by histological staining for aggrecan. After 14 days of culture only the MIX and E3 show a positive staining, which is more pronounced in E3.

As demonstrated in Fig. 5.2 neither a growth benefit nor an improved chondrogenic potential of the mixed population and therefore no evidence for a functional heterogeneity being conserved *in vitro* was found.

5.2.2 Spatial heterogeneity of MSC populations.

In subsequent studies, the spatial organization of MSC populations *in vitro* was analyzed. Fig. 5.3a-f shows results obtained for human MSC of P0. These cells formed large colonies at both 5% and 11% pO₂ (Fig. 5.3a,b). Following 14 days of culture the colonies were stained for aggrecan. A clear staining was only observed at the periphery of the colonies at 11% pO₂. Although more dense, the center of these colonies showed no staining. At 5% pO₂ clear staining was observed neither at the periphery nor at the center of the colonies. This demonstrates an increasing tendency for spontaneous pre-differentiation with oxygen tension in expansion cultures in agreement with former results on ovine MSC (see Chapter 3, [148]). Ovine and rat MSC did not show clear aggrecan staining at P0.

5.3 Modeling Stem Cell Organization and Aging *in vitro*.

In order to explain the phenomena of persistent clonal and of spatial heterogeneity in MSC populations the noise-driven approach to stem cell dynamics introduced in Chapter 3 is modified. The model explained the observed dependencies of MSC growth and differentiation on the oxygen environment most satisfactory. However, it did not consider an intrinsic and persistent type of heterogeneity or individuality. Thus, any initial difference between two single cell derived clones in Chapter 3 is based on random initial fluctuations and vanishes if they grow to larger cell numbers. Therefore, the experimentally observed persistent hetero-

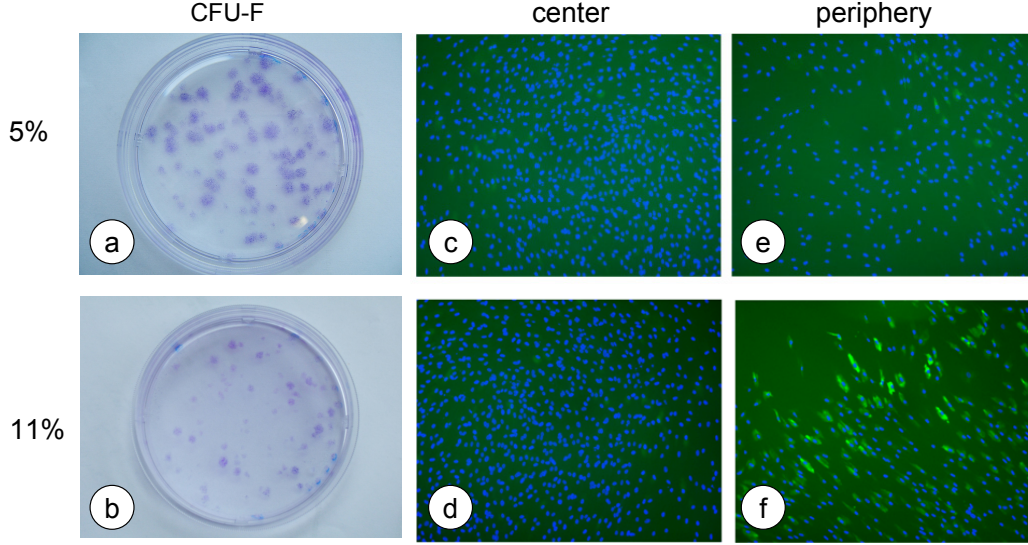


Figure 5.3: Spatial heterogeneity of human MSC colonies. Shown are P0 colonies at 5% (upper row) and 11% pO₂ (lower row). a),b) CFU-F assay. c)-f) Spontaneous pre-differentiation is demonstrated by aggrecan staining (green). c),d) After 14 days of culture staining was negligible at the center in both oxygen environments. e),f) At the periphery staining was weak for 5% and substantial for 11% pO₂. DAPI: blue.

genicity of clones comprising more than 10^4 cells (compare Fig. 5.1b) cannot be described by the model. Thus, the noise driven concept of the model is kept and the dependence of the fluctuation strength $\sigma(\alpha)$ is impacted by the environment; oxygen still sets the mean noise amplitude. But it is extended by the assumption that stem cell states become de-stabilized with ‘age’ resulting in an increased tendency for spontaneous pre-differentiation. This scenario is modeled assuming that the noise amplitude $\sigma(\alpha)$ of a cell depends on the generation number m (Fig. 5.4a). For daughter cells j and k of cell i holds: $m_j = m_k = m_i + 1$. The resulting time dependent noise amplitude $\sigma(\alpha, m)$ of a cell of age m and differentiation α contributing to a MSC population *in vitro* is given by:

$$\sigma(\alpha, m) = \sigma_0 [1 - \alpha f(E)] + mr_D [1 - 2\alpha] \geq 0. \quad (5.1)$$

The first term on the right hand side defines the extrinsic, environmental determined noise amplitude as in Chapter 3. Here, σ_0 denotes the noise amplitude for initial stem cells, and $f(E)$ is a function determining the change of this amplitude with differentiation in dependence of the environment. In Chapter 3 $f(E)$ was given as the Hill function $h(pO_2/pO_2^{\max})$, here it is changed to:

$$f(E) = 2(1 - \sigma_E/\sigma_0), \quad (5.2)$$

where σ_E is the mean noise amplitude in a defined environment E. The second term on the right hand side in Eq. (5.1) defines the effects of aging. Thereby, r_D is the rate of de-stabilisation of stem cell states per cell division. The ‘age’ of a cell is given by $\sigma(\alpha = 0)$. If the noise amplitude of a cell becomes zero at $\alpha = 1$ it is assumed to become time independent. This occurs if the generation number of a cell reaches:

$$m_{RS} \equiv m(\sigma(\alpha = 1) = 0) = (2\sigma_E - \sigma_0)/r_D \quad (5.3)$$

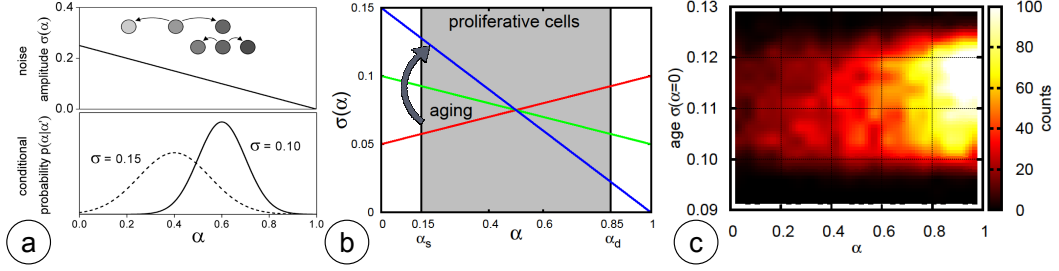


Figure 5.4: Model of population heterogeneity. a) Stem cell aging and proliferation. The noise amplitude of stem cell states $\sigma(\alpha = 0)$ increases with each cell division. In grey: proliferative active states α_p with $\alpha_s < \alpha < \alpha_d$. b) Distribution of cells of generation m and differentiation state α . Shown is an example of an *in vitro* population at 11% pO₂. The frequency of pre-differentiated cells increases with age.

For the chosen parameter sets this generation number ranges between 20 and 70. At m_{RS} the cells show a strong tendency to pre-differentiate and to stay quiescent. Thus, one can relate m_{RS} to replicative senescence. m_{RS} depends on the environment and in particular on the oxygen tension. For human and rat MSC isolated using plastic adherence 20 divisions are required to reach that limit at 20% pO₂. At 5% pO₂ this number increases to 48. These results roughly agree with experimental findings, which strongly depend on the donor (20% pO₂, [176], 20% and 3% pO₂, [181]). Ovine MSC were found to be even more sensitive to oxygen [148]. The heterogeneity of a population can be monitored by the probability distribution to find a cell of age $\sigma(\alpha = 0)$ and in state $\alpha = 1$ (Fig. 5.4b). Within an expanding population the probability to find spontaneous differentiated, quiescent cells ($\alpha > \alpha_d$) increases due to the increasing number of division per cell on average. This effect is independent of the environment. Importantly, we assumed a proliferation stop in dense culture [182]. Thus, quiescent cells in dense regions of the population do not ‘age’. Table A.3 summarizes the parameters of the aging model used in our simulations.

5.4 Simulation Results

5.4.1 Spatial age-structure of MSC colonies *in vitro*.

In a first step the age-structure of colonies growing from a single stem cell ($\sigma_0 = 0.100$) was simulated. A radial age- profile formed across such colonies with the youngest cells being located at the center of the population (Fig. 5.5a). This profile originates from stalled proliferation at high cell density and, thus, represents a general feature of the biophysical model from Chapter 1. The differentiation profile in the growing colonies depends on the specific time scales of proliferation, differentiation and aging. Fig. 5.5b,c show examples of such profiles. Here, the parameter set was adjusted to obtain a profile similar to that of human MSC seen in Fig. 5.3c-f. At 11% pO₂ aged cells at the periphery are most differentiated and minimal differentiation occurs near the center of the colony. Decreasing the oxygen tension to 5% pO₂ increases the amplitudes of the cellular state fluctuations. In this case cells do not reach stable differentiated states and their average differentiation decreases in the whole colony. These results demonstrate that the presented model is capable of describing spatial heterogeneity of clonal MSC populations.

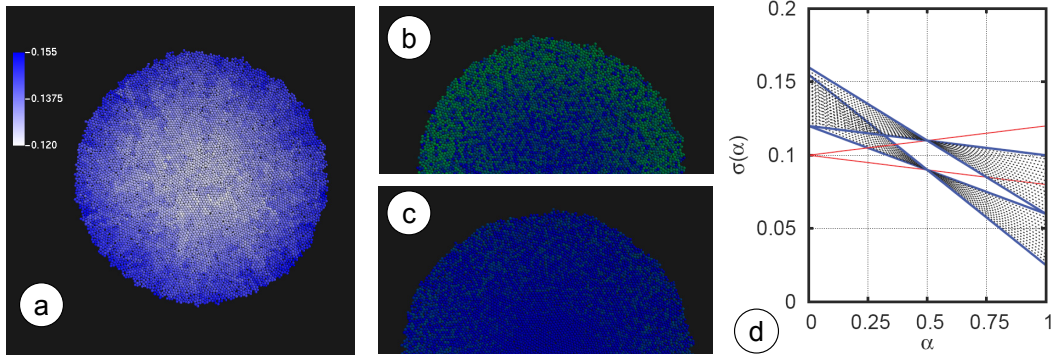


Figure 5.5: Simulated age-structure of MSC. a) Spatial age-structure. The Color code indicates aging in terms of $\sigma(\alpha = 0)$ ranging from 0.120 to 0.155 corresponding to 8...22 *in vitro* cell divisions. b,c) Radial profile of the average differentiation at b) 11% and c) 5% pO₂. The strongest spontaneous pre-differentiation is found at the periphery. d) The population heterogeneity with respect to age is encoded in the variance of the noise amplitudes of all contributing cells (upper and lower set correspond to 5% and 11% pO₂). Red: noise profiles of the mother cells.

5.4.2 Functional heterogeneity of MSC *in vitro*.

Based on the results on the age structure we simulated functional heterogeneity of MSC clones in a second step. For that purpose we selected 30 cells of defined age $\sigma(\alpha = 0) = 0.1, 0.125, 0.15$. They were taken from colonies of average age $\sigma(\alpha = 0) = 0.1, 0.125, 0.15$, respectively, which are expected to occur in P0 due to *in vivo* heterogeneity. Colony growth of the selected cells was simulated over 7 days at 20% pO₂. Fig. 5.6 shows the results of simulation using the ovine MSC parameter set. The simulated growth curves (Fig. 5.6a) reproduce the behavior found *in vitro* (Fig. 5.1b). Younger clones grow faster than older clones. In agreement with the experimental results slow growing clones in the simulation showed a strong tendency for pre-differentiation, while fast growing clones did not (Fig. 5.6b). These cells of the simulated expansion were used for induced chondrogenic differentiation in pellet culture applying the model of functional differentiation introduced in Chapter 3. The number of chondrogen differentiated cells was found to be highest in pellets that of cells of intermediate proliferating clones (Fig. 5.6c). Considering that cells in P2 and P3 have undergone about 20- 30 cell divisions and accordingly no cells of age $\sigma(\alpha = 0) < 0.125$ can exist, the results qualitatively reproduce the experimental findings on reduced chondrogenic potential in slow proliferating MSC (Fig. 5.1e,f). Thus, functional heterogeneity of MSC clones is covered by the presented aging concept. Note that age differences that typically develop in a single colony in P0 (10 divisions) are sufficient in order to explain the observed heterogeneity. However, this does not exclude the presence of *in vivo* heterogeneity.

5.4.3 Aging of MSC *in vivo*.

Finally, model is used to predict dynamics of *in vivo* aging. The bone marrow constitutes a MSC niche that conserves stem cell states [183]. Accordingly, the mean noise amplitude in the niche was assumed to be a strongly stem cell conserving environment ($\sigma_E = 0.15$, Fig. 5.7a). Cell division in the niche increases the stem cell noise amplitudes and thus, changes the population structure. Thereby, the proliferation activity increases as long as

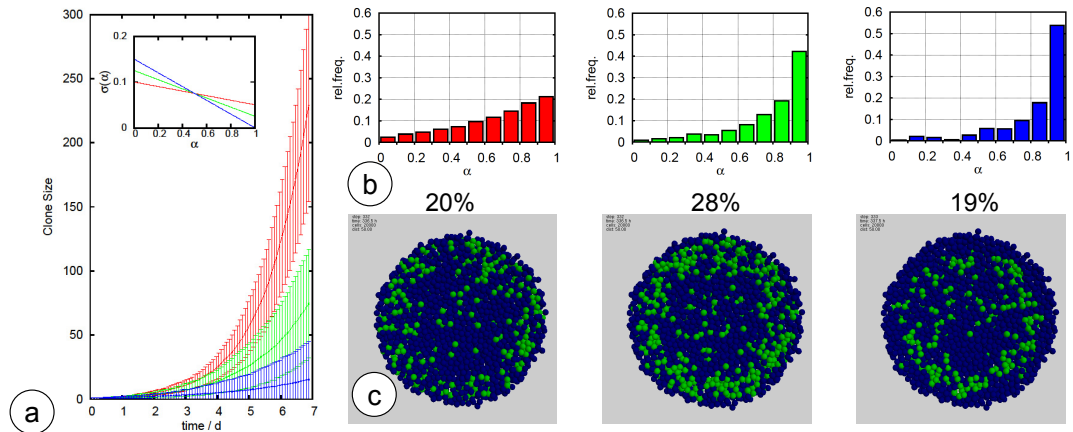


Figure 5.6: Simulated properties of single cell-derived MSC clones. a) Growth behavior of single cell derived clones initiated with cells of age $\sigma(\alpha = 0) = 0.1$ (young, red), 0.125 (intermediate, green), 0.15 (old, blue). b) Histograms of the differentiation parameter α in the populations resulting from the growth process. Cells are considered to be spontaneous differentiated with $\alpha > \alpha_d = 0.85$. Colors are the same as for growth curves. c) Simulated induced chondrogenesis in pellet culture. Pellets are generated from the populations above. Green cells are functionally differentiated and their total fraction is given by the numbers. After 14 days of culture the youngest (left) and oldest pellet (right) contain less functional differentiated cells (number on top) than the pellet of intermediate age.

the age $\sigma(\alpha = 0)$ is smaller than $\sigma_E = 0.15$. Contact inhibition was neglected in the niche. The simulations started with a small number (4 cells) of initial stem cells of age σ_0 (*in vivo*) and generated an aging niche population. After this population reached a sufficient age $\sigma(\alpha = 0) = 0.07$ four equidistant time points defined four age groups. The obtained differentiation structures were used to simulate the CFU-F capacity of MSC ‘isolated’ at these time points. Thereby, plating a cell was simulated by changing its mean noise amplitude σ_E at conserved stem cell noise amplitude $\sigma(\alpha = 0)$ to its value at high oxygen conditions (20% pO_2 , Fig. 5.7a). In order to calculate the CFU-F capacity of the age groups 100 cells for each group were plated and 5 day of colony growth was simulated. Afterwards the number of colonies that expanded to more than 20 cells were counted. As shown in Fig. 5.7b the simulated CFU-F capacity was found to decrease with age.

Experimental validation: CFU-F assays of aged rat MSC. *In vivo* aging of MSC was demonstrated using MSCs of 3, 7, 12 and 56 weeks old rats (Fig. 5.7c). MSC isolated from 3 weeks old rats showed a significant higher CFU-F capacity than MSC of all the other groups ($p < 0.05$). Moreover, MSC isolated from 12 weeks old rats showed a significant higher CFU-F capacity than MSC from 56 weeks old rat ($p < 0.05$). Together these results demonstrated a continuously decreasing CFU-F capacity of rat MSC with age, in qualitative agreement with the simulation results. This tendency represents a qualitative result. Quantitative predictions of the clone size distribution in a CFU-F assay would require detailed knowledge about the *in vivo* age distribution of MSC. Experimental results by D’Ippolito *et al.* [170] and Wagner *et al.* [176] suggest that *in vivo* MSC can differ by more than 20 cell doublings.

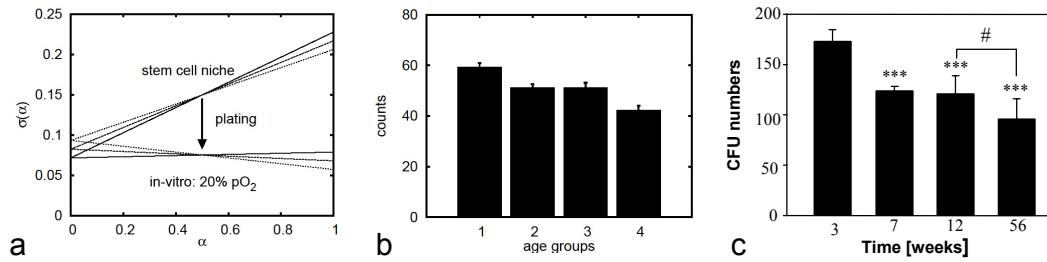


Figure 5.7: Simulating and monitoring *in vivo* aging. a) Noise amplitude profiles in the stem cell niche at different times. Due to the aging concept these profiles change over time. Accordingly, the noise amplitude profiles of the populations plated *in vitro* differ. b) Simulated CFU units. A continuous decrease of the CFU potential was observed. c) Experimental result regarding the CFU-F capacity of MSC of 3, 7, 12 and 56 weeks old rats.

5.5 Discussion

In a combined experimental and theoretical study it was demonstrated that clonal heterogeneity of MSC can be explained by a stem cell aging concept that associates aging with (de)stabilizing regulatory states. Extending the model introduced in Chapter 3 it was assumed that each cell division induces changes of the environment-dependent noise profile of a cell. Due to these changes unspecific pre-differentiated cells become more frequent over time. This is in agreement with experimental observations on stem cell aging [176,184]. The simulations suggest that also the differences in the chondrogenic potential of MSC clones are a consequence of such aging dynamics. The presented aging concept is general in the sense that *in vitro* and *in vivo* aging are assumed to base on the same principles independent of species. This is supported by recent experimental findings that *in vivo* aging and replicative senescence *in vitro* have related effects on stem cells [178].

In the model the cellular environment still determines the mean noise amplitude. Thus, the environment can either conserve or destabilize stem cell and progenitor states. Affecting the distribution of the differentiation states it impacts the proliferation activity of the cells and, thus, also aging. Actually, it may also affect aging directly by controlling the aging rate r_D . Here a constant aging rate independent of the environment and species was assumed. One crucial component of the environment is oxygen. In terms of the model low oxygen tension corresponds to a high mean noise amplitude. Increasing oxygen tension decreases this amplitude and thus, can act as differentiation signal. Accordingly, aged MSC are much more prone to pre-differentiation at high oxygen tension in agreement with experimental findings in the Chapter 3. It can be expected that effects of high glucose levels on MSC senescence [165] can be explained in a comparable way. MSC organization is also affected by cellular growth factors [185]. In fast and slow growing clones the segregation of such factors may differ. This study presented experimental evidence that clonal heterogeneity of a MSC population *in vitro* is not associated with a significant benefit regarding growth and chondrogenic differentiation. There is increasing evidence that stem cells adapt to changing environment utilizing various epigenetic mechanisms including chromatin remodeling [31,186,187]. In particular, DNA-replication represents a window of opportunity for changes in epigenetic states [36]. Histone modifications have been associated with MSC self-renewal [188]. Changes in such modifications have been observed in aging MSC [189]. Such changes may reflect the adaptive process of MSC to regenerative demands. Accordingly it

was hypothesized that each division event forces MSC to actively destabilize stem cell states. The original stem cell potential is lost in adaptation to proliferative conditions. Metabolic activity, in particular during DNA replication, causes DNA damages, e.g. by ROS and other free radicals. It is known, that DNA-damages and concomitant repair processes can induce genome-wide epigenetic changes [190]. Thus, adaptation to regenerative demands and accumulation of damages appear to be closely linked. Consistently, ROS and other free radical emissions by cells and tissue were demonstrated to be indicators of aging *in vivo* and *in vitro* [191]. Moreover, ROS was shown to be involved in signaling and stimulating differentiation processes in MSC [192,193]. In agreement with these findings anti-oxidative defense enzymes delay MSC aging. A prolonged lifespan and an enhanced growth rate were observed in human MSC cultures supplemented with antioxidants [194]. It can be expected that understanding the molecular mechanisms linking stress response and epigenetic changes will pave the way to anti-aging and rejuvenation strategies utilizing epigenetic reprogramming of adult stem cells [31]. The results presented in this study give a panel of experimentally testable predictions regarding MSC organization *in vitro* and *in vivo*. Regarding *in vitro* culture, the model predicts that spontaneous pre-differentiation of aged MSC *in vitro* will occur faster with each generation. However, a defined number of initial cell divisions is required to enable efficient functional differentiation. In the model this number depends on the mean noise amplitude which is determined by the cellular environment. Thus, the model predicts that for each isolation protocol and each culture condition an optimal size of an MSC population exists to which it should be expanded before using it in differentiation assays. The results by Sekiya *et al.* [195] on chondrogenic differentiation support this prediction. Regarding *in vivo* aging, the model predicts that the population structure in the niche environment changes. In particular, the number of cells sorted by so-called stem cell markers will decrease while cells sorted by markers for progenitors will increase. It was demonstrated that the number of functional stem cells in the rat bone marrow decreases with age. These findings agree with results on human MSC by D'Ippolito *et al.* [170]. Additional to changes of the population structure the model predicts an increased turnover in the aged bone marrow. Whether this will result in an increased release of MSC and what the consequences of such a release for the whole body would be remains speculative. The results emphasize that in order to understand MSC organization *in vivo* it will be of exceptional interest to study changes of the MSC turnover in the bone marrow with age and in disease.

6

Intracellular Processes: Wnt Signaling and Glutamine Synthetase Gen Expression in Hepatocytes

6.1 Introduction

In the last chapters a phenomenological model for differentiation, growth processes and aging of mesenchymal stem cells was introduced. The degree of cellular differentiation was summarized by only one cellular state variable α , while another one, β , specified the lineage. From a microscopic point of view each combination (α, β) may subsume a set of expression patterns. The large number of functional and regulatory molecules contributing to the cellular state of differentiation and thus the unfeasability motivated such a phenomenological model. On the other hand, development and function of a complex organism require precise control of all molecules contributing to cellular regulation in time and space. Fundamental are cellular communication and therefore the methods of transmitting information. Among these methods are diffusing chemical signals like morphogens and contact-dependent signaling via cell-cell contacts. For example, the wingless-family genes are widespread among species and the function of their protein is crucial in development and homeostasis of many tissues [61, 196–202]. Among the three wnt pathways the canonical wnt/ β -catenin pathway represents the most studied one, and it is directly involved in the zonation of lobuli in the liver and in particular in regulation of Glutamine Synthetase (GS) activity [203]. In this chapter regulation of GS activity based on wnt signaling serves as an example for modeling cellular regulation on a molecular level.

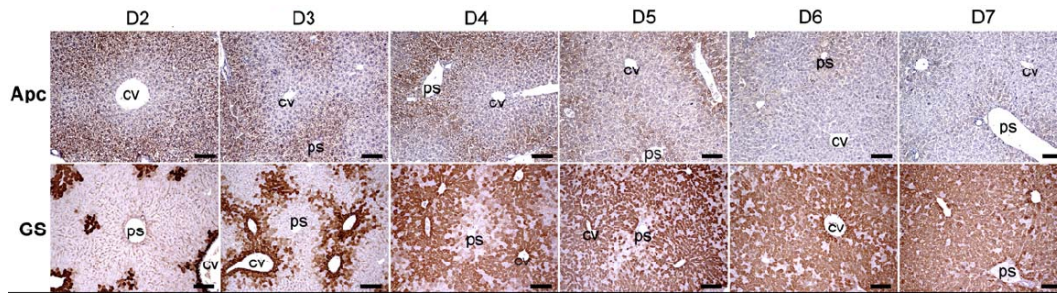


Figure 6.1: APC and GS activity after tamoxifen induced APC knockout After APC knockout the pericentral phenotype spreads over the whole lobule. After complete loss of APC GS activity can be observed in close proximity to the portal triad.

6.2 Background and Experiments

Glutamine Synthetase is found in the liver, one of the key organs in higher metazoan, and is involved as one key enzyme in nitrogen metabolism. Within the liver it is exclusively expressed in the pericentral hepatocytes complementary to the region of ureogenesis. This geometry is essential for liver function, because it enables GS to guarantee homeostasis of blood levels of ammonium ions and glutamine [203]. Recent results on liver zonation have shown that the wnt-pathway is the key to understanding the zonation. These results assigned adenomatous polyposis coli (APC), a component of the β -catenin-degradation complex, the role of “zonation keeper” [204, 205]. In these experiments, APC knockout is followed by establishment of a pericentral phenotype in the whole lobule. GS expression starts spreading after day 3 from the proximal pericentral hepatocytes and covers the whole lobule after day 5 (Fig. 6.1, [204]). Similar results are observed after an induced overall expression of β -catenin. Finally, overall expression of Dkk leads to almost complete loss of the pericentral phenotype and generation of the periportal one in the whole lobule. Together these results strongly indicate the role of the canonical wnt-pathway for regulation of GS. Although little is known about how APC is regulated, it is questionable to consider APC alone as the zonation keeper, because complete knock-out of APC is equivalent to knock-out the whole destruction complex.

After identification of the signaling pathway, a regeneration experiment gives some hint on the mechanisms of signaling. CCl_4 intoxication affects mainly the pericentral region of the liver [206]. Four days after CCl_4 intoxication the pericentral hepatocytes die and, thus, GS activity is lost. After another 4 days GS activity is regenerated in the lobule (Fig. 6.2). Regeneration of GS activity starts after the first contact of hepatocytes to the endothelial cells of the vein is formed, although not necessarily in the hepatocytes establishing this contact. This may be a sign of contact-dependent signaling and would be in accordance with wnt-signaling (see below). In the course of regeneration an overshoot of GS activity is observed but returns soon to the original level [207].

In-vitro GS expression can be induced *de novo* in GS-negative periportal hepatocytes by co-culture with RL-ET 14 cell, a hepatic epithelial cell line. In direct contact and close vicinity with RL-ET 14 cells GS-negative hepatocytes start GS expression [208]. In one set-up contact was inhibited using a plastic ring, and only after removal of the ring GS expression was induced in a layer of approx. 15 cells. From day 4 to day 5 after removal GS activity was still increasing in the cultures. In presence of Dkk no *de novo* expression was observed, thus confirming the key role of wnt in this process [209]. Indication of a

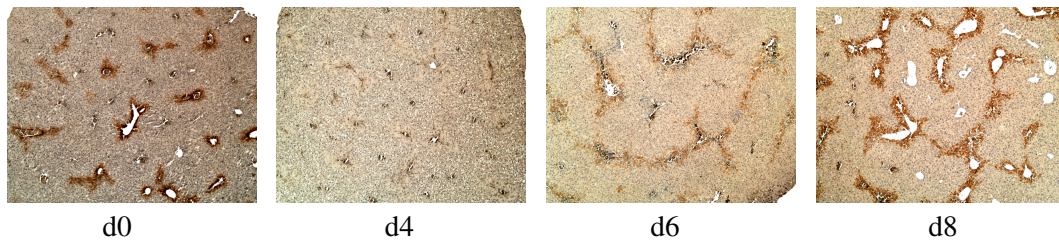


Figure 6.2: GS regeneration after CCl_4 intoxication. At day 0 the original expression pattern is seen and CCl_4 is injected for the first time. After day 4 and three CCl_4 injections GS activity is fully destroyed. At day 6 GS activity is slightly regenerated and after day 8 regeneration has completed.

contribution of diffusive wnt was shown by treatment of hepatocyte with preconditioned medium from RL-ET 14 cells, which resulted in increased GS expression, although the level did not reach the ones found in co-cultures [208].

Wnt-pathway Wnt genes encode a class of roughly 20 small proteins, which are involved in virtually every aspect of embryonic development [196,197]. The central component of the wnt-pathway is β -catenin representing the trigger of transcription. A schematic sketch of the canonical pathway is shown in Fig. 6.4.

In absence of wnt β -catenin is phosphorylated by the destruction complex, precisely, by Casein Kinase 1 (Ck1) and Glycogen Syntase Kinase 3 (Gsk3). Both kinases compose the degradation complex together with the scaffold protein Axin and adenomatous polyposis coli (APC). Phosphorylated β -catenin is ubiquitinated and finally degraded by the proteasome [196,197]. This results in a high turnover of β -catenin and a average half-life time of only 30 min [199].

If wnt signaling is present, the surface receptors Frizzled (Fz) and its co-receptor LDL related protein 5 or 6 (Lrp5/6) mediate it to the cytoplasm. The wnt-induced Fz-Lrp5/6 complex formation promotes recruitment of Axin and Gsk3 from the cytosol and initial phosphorylation of Lrp5/6 by Gsk3. Phosphorylated Lrp5/6 provides a docking site for additional Axin-Gsk3 complexes, which enables further phosphorylation [210]. Recruitment of these essential parts of the degradation complex inhibits β -catenin-degradation and stabilizes

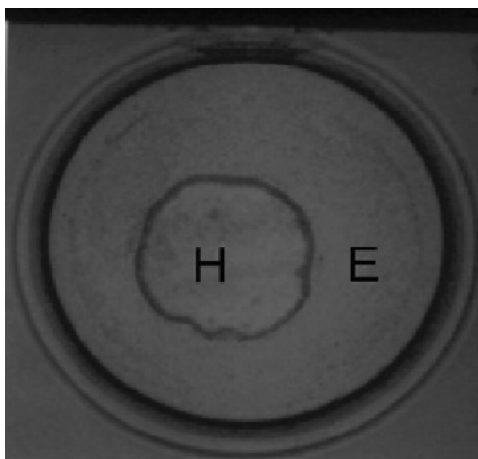


Figure 6.3: GS *de novo* expression in rat hepatocytes in co-culture with RL-ET 14 cells. Hepatocytes (H) are found in inside of the ring co-culture with RL-ET 14 cells (E). Three days after removing the plastic separation ring GS is detected in a small layer of hepatocytes near the interface with RL-ET 14 cells.

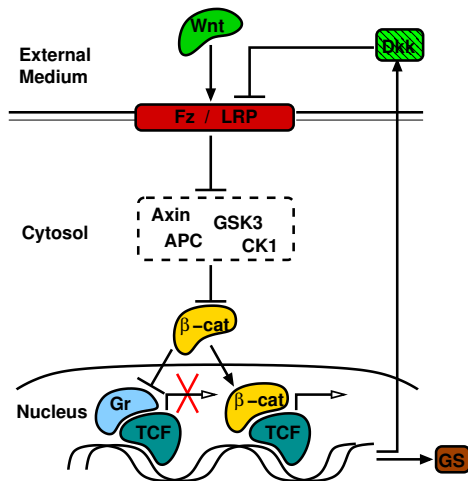


Figure 6.4: Simplified scheme of wnt-pathway and its feedback loop as used in the simulations. Binding of wnt to Fz and Lrp5/6, inhibits β -catenin-destruction by recruiting the destruction complex constituents Axin and Gsk3. The β -catenin-level is stabilized, and it translocates into the nucleus, replaces Groucho(Gr) and thereby transforms TCF from the repressor Groucho/TCF into the transcription factor β -catenin/TCF. Here the targets of interest are GS and Dkk. The latter competes with wnt for the receptors and introduces the negative feedback-loop.

cytosolic β -catenin level [199]. Nuclear β -catenin-buffers ensure a switch-like behavior of the T cell factor (TCF): at low β -catenin-concentrations TCF/Groucho acts as a silencer, but above a certain threshold β -catenin/TCF is formed and changes TCF into a transcription factor [199]. Stabilized cytosolic β -catenin provides sufficient nuclear β -catenin to initiate transcription of wnt/ β -catenin targets. One of the many targets of β -catenin/TCF is the wnt-antagonist Dickkopf-1 (Dkk). Dkk introduces a negative feedback into the wnt-pathway by docking to the same surface receptors as wnt [211]. After release of Dkk into the extracellular medium it binds to Lrp5/6 and inhibits the recruitment of Gsk3 [212].

Transport of signaling molecules: It has been shown, that wnt function and transport depend on lipid modifications at two sites [213]. This results in a strong affinity to lipids, in particular to the cell membrane. However, wnt is found to some unquantified extent in the supernatant [209]. For diffusion in aqueous media like the supernatant attachment to other molecules like heparan sulfate proteoglycans (HSPGs) or integration into vesicles is necessary [214]. For free diffusion in the medium this results in a much smaller diffusion coefficient due to the size of the transporter complex. But transport mechanisms of wnt are still subject of heavy debate. Evidence for other mechanisms of transport like membrane bound transport or transcytosis, i.e. repeated rounds of internalization and externalization, has been reported [215]. It may be viewed as a support for the hypothesis of transcytosis, that wnt was found to be associated with argosomes and their speed of transport to be consistent with the speed of motor proteins and the rate of wingless spreading [215].

The wnt-antagonist Dkk is soluble and can diffuse more rapidly than wnt [216]. Nevertheless, because all receptors are internalized and externalized, Dkk may spread by transcytosis, too.

6.3 PDE System for Activator and Inhibitor

Recently Sick *et al.* [61] have studied the wnt pathway as a possible control mechanism in the distribution of rat hair follicle. They applied modified Gierer-Meinhardt equations for wnt as the activator and Dkk as the inhibitor. Here the following very similar system is used, which differs from the system of equations used by Sick *et al.* [61] by the advection term that mimics for the *in vivo* case the blood flow transported from the periportal field to the central vein in the liver by the additional advection term $v\nabla[\text{wnt}/\text{dkk}]$:

$$\begin{aligned}
\frac{\partial [\text{wnt}]}{\partial t} &= D_{\text{wnt}} \Delta [\text{wnt}] + v_{\text{wnt}} \nabla [\text{wnt}] + \rho_{\text{wnt}} F([\text{wnt}], [\text{dkk}]) - \mu_{\text{wnt}} [\text{wnt}] \\
\frac{\partial [\text{dkk}]}{\partial t} &= D_{\text{dkk}} \Delta [\text{dkk}] + v_{\text{dkk}} \nabla [\text{dkk}] + \rho_{\text{dkk}} F([\text{wnt}], [\text{dkk}]) - \mu_{\text{dkk}} [\text{dkk}] \quad (6.1) \\
F([\text{wnt}], [\text{dkk}]) &= \frac{[\text{wnt}]^2}{(K + [\text{dkk}](1 + \kappa [\text{wnt}]^2))}
\end{aligned}$$

$[\text{wnt}]$ and $[\text{dkk}]$ are the time and space-dependent concentrations, D_{wnt} and D_{dkk} the diffusion coefficients, ρ_{wnt} and ρ_{dkk} the production constants of wnt and dkk, respectively. The Hill function F guarantees production saturation for both species and v_i is the velocity of advection of species $i = \text{wnt}, \text{dkk}$. Both species are assumed to diffuse, but the formation of the observed pattern required a much faster diffusing inhibitor $D_{\text{dkk}} \gg D_{\text{wnt}}$ in agreement with slow diffusion caused by palmitoylation of the wnt molecule. The coupling of both equations is found in the production term where both concentrations enter into the Hill function.

Here this model system of activator-inhibitor-interplay was used as a first approach to modeling GS expression in the liver. Motivated by the circular arrangement of the co-culture experiment and the geometry of a liver lobule, a 1D system was chosen for simplicity. RL-ET 14 cells and endothelial cells of the central vein were assumed to supply a constant activator signal representing wnt. This source of wnt was set at $x = 0$. A solution for the parameter set given by Sick *et al.* [61] was calculated using `Mathematica`. The model parameters are all dimensionless, but related to experimentally measured quantities by length and time scales. All parameters are given explicitly in Table 6.1.

Initial conditions assume vanishing concentrations except for the constant wnt-signal at $x = 0$. Neumann boundary condition incorporate vanishing spatial derivatives at the boundaries and thus reflect a closed domain. Three scenarios are tested:

1. For *in vitro* culture the advection term vanishes, $v_i = 0$ for wnt and Dkk. Dkk is transported by diffusion, while the mechanism for wnt is unspecified (diffusion of transporter complexes, transcytosis, membrane bound).
2. In the liver there is a constant flow of blood causing an advection term with $v_i > 0$ for Dkk and wnt, if both are transported in the extracellular medium by diffusion.
3. If wnt is not found freely in the medium and does not diffuse, but is transported by transcytosis or membrane bound, advection affects only Dkk transport: $v_{\text{dkk}} > 0$.

The results of the system for the parameter values in Table 6.1 are shown in Fig. 6.5. The concentrations approach an equilibrium. Assuming an activator threshold of 0.1 for the GS production and setting the length scale to 2-3 cell diameter, the PDE approach yields for the case without advection ($v = 0$) a layer of 10-12 cells. If advection affects both species, this layer reduces to 2-3 cells and the number of activated cell producing both molecules strongly reduced leading to a much smaller total Dkk content. If only Dkk is affected by

D_{wnt}	D_{dkk}	ρ_{wnt}	ρ_{dkk}	μ_{wnt}	μ_{dkk}	K	κ	v
0.005	0.2	0.005	0.02	0.005	0.015	0.1	0.01	1

Table 6.1: Dimensionless parameter for the first test of the simple activator-inhibitor-system for the zonation of the liver as given in [61].

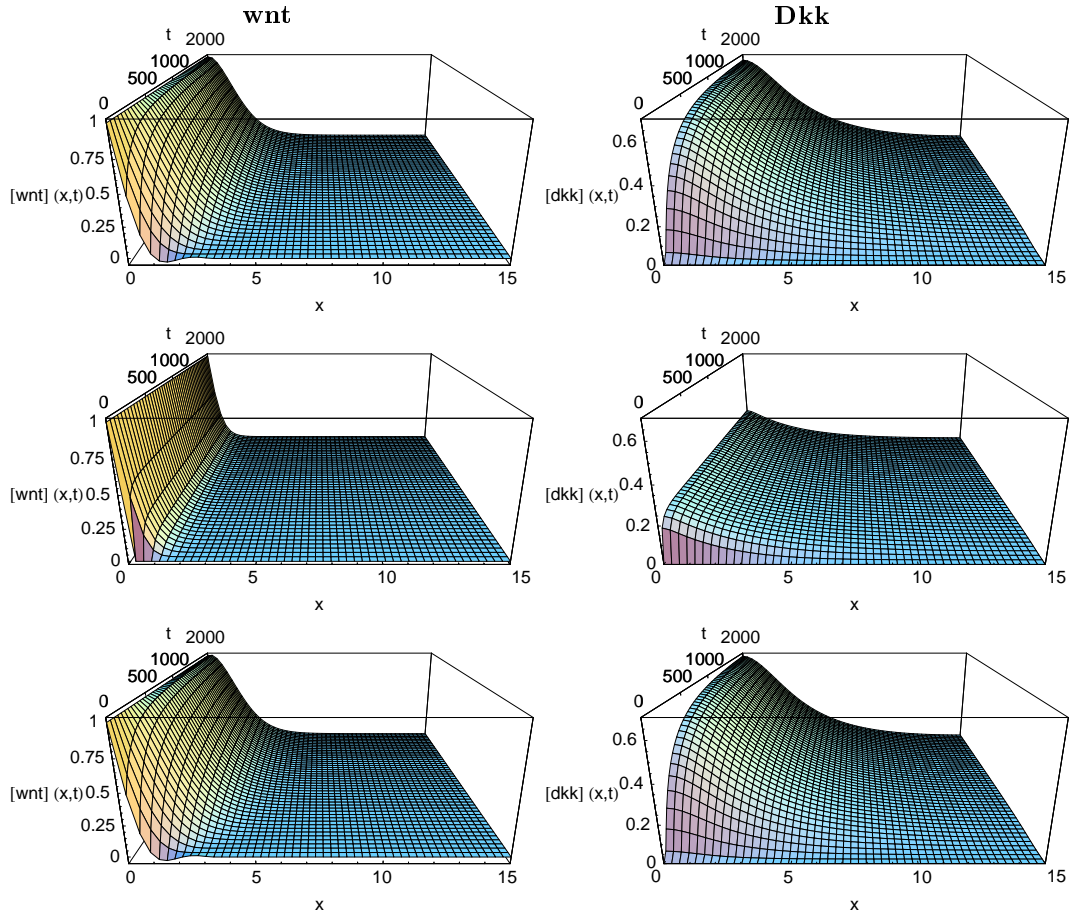


Figure 6.5: Solutions of the simple 1D activator-inhibitor PDE approach (Left: wnt, Right: dkk). A constant wnt signal is found at $x = 0$. The x -axis represents the portal-central axis and activator threshold for GS is assumed to be 0.1. Assuming transport conditions according to the scenarios 1-3 a layer of 1. ~ 15 (top), 2. ~ 3 (middle), and 3. (unchanged to 1) ~ 15 GS-positive cells is found.

diffusion, the layer is unchanged compared to the case without advection, because even a small concentration of the inhibitor Dkk (≈ 0.1) reduces the production term by 90%, even at maximal activator concentration. This setting of parameters results in a fast approached equilibrium with only a small production term for both molecules close to the source of the activator, which is responsible for the equilibrium.

Discussion of PDE approach: As a first interpretation, the results of this simple approach would suggest diffusion based wnt transport, because the difference in the extent of GS-activated layer between static situation and the one affecting both species by advection is of the same order as between *in-vivo* and co-culture.

But despite a simple explanation of control of GS expression, some effects of possible impact are neglected:

Activation as assumed in the PDE system includes positive autoregulation of wnt. Although several feedback loops for autoregulation of the wnt-pathway exist like the regulation of Frizzled, Lrp5/6, HSPG, Axin2, TCF/Lef and Dkk (e.g. [196]), a direct transcriptional autofeedback loop of wnt has only been reported for a pluripotent mouse embryonal carcinoma stem cell line (P19CL6) by Deb *et al.* [217]. Considering the complexity of wnt-regulation including e.g. cross-talk with other pathways like MAPK/Erk [218,219] etc., the generalization from a cancer cell line to all mammalian cell, in particular hepatocytes, is highly speculative.

Delay in release of a target caused by transcription, translation and externalization is completely neglected as production of both, activator wnt and inhibitor Dkk, starts immediately. According to González-Sancho *et al.* [211] β -catenin is found in HeLa cells after approx. 4h and Dkk-1 RNA after approx. 12h of wnt treatment. HeLa cells are a cell line, which proliferates abnormally rapidly and impact of immortalization on the cellular regulation in general and β -catenin in particular cannot be excluded, which does not allow generalization.

Geometry in a co-culture and in the liver includes a different radial dilution of diffusing substances. This effect would at least introduce a factor of order $1/x$ which is neglected, too.

Conclusion: The 1D activator-inhibitor PDE approach extremely simplifies the system. However, it provides a possible explanation for the different ranges of GS expression in a liver lobule and *in vitro* culture. It suggests, that either wnt transport is affected by portal-central flux to similar extent as Dkk or a wnt antagonist is found in the periportal compartment like reported for hrs/serum [218].

The shortcomings of the simple 1D PDE approach are circumvented by integrating a model for the wnt pathway into the individual cell-based model. A detailed model for transport mechanism similar to Bollenbach *et al.* [220] will be included as well as a model of the wnt pathway in the cell. Application of the model does not include cellular motion, but an integration into the full 3D model of a liver lobule by Stefan Hoehme [221] is projected.

6.4 Individual Cell-Based Model for wnt Signaling

Reduction to Key Species and Processes

In order to keep the simulation strategy for the observed GS expression *in vitro* as clear and simple as possible, reduction to key components is essential. Starting with the wnt-signal and following the pathway downstream, as depicted in Fig. 6.4, one arrives at the following conclusions for the agents of the pathway:

Wnt is the morphogen suggested to introduce GS expression.

Receptors transmit the exterior wnt signal to the interior of the cell. Because surface expression of both receptors is necessary for activation of the pathway and wnt and Dkk compete for the activating receptor [196], it is not distinguished between both types of receptors. Dsh is only forwarding the signal downstream, and is therefore not included into the model.

Destruction complex initiates β -catenin degradation by marking it for ubiquitination. It is inhibited by wnt-bound receptors. Because the regulation of its constituents is

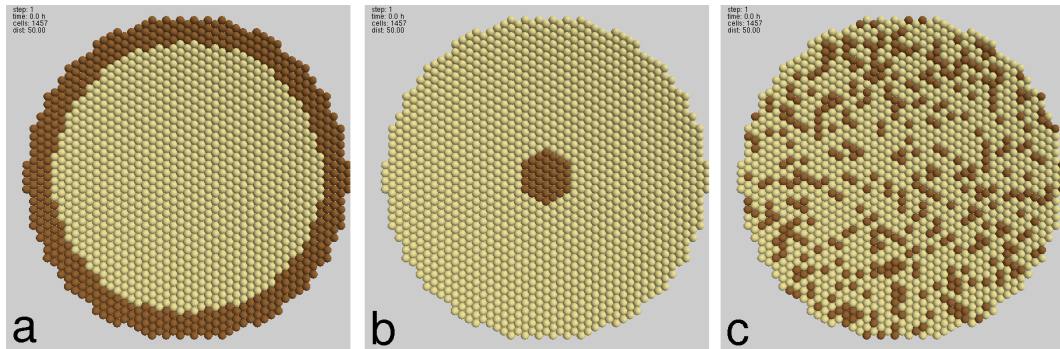


Figure 6.6: Geometries used in the Simulations. a) Concentric co-culture as used in [208] and b) simple geometry mimicking a liver lobule after CCl_4 intoxication, composed of a small circular area of wnt-positive cells in the center (endothelial cells of the central vein) surrounded by GS-negative hepatocytes. c) Co-culture experiments of a random mixture of RL-ET 14 cells and hepatocytes.

largely unknown it enters via a Michaelis-Menten approach of competitive enzyme inhibition.

β -catenin concentration is controlled by the activity of the degradation complex. Above a threshold it initiates transcription of the wnt/ β -catenin targets.

Dkk is a β -catenin/TCF target and a wnt antagonist. By competing for the same receptors it introduces a negative feedback into the network studied here.

GS a β -catenin/TCF target and the species studied in the co-culture experiments.

Note, that for a better overview the parameters are summarized in A.4.4.

Simulation Scenarios

The simulation focuses on spreading and processing of the wnt-signal. At this stage it does not include growth and motion as presented in the previous chapters. Thus cell positions were kept fixed throughout the simulation and initialized in various geometries, two of them modeling co-culture experiments and another one as a simple model of a liver lobule (Fig. 6.6):

1. Modeling co-culture geometry 1: In one co-culture experiment, a plastic ring initially separating RL-ET 14 cells and hepatocytes is removed and contact between the two cell types is established. This situation of RL-ET 14 cells enveloping GS-negative hepatocytes is used as initial configuration.
2. Modeling the hexagonal liver lobule after CCl_4 intoxication: a small circular area of wnt-positive endothelial cells mimicking the central vein is surrounded by GS negative hepatocytes.
3. Modeling co-culture geometry 2: random positions of RL-ET 14 cells in various densities.

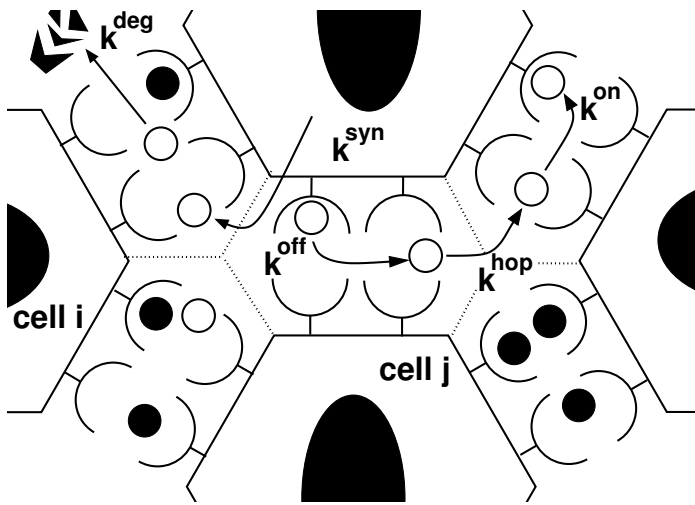


Figure 6.7: Lattice of the intercellular spaces and morphogen related processes. The dense sphere packing in two dimensions results in a honeycomb lattice of contacts. Both species, wnt and Dkk, are restricted to the lattice and the medium. In general all processes happen with different rates for wnt and Dkk. They are released into the contacts with k^{syn} . Both molecules hop from contact to contact with k^{hop} . In a contact they bind to free receptors on the surfaces of both cells and dissociate with k^{on} and k^{off} , respectively. If not bound both molecules are degraded with k^{deg} .

Geometry

The geometry of the model, i.e. cells, contacts and inter-cellular spaces, is defined by the included processes. Transcription/translation and β -catenin regulation happen in the interior of cells and are therefore spatially separated and associated with each cells interior. Receptor dynamics and membrane associated transport takes place in the vicinity of the membrane. A discretization of the membrane is given by the cell-cell and cell-medium contact areas. Contacts between two cells i and j can be assigned unique labels $\langle i, j \rangle$ similar to Bollenbach *et al.* [220]. In a dense sphere packing of a monolayer this results in a honeycomb lattice, where every cell inside the colony has six contacts to other cells (see Fig. 6.7). In a 2D culture each cell has access to the medium. This is accounted by an additional seventh contact to the medium. In the medium, which is discretized by a rectangular lattice, a fraction of signaling molecules can freely diffuse, and enter the matching cell-cell contacts from the medium and vice versa. The rectangular medium lattice in which diffusion is modeled is chosen so that an equal number of contacts is found in each medium lattice site if each contact is mapped to the lattices site its center is located in. Hence the ratio of the lattice constants is $\sqrt{3}/2$. If a cell-cell contact is empty due to boundary effects it is regarded as an extra contact to the medium and identified with the corresponding medium lattice site, too.

wnt turnover

In summary, the wnt dynamics included by the proposed model consists of production and release, membrane bound transport and free diffusion, receptor binding and unbinding and, finally, the degradation of unbound molecules (see Fig. 6.7). In the following these processes are explained in detail.

Production of wnt happens without positive auto-feedback only in RL-ET 14 cells or the endothelial cells of the central vein, since a direct transcriptional autofeedback loop for wnt has only been reported for a carcinoma stem cell line [217]. Restriction of wnt-production to these cells is also motivated by the observation that GS-positive cells do not induce GS expression in other hepatocytes. The production rate $k_{\text{wnt}}^{\text{syn}}$ is assumed to be constant and equal for all wnt-positive cells. wnt is released into extracellular space, this means transported equally to all contacts of the respective wnt-producing cell. Each cell i has seven contacts (six to its neighbor cells, one to the medium that covers the cell population) and therefore releases on average

$$\frac{d}{dt} [\text{wnt}]_{\text{syn}} = \frac{1}{7} k_{\text{wnt}}^{\text{syn}} \quad (6.2)$$

into each of the surrounding contact spaces $\langle i, j \rangle$ to other cells or the medium.

Transport of wnt: Similar to the model presented by Bollenbach *et al.* [220] each cell-cell contact between two cells in the interior of the culture has boundaries with contact areas to the substrate, other cell-cell contacts and the medium. From a cell-cell contact the wnt molecules can therefore transfer into the medium and neighboring contact spaces, but not into the solid substrate. Transfer into another cell-cell contact occurs with hopping rate $k_{\text{wnt}}^{\text{hop}}$ and equally into all neighboring contacts. Thus, the molecules are assumed to move independently. The same accounts for molecules entering cell-cell contacts from the medium with a rate k^{in} or leaving the intercellular space into the medium with k^{out} . Depending on the number of molecules, these processes happen stochastically with equal rates for small molecule numbers or deterministically as the average for large numbers. The contribution to the change of $[\text{wnt}](\langle i, j \rangle)$ in contact $\langle i, j \rangle$ by transport is therefore on average given by:

$$\begin{aligned} \frac{d}{dt} [\text{wnt}]_{\text{hop}}(\langle i, j \rangle) = & k_{\text{wnt}}^{\text{hop}} \sum_{nn(\langle i, j \rangle)} [\text{wnt}](\langle k, l \rangle) - 4 k_{\text{wnt}}^{\text{hop}} [\text{wnt}](\langle i, j \rangle) \\ & + k_{\text{wnt}}^{\text{in}} [\text{wnt}]_{\text{lat}} - k_{\text{wnt}}^{\text{out}} [\text{wnt}](\langle i, j \rangle), \end{aligned} \quad (6.3)$$

where the exchange with other cell-cell contacts and the medium are given in the first and second line, respectively. The sum runs over all cell-cell contacts $\langle k, l \rangle$ connected to contact $\langle i, j \rangle$ by a common edge and $[\text{wnt}]_{\text{lat}}$ the concentration in the medium lattice site the contact is situated in. Note, that this model of membrane bound diffusion of free wnt molecules is in principle applicable for modeling other transport mechanisms: Allowing the ligand-receptor complexes to translocate to neighboring contacts mimics 2D diffusion within the membrane, and transcytosis can be modeled making any contact accessible for the complexes, but no major differences are expected according to the results of Bollenbach *et al.* [220].

The contribution of hopping to a concentration change in a lattice site of the medium, that is in contact to the 2D culture, is calculated analogous.

$$\frac{d}{dt} [\text{wnt}]_{\text{lat}} = k_{\text{wnt}}^{\text{out}} \sum_{\langle i, j \rangle \in l} [\text{wnt}](\langle i, j \rangle) - n_c k_{\text{wnt}}^{\text{in}} [\text{wnt}]_{\text{lat}}(l), \quad (6.4)$$

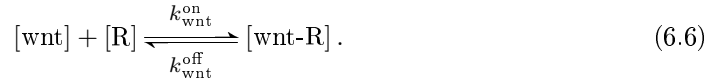
where the sum runs over the cell-cell contacts $\langle i, j \rangle$ within the considered medium lattice site l and n_c is their number, for this particular choice of lattice holds $n_c = 3/4$. The first and the second term represent the molecules leaving and entering cell-cell contacts, respectively.

Normal Diffusion of wnt is restricted to the medium. Within the medium concentrations are calculated solving the diffusion equation

$$\partial_t [\text{wnt}]_{\text{lat}}(r, t) = D_{\text{wnt}} \Delta [\text{wnt}]_{\text{lat}}(r, t), \quad (6.5)$$

with the diffusion coefficient of wnt D_{wnt} and its concentration $[\text{wnt}](r, t)$. The diffusion equation is solved on a rectangular lattice chosen as reasoned above. Due to the mentioned lipidmodification of wnt a small diffusion coefficient is assumed.

Binding/unbinding to receptors is a dynamic process transmitting the wnt signal into the cell and propagating it downstream [196]. A free wnt molecule in the intercellular is assumed to bind to a free accessible receptor with a rate $k_{\text{wnt}}^{\text{on}}$. Accessible receptors are those located on one of the surfaces confining the contact associated with the molecule's position. Wnt molecules bound in a contact in a wnt-receptor complex can dissociate with $k_{\text{wnt}}^{\text{off}}$ and a wnt molecule is released into the intercellular space of the contact leaving a free receptor.



For the reaction rate a simple mass action law with constant rates is assumed, so that the resulting difference of free wnt-molecules, free receptors and wnt-receptor complexes is:

$$\frac{d}{dt} [\text{wnt}]_r = -k_{\text{wnt}}^{\text{on}} [\text{wnt}] [\text{R}] + k_{\text{wnt}}^{\text{off}} [\text{wnt-R}], \quad (6.7)$$

where the subscript r denotes the contribution of the binding-unbinding process to the total change of wnt in the considered contact. The ratio of $k_{\text{wnt}}^{\text{on}}$ and $k_{\text{wnt}}^{\text{off}}$ defines the ratio of bound/free receptors in equilibrium and in absence of wnt.

Degradation of wnt is assumed to affect only free wnt molecules. These molecules are degraded at a constant rate $k_{\text{wnt}}^{\text{deg}}$ so that the number of degraded molecules in each contact and medium lattice site is given by:

$$\frac{d}{dt} [\text{wnt}]_{\text{deg}} = -k_{\text{wnt}}^{\text{deg}} [\text{wnt}]. \quad (6.8)$$

Summing up the contributions Summing up all contributions of the processes described above one arrives at the full equation for the wnt content in a contact.

$$\begin{aligned} \frac{d}{dt} [\text{wnt}] = & \frac{1}{7} k_{\text{wnt}}^{\text{syn}} \\ & + k_{\text{wnt}}^{\text{hop}} \sum_{nn\langle i,j \rangle} [\text{wnt}] (\langle k, l \rangle) - 4 k_{\text{wnt}}^{\text{hop}} [\text{wnt}]_{\text{lat}} + k_{\text{wnt}}^{\text{in}} [\text{wnt}]_{\text{lat}} - k_{\text{wnt}}^{\text{out}} [\text{wnt}] (\langle i, j \rangle) \\ & - k_{\text{wnt}}^{\text{on}} [\text{wnt}] [\text{R}] + k_{\text{wnt}}^{\text{off}} [\text{wnt-R}] \\ & - k_{\text{wnt}}^{\text{deg}} [\text{wnt}]. \end{aligned} \quad (6.9)$$

Dkk turnover

Dkk is the antagonist of wnt by competing for the same receptors. The same processes of production, transport, un/binding and degradation control Dkk-concentrations, but two main differences exist:

- Dkk is not palmitoylated
- Dkk is a target of the wnt/ β -catenin pathway.

The first difference results in different transport parameters D_{dkk} and $k_{\text{dkk}}^{\text{hop}}$ in the analog equations to Eqs. (6.5) and (6.3). The second difference manifests in Dkk transcription depending on the cytosolic β -catenin concentration and implications.

Dkk is only produced if the β -catenin concentration in a hepatocyte exceeds a certain threshold $[\beta\text{-catenin}]_c$, β -catenin enters into the nucleus and β -catenin/TCF promotes transcription of Dkk. Transcription, translation, intracellular transport and externalization are subsumed in a delay of Dkk production by the parameter Δt_{dkk} . Dkk is released with a production rate $k_{\text{dkk}}^{\text{syn}}$ into extracellular space only Δt_{dkk} after reaching the β -catenin-threshold of transcription $[\beta\text{-catenin}]_c$. Analogous, Dkk production is terminated only after Δt_{dkk} , if the cellular β -catenin-concentration has dropped below $[\beta\text{-catenin}]_c$.

Because the wnt sources, RL-ET 14 and hypothetically endothelial cells of the central vein, stably express wnt in the model, they are also assumed to be unaffected by the wnt signal and excluded from the Dkk-producing cells. For stability reasons, start and stop of transcription is assumed to be separated by a threshold of $\beta\text{-c} \pm 5\%$. Otherwise the fluctuations in the model would result in a permanently fluctuating rather than a stable GS activity.

Receptor competition

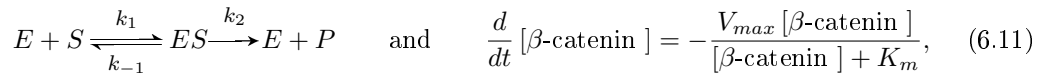
Both ligands bind to and unbind from the receptors by the simple reaction 6.6. In analogy to Eq. (6.7) the number of receptor molecules in each state is given by:

$$\begin{aligned} \frac{d}{dt} [\text{R}] &= -k_{\text{wnt}}^{\text{on}} [\text{wnt}] [\text{R}] - k_{\text{dkk}}^{\text{on}} [\text{dkk}] [\text{R}] + k_{\text{wnt}}^{\text{off}} [\text{wnt-R}] + k_{\text{dkk}}^{\text{off}} [\text{dkk-R}] \\ \frac{d}{dt} [\text{R-wnt}] &= k_{\text{wnt}}^{\text{on}} [\text{wnt}] [\text{R}] - k_{\text{wnt}}^{\text{off}} [\text{wnt-R}] \\ \frac{d}{dt} [\text{R-dkk}] &= k_{\text{dkk}}^{\text{on}} [\text{dkk}] [\text{R}] - k_{\text{dkk}}^{\text{off}} [\text{dkk-R}] \\ [\text{R}]_{\text{tot}} &= [\text{R}] + [\text{R-wnt}] + [\text{R-dkk}] \end{aligned} \quad (6.10)$$

$k^{\text{off}}/k^{\text{on}}$ are individual for each ligand and their ratios define the concentration for half-receptor-occupancy at vanishing concentration of the other ligand.

β -catenin turnover

In contrast to the other system components β -catenin does not leave the cells' interior. β -catenin is assumed to be produced in the cells at a constant rate k_{β}^{syn} in all hepatocytes. Degradation on the other hand is an enzyme reaction dependent on the amount of wnt-bound receptors [196]. For a constant destruction complex level in the cytosol it follows a Michaelis-Menten kinetics with β -catenin as the substrate S and the destruction complex as the the enzyme E :



where $K_m = (k_{-1} + k_2)/k_1$ is the Michaelis-Menten constant and $V_{\text{max}} = k_2 [E]_0$ the maximal reaction rate. The latter depends on the amount of available enzyme $[E]_0$. As reasoned above the amount of available enzyme depends on the number of wnt-bound receptors, which are recruiting the scaffold protein Axin and the kinase Gsk3. Hence one can apply Michaelis-Menten for competitive inhibition of enzymes.

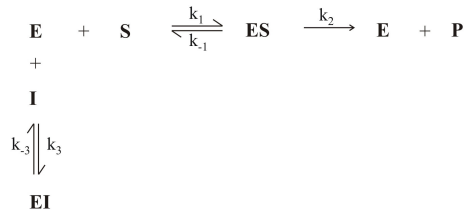


Figure 6.8: Competitive enzyme inhibition. Another binding partner competes with the substrate of the enzyme reaction for the enzyme and binds it reversibly. Inhibitor-enzyme complexes are inactive and do not degrade the inhibitor.

Competitive enzyme inhibition. is given if an inhibitor prevents the reaction by binding to the enzyme and blocking the active site, without undergoing a reaction. Obviously the recruitment of Axin and Gsk3 to the receptor-dimer acts in a similar way. It is not exactly the enzyme reaction with competitive inhibition as shown on the right, because of the many components of the destruction complex and restriction of this particular inhibitor to the 2D domain of the cell membrane. But it holds true, that the wnt-bound receptors act as an inhibitor competing for essential components of the degradation complex. This motivates applying the Michaelis-Menten analogue of competitive enzyme inhibition as derived under the steady-state assumption [222]:

$$\frac{d}{dt} [\beta\text{-catenin}] = - \frac{V_{max} [\beta\text{-catenin}]}{[\beta\text{-catenin}] + K_m (1 + [\text{wnt-R}] / k_{inh})}, \quad k_{inh} = \frac{k_{-3}}{k_3} \quad (6.12)$$

where the amount of wnt-bound receptors $[\text{wnt-R}]$ replaces the inhibitor concentration $[\text{I}]_0$ and enters directly into the differential equation for the β -catenin concentration. The reaction is determined by three further model parameter. $V_{max} = [\text{E}]_0 k_2$ is the maximum β -catenin degradation rate, $K_m = k_{-1} + k_2/k_1$ the Michaelis constant for the β -catenin-degradation representing the substrate concentration for half maximum rate and no inhibitor and, finally, the strength of inhibition given by the dissociation constant of the inhibitor k_{inh} .

GS

β -catenin-dependent transcription starts only if $[\beta\text{-catenin}] > [\beta\text{-catenin}]_c$, but analogous to Dkk GS production is delayed by Δt_{GS} . After the delay GS is assumed to be produced at a constant rate k_{GS}^{syn} and to accumulate only in the cytosol. Degradation of GS by the proteasome happens at a constant rate k_{GS}^{deg} and is assumed to follow the law of mass action.

Simulation Parameters

To best knowledge, no quantitative data on the detailed molecular concentrations of the species and related time constants is available in sufficient detail. Regarding time scales the only cornerstones are given by measurements of β -catenin-activity in HeLa cells after wnt3a treatment, where β -catenin is observed after 4h of treatment and has almost vanished after another 4h [211]. Qualitative measurements of GS activity in hepatocytes have been reported, in which GS is observed after 2-3 days in APC knockout mice (e.g. [204]), and after CCl₄ intoxication experiment in rats [209]. Considering the lack of quantitative knowledge on the parameters and their general scalability, the results from those non-human systems are used for first parameter estimates. The set of parameters presented summarizing in Table A.5 has been chosen to best knowledge on the basis of analogies after a thorough discussion with the experimental collaborators [209].

Because the wnt-pathway is expected to be very sensitive, the inhibitor dissociation constant k_{inh} in Eq. (6.12) that quantifies the inhibitory effect of wnt-bound receptors on

the destruction complex was set such that already a few receptor-bound wnt molecules have a notable effect. For the parameter set found in A.4.4 Eq. (6.12) gives a minimum number of 57 wnt-receptor complexes that is necessary for stabilizing β -catenin-concentration above the transcription threshold β - c_c . Otherwise the cytosolic concentration of β -catenin is below this threshold and β -catenin is not able to initiate transcription.

Although in biological systems the receptor density is regulated, for simplicity N_r is assumed to be constant and equal for each cell. For their stochastic initialization the number in individual contacts may vary slightly. In the line of a very sensitive wnt-pathway, also a much bigger total receptor number of $N_r = 700$ was chosen such that the equilibrium of free to occupied receptors in Eq. (6.10) favors wnt binding in vicinity of the switch.

6.5 Results

6.5.1 Simulated concentric co-culture

Wnt-producing RL-ET 14 cells envelop hepatocytes.

Reference simulation In the co-culture experiment using a concentric geometry the final GS expression pattern was used for fitting the parameter. A stable layer of $\approx 5 - 6$ GS expressing cells was achieved using the simulation parameter given in Table A.5 (see Fig. 6.10 a). The underlying dynamics is documented by the time series of all concentrations for every cell (see Fig. 6.9 for selected cells). Wnt spreads from the RL-ET 14 cells into the interior resulting in an equilibrated radial gradient as indicated by the dark red curve. With increasing wnt in the extra-cellular environment, the number of wnt-receptor complexes increases (yellow) and inhibits degradation of β -catenin (green). This results in an increasing β -catenin concentration in all cells. In the nine cells closest to the RL-ET 14/hepatocyte interface the internal β -catenin-concentration rises to values above the transcription threshold β - c indicated by the black line at 100 molecules. After the delay Δt_{dkk} Dkk (shown in blue) is released into the extracellular space and after Δt_{GS} GS (black) appears in the cell. With the increasing number of Dkk molecules competing for the receptors the number of wnt-receptor complexes reaches a maximum and decreases to its equilibrium occupation, while the number of Dkk-receptor complexes saturates. This effect causes also a decrease of the β -catenin-content and ceasing expression of the two targets in three of the nine cells in Fig. 6.9. The total GS activity in the colony can be quantified by counting the cells with a GS concentration above a certain threshold. Fig. 6.11 shows the time course with the GS activity overshoot predicted by the reference simulation (red). Interestingly, such an overshoot has precisely been observed in hepatocytes after a CCl_4 intoxication [209].

Parameter variations: Oscillations & Co. In order to permit experimental verification of the model the possible GS-pattern *in vitro* were predicted for several parameter variations including the initial arrangement of the cell types. Because the wnt-gradient in the colony is only determined by production and transportation, an increase of the size of the wnt-positive layer or wnt-production leads to a greater amount of wnt in the system and, thus, in a larger number of GS-positive hepatocytes and an extension of the layer (see Fig. 6.11, green). Increasing transport smoothes the wnt gradient in the colony and also extends the region of transcription if sufficient wnt is available.

The size of the layer can also be influenced by changing parameters of β -catenin-dynamics like the (un)binding rates of the ligands, shifting the equilibrium distributions of the two

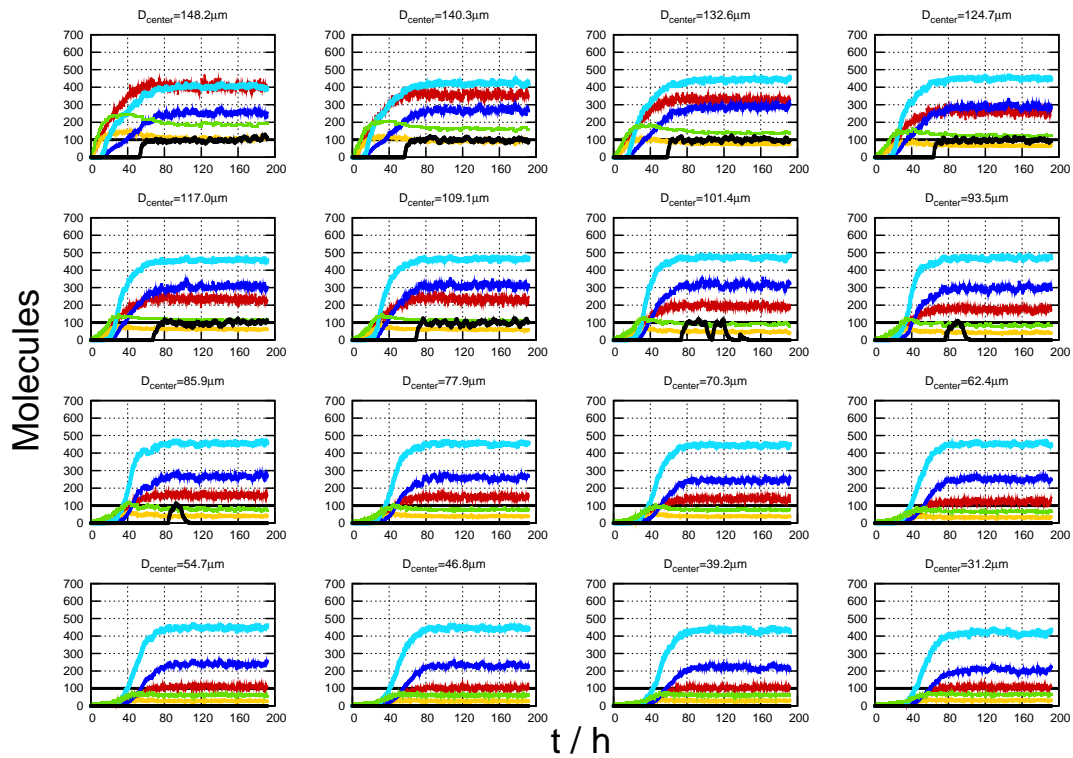


Figure 6.9: Details of the underlying dynamics of all pathway components for individual cells on a radial path. Each plot shows the pathway components for individual hepatocytes (center distance D_{center} given above the plot) with the colors encoding the following: dark red: extracellular wnt, yellow: wnt-receptor complexes, green: β -catenin, dark blue: extracellular Dkk, light blue: Dkk-receptor complexes, black: GS, black line indicates β -catenin-threshold. After spreading of wnt β -catenin concentrations rise, and Δt_{dkk} after the β -catenin-threshold is reached Dkk is released in the extracellular space followed by a decreasing number of β -catenin/receptor complexes. After equilibration GS expression is stable in a six cells thick layer, but four cells closer to the interior show only a short period of GS expression.

receptor complexes, the parameters of enzyme inhibition V_{max} , K_m and k_{inh} , or the transcription threshold $\beta-c_c$. For example, increasing the transcription threshold $\beta-c_c$ from 100 to 150 reduces the final layer of GS-positive cells by $\approx 40\%$ (see Fig. 6.10 b). A decrease in the receptor unbinding rate for wnt k_{wnt}^{off} results in a higher fraction of wnt molecules bound to receptors without changing the concentration of unbound wnt, and therefore higher sensitivity of the β -catenin regulation to wnt. Reducing k_{wnt}^{off} by 50% results in a layer of GS-positive cells of double extent (see Fig. 6.10 c). An increase of the number of wnt-producing cells in the outer rim causes an increase of the final number of GS positive cells as could be expected (Fig. 6.11).

Oscillations occur if β -catenin and Dkk dynamics, production, degradation are fast. If local Dkk levels rise fast enough, Dkk replaces wnt at a sufficient number of receptors to cause the β -catenin level to drop below the transcription threshold again. The oscillatory effect of fast increasing levels of Dkk in the cells environment is diminished by an increase of Dkk diffusion. After termination of transcription Dkk is degraded fast, slowly moving wnt is still present to bind to the receptors and β -catenin levels increase again. Snap shots of such a scenario is shown in Fig. 6.10 for slow (d) and faster (e) Dkk diffusion. For faster

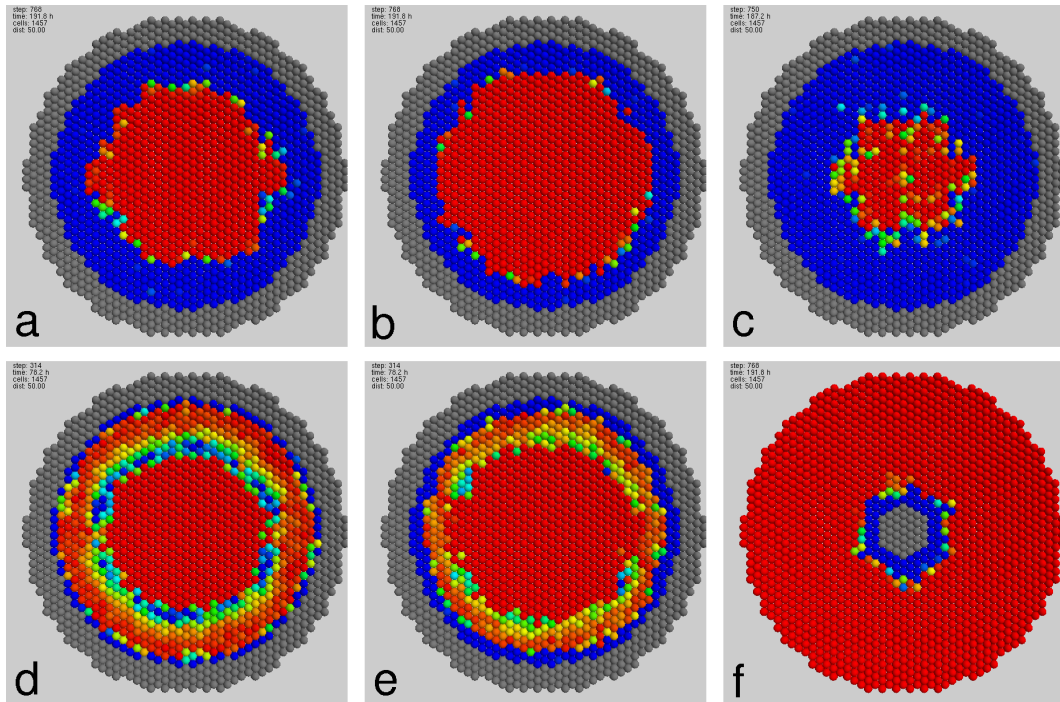


Figure 6.10: Resulting GS pattern of simulations in concentric geometry. Simulation results for various parameter sets in concentric cultures. Grey cells are RL-ET 14 cells, colored cells have different GS activities, ranging from red: no activity to blue: full activity. a) Reference Simulation of a stable GS layer using the parameter given in Table A.5. b-d) are snapshots showing GS pattern of various simulations of the sensitivity analysis. b) The most direct parameter affecting expression of the target genes is the β -catenin-threshold. Raising it results in a smaller stable GS-positive layer. c) The equilibrium concentration of receptor-bound wnt is affected by binding and unbinding rates of both ligands. A smaller unbinding rate for wnt for example results in a broader stable GS-positive layer. d) Acceleration of the Dkk dynamics leaving wnt-related parameter fixed results in oscillations as indicated by the wave of GS expression. e) The range of oscillations depends on the diffusion coefficient. For a faster diffusion of the antagonist Dkk (greater D_{dkk}) the range of oscillations decreases. f) Inversion of the geometry results in a much thinner GS layer.

diffusion the GS wave is less pronounced. In contrast to (d) it vanishes completely before reaching the center of the colony.

The period of the oscillation changes with the delay of Dkk production Δt_{dkk} . Decreasing the delay shortens the time until wnt is replaced at the receptors and therefore reduces the total time until wnt is bound to the receptors again. A similar effect is found for a faster production or degradation rate of Dkk. The strength of the effect depends on the ratio of the considered process, delay or production, to the total oscillation period. Locally for each cell it can be understood as a damped oscillation with the transport acting dissipative.

Modeling a liver lobule: hepatocytes envelop wnt-producing cells.

A simple way of mimicking the geometry of the liver lobule, where a small number of GS-positive cells close to the central vein is enclosed by numerous GS-negative cells of the periportal space, is to simply reverse the geometry and to place the wnt-source in the center

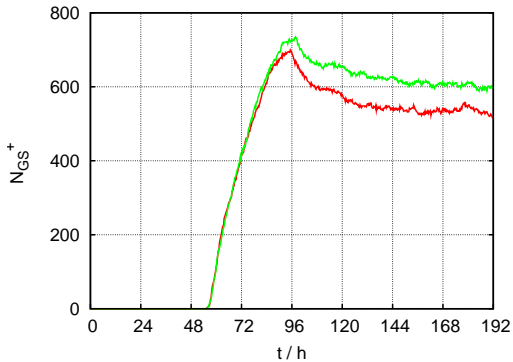


Figure 6.11: GS activity in concentric colony resembling the experiment. After an overshoot due to following Dkk production and wnt replacement at the receptors as described in the text, GS activity, quantified by the number of cells expressing GS N_{GS+} , equilibrates in the colony. An increasing GS activity in comparison to the reference simulation (red) is achieved by increasing the number of RL-ET 14 cells in the outer layer that produce wnt (green).

of the colony as shown in Fig. 6.6. Using the same parameter set that led to a stable GS activity within a layer a couple of cells thick in this case results in a much steeper β -catenin gradient and in a much smaller GS-positive layer of only 2-3 cells. For the dilution of the signal with radius r , the gradient of wnt and Dkk concentrations is much steeper in case of a wnt source at the center as in the liver lobule. Thus the pattern in the liver and in a concentric co-culture might be explained simply by the reverse geometries without necessity of complicated considerations of flow in the lobule. For the small number of wnt-positive cells no overshoot of GS activity is seen (Fig. 6.12, red curve), but increasing the number of wnt-positive cells and the amount of wnt produced in the center results in an extended GS-positive layer, therefore higher Dkk-levels, replacement of wnt at the receptors and the overshoot in GS activity seen in Fig. 6.12, green curve. For modeling the overshoot the effect of a higher total Dkk production and therefore a decreased fraction of wnt-binding receptors can also be achieved by increasing the receptor binding rate of Dkk k_{dkk}^{on} as shown in Fig. 6.12, blue curve. This suggests a higher receptor affinity of Dkk in comparison to the one of wnt.

6.5.2 Simulations of a random co-culture

Another geometry apart from the concentric pattern was applied in the co-culture experiments. Small islands of hepatocytes at random positions are surrounded by RL-ET 14 cells. Here the cell type of each individual cell was picked at random with probabilities leading to a various fractions of RL-ET 14 cells. Fractions of 2% 10%, 25%, 33% and 40% of RL-ET 14 cells and the parameter set of the reference simulation were used. GS expression was seen at

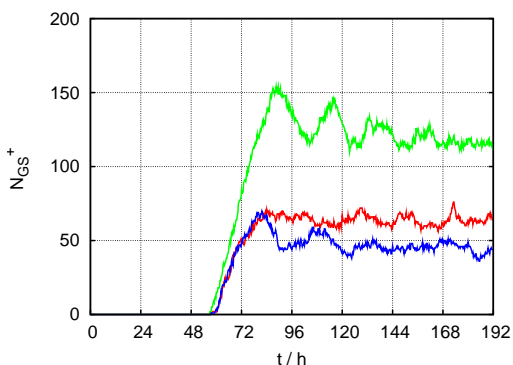


Figure 6.12: GS activity in lobule-like geometry. In this geometry no overshoot and subsequent equilibration is seen for simulations using the parameter set of the reference simulation (red). An overshoot is produced by increasing the wnt signal from the endothelial vein by increasing the number of wnt-positive cells. This results in a thicker GS-positive (and Dkk expressing) layer and an overshoot (green). The same effect can be achieved at the receptor level by increasing Dkk receptor affinity, which as a consequence reduces the final GS activity (blue).

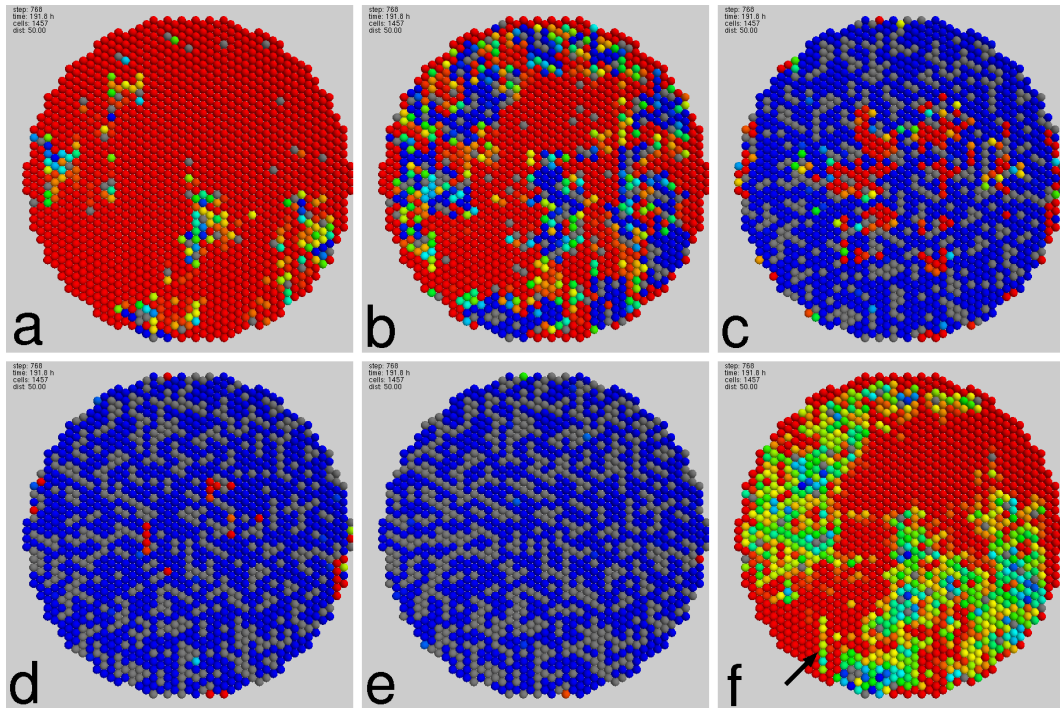


Figure 6.13: Resulting pattern of random order simulations. GS expression strongly depends on the density of RL-ET 14 cells as seen for fractions of a) 2%, b) 10%, c) 25%, d) 33% and e) 40% RL-ET 14 cells. Grey cells are RL-ET 14 cells, colored cell have different GS activities, ranging from red: no activity to blue: full activity. a, b) GS-positive cells occur only near local aggregations of RL-ET 14 cells. Confluent GS expression is found above a fraction of 40% RL-ET 14 cells. f) wnt-bound receptors for a). GS-positive cells are located within the areas of higher receptor occupation (red and blue encode low and high receptor occupation, respectively). Note the stochasticity e.g. in the conformation indicated by the arrow.

all densities in some cells (see Fig. 6.13). At a small densities GS expression does not develop in the neighborhood of single RL-ET 14 cells, but requires local aggregation of a number of wnt-producing cells. They do not need to be in direct contact, but in sufficient proximity to enhance each others signals. For a colony containing only 2% of RL-ET 14 cells, the number of GS-positive cells is smaller than the number of RL-ET 14 cells. With increasing density of RL-ET 14 cells GS expression becomes more frequent. But GS expression is incomplete over a wide range of RL-ET 14 densities. No total coverage of GS activity is found below a fraction of RL-ET 14 cells of 40%.

6.6 Discussion

GS expression is observed as a stable property of hepatocytes. In a culture containing mixture of GS-positive and GS-negative hepatocytes only a small modulation of individual GS expression, but no *de novo* expression or complete cessation has been observed [208]. GS-positive hepatocytes persist, but do not induce GS-expression in neighboring hepatocytes [223]. In contrast, overall expression of the wnt-antagonist Dkk in transgenic rats

is sufficient to cause a periportal phenotype in the whole lobule [204, 205]. Supported by experimental findings of constitutive β -catenin expression or APC knock-out strongly these results strongly suggest the canonical wnt-pathway for GS regulation. The source of the wnt signal at the central vein in contrast to the portal triad could be a functional important remainder of liver development where wnt plays a major role in zebra fish, frog and chicken [224–226].

After introducing a multi-scale model for transport, receptor and transcription dynamics, a parameter set has been identified that qualitatively reproduces the experimental results of the concentric co-culture experiment briefly summarized in the first section of this chapter. Variations in the parameters have been tested for their effects on the observed spatio-temporal pattern. In contrast to the experiments the model does not include GS expression in absence of a β -catenin-stabilizing environment like a continuous wnt-signal as found in co-culture of GS-positive and GS-negative hepatocytes. The dependence of GS activity on the β -catenin-balance therefore suggests some kind of stabilizing positive feedback.

Interestingly, the model explains exactly the overshoot observed after CCl_4 intoxication by this lack of stabilization. It predicts a delayed production of the wnt-antagonist Dkk, replacement of wnt by Dkk at the receptors and loss of GS activity in cells with values of β -catenin-concentrations only little above the transcription threshold.

The overshoot can be turned into oscillations of β -catenin and its targets by a variation of the parameters defining the Dkk dynamics. Another type of oscillations provide a clock in the paraxial presomitic mesoderm for segmentation and involve the wnt-pathway. Strikingly, expression of β -catenin-targets and inhibitors of the wnt-pathway exhibits such oscillations, while no evidence for an oscillating β -catenin-level was found [227]. In contrast, β -catenin-concentrations established a clear anterior-posterior gradient [228]. This means that another quantity encoding the regulatory cues for the expression machinery must exist apart from the total β -catenin-concentration. According to the oscillations of β -catenin-targets it must be closely related to the wnt-pathway, like concentrations of nuclear β -catenin-buffers or activity of anchor molecules, that regulate nuclear β -catenin-concentration [229]. The precise regulation of β -catenin is also essential in the liver development of *Xenopus* [225] and in somitogenesis, which gives rise to liver development [228, 230]. The presence of such a mechanism in liver development is closely related to liver patterning and development of the local order, which may be related to the observed overshoot.

A simple inversion of the concentric geometry by placing the wnt-positive cells inside a small circular region in the center reproduced the pattern of GS expression found in the liver lobule, and provides a hypothesis which is easily testable. Applying the reference parameter set the overshoot after CCl_4 intoxication was not reproduced for this geometry. Adjusting slightly the Dkk receptor affinity was able to introduce such an overshoot. This suggests a greater receptor affinity for Dkk than for wnt.

The interaction with other pathways was not necessary to explain the mechanism for restricting GS expression in the liver. The *hras/erk* pathway as a complement for wnt/ β -catenin -signaling [218] may contribute information rather for the periportal zone of ureogenesis than the pericentral space. Even dependence of the regulation of APC, the ‘zonation keeper’ [204], and Axin on the wnt signal that is released at the central vein, and internal feedbacks cannot be ruled out completely. Regulation of these members of the destruction complex can be expected to reveal important information not only on regulation of GS, but also on many other processes involving the wnt-pathway. For example, regulation of Axin degradation by APC has been shown to play an important role for amplifying the wnt signal [202].

Inspired by the co-culture experiments of random pattern a series of simulations ini-

tialized with random positions of the hypothesized wnt-sources has been performed. The results suggest, that for GS activity higher wnt concentrations are necessary, than a single cell can supply. Summing up the wnt-signal of many cells by local aggregation was necessary for establishing β -catenin concentrations above the transcription threshold. Interestingly, a complete coverage of GS activity was only found for fractions above 40% RL-ET 14 cells. Therefore, the suggestion is made to test the dependence of GS activity on the density of RL-ET 14 cells.

In biological systems all receptors are dynamic. They are regulated, internalized and externalized, which might be another mechanism for transport. However, Bollenbach *et al.* [220] did not observe any qualitative difference to passive transport. Regulation of the receptor densities represent another important aspect in unveiling the control mechanisms of cellular pathways.

The construct of a honeycomb lattice is a completely regular structure. However, many hepatocytes adopt a hexagonal shape, and even trigonal honeycomb patterns with little deviations are observed in cell cultures. Stochastic treatment of the transport processes and receptor dynamics was used compensate the regularity to some extent. Nevertheless, a more realistic representation of cells, for example, by Voronoi constructs similar to Schaller *et al.* [70], would be an advance, but also require a much more complex treatment of surface discretization and related stochastic processes. Integration of this model into a fully dynamical system including cellular motion and proliferation is aimed as a next step in the context of modeling liver regeneration [221].

In summary, the experimentally observed patterns were reproduced with this simple representation. Variations of parameters and geometry suggested a number of easily testable hypothesis. Certainly, the co-culture experiments should be repeated scaled down and in an inverse geometry to include a more lobule-like geometry and to test, whether this geometry is one key to the zonation problem.

7

Conclusion

In the course of this thesis the potential of individual cell-based models based on a simple spatial representation of biological cells has been developed by extending the simple and mainly biophysical IBM introduced in Chapter 1 by differentiation and intracellular regulation, which are fundamental quantities that distinguish biological cells from physical particles. Following the IBM approach all individual cells are represented as physical particles of spherical shape. Cell-cell and cell-matrix interaction are modeled by a modified Hertz potential for adhesive, elastic spheres, which is based on the assumption of a homogeneous, linear material. Based on these simplifications and in contrast to other more realistic and complex approaches this interaction potential enables simple and fast calculation of interaction forces and contact areas of the cells. Cell motion is modeled by a Langevin equation using a conceptual analogy between cellular and Brownian motion.

The examination of the simple basic IBM in Chapter 2 regarding applications that are consistent with the simplifications included motion in cell populations, cell sorting and compression of multi-cellular aggregates. Simulated cell motion in cell populations that uses Langevin forces generally deviates from Brownian motion, because the random movement of Brownian particles is controlled by the physical temperature which links fluctuations and dissipation both mediated by collision with small fluid particles on short time scales. Different from this, cells perform an active random movement able to control the autocorrelation amplitude of their random motion by cell-internal mechanisms. For example, the strict application of Langevin equations of motion as for interacting Brownian particles suggests a faster movement with increasing particle density. For most cell types, e.g. for epithelial cells, this is not found. Hence to take into account that eukaryotic cells generally move slower at high densities, the amplitude of the autocorrelation function of the random force term was modified and used in the following of this thesis.

Cell sorting by differential adhesion was considered. It was found that cell sorting could not be quantitatively explained by differential adhesion within the model approach since the resulting multi-cellular configurations displayed only local sorting reflecting that the cells got stuck in local energy minima. In order to test the possible influence of long-range forces on sorting as done by Palsson *et al.* [75] the model was extended by adding a long-range force tail which indeed led to improved sorting but no complete sorting could be achieved for large cell population sizes beyond about 1000 cells. In order to sort completely, the cells probably need to extend their horizon either by longrange signals, which could be provided

by chemical signaling, or by significantly larger fluctuations in shape and space, that allow them to explore their environment and to find the global minimum in sufficiently short time.

Modeling compression of multi-cellular aggregates has shown a good quantitative agreement for the relaxation curves. However, the aggregate shapes have shown less rounding off as, for example, in the experiments by Forgacs *et al.* [108]. Moreover, Forgacs *et al.* used a one-dimensional viscoelastic model to fit their experimental findings and their relaxation times predicted based on this model were about an order of magnitude below those found with our model. A deeper understanding of the visco-elastic behavior of cell aggregates would need more experimental and simulation work. For example, biological cells respond to stress in a non-linear and viscoelastic way, which is not reflected by the model used throughout this work. The Hertz potential does neither describe viscoelastic deformation nor different detachment dynamics caused by reorganization of adhesion complexes. The viscous effects observed by compression of cell aggregates in this thesis result from a re-arrangements of cells within the aggregate but not from a viscous response of the cells itself. Moreover, the model assumes approximately spherical cell shapes, which may be significantly violated in compression experiments in case the compression occurs rapidly. Because both processes - viscosity effects of the individual cells and large deformations - may be crucial in a compression experiment, neglecting them led to the failure of this simple physical IBM to model the dynamics of such compression experiments. As discussed in Chapter 2, despite some of the experimental observations in sorting and compression could be well captured, a completely quantitative modeling of biophysical observations in sorting and compression simultaneously would probably need a more detailed and complex representation of processes on the sub-cellular scale than those included in the simplified spherical cell model used in this work. Rephrased this means, that a successful modeling of cell reorganization processes in general and these experiments in particular might need a sub-cellular resolution. However, for growth phenomena, in which extensive cell-cell reorganisations on small timescales do not occur, the possible shortcomings in modeling sorting and compression experiments are not limiting. The largest part of the thesis was devoted to growth and differentiation phenomena where the IBM's have been extended to multi-scale models that include the subcellular control.

In the following part of the thesis the IBM has been extended to characterize each cell by another quality: cellular differentiation. Motivated by recent studies on noise in cellular regulation a model of noise-driven cell regulation is included in each individual cell. The resulting hybrid model has well reproduced the oxygen-dependent growth and subsequent chondrogenic differentiation of MSC. Both, the characteristic size distribution of single cell derived clones and the occurrence of functional chondrocytes in multi-cellular spheroid of the expanded cells is covered by the model. Particular importance for successful modeling were clearly given by the spatial representation of individual cells and the facilitated consideration of the local environment of individual cells. Both, the local oxygen concentration and cell-cell contacts in multi-cellular spheroids, are crucial for modeling differentiation and induction of a functional phenotype in the spheroids. These results highlight the importance of using IBM approaches that include a spatial representation for the modeling of multi-cellular biological phenomena. In particular, the concept of unifying a spatial, physical representation and the IBM approach of individual cellular differentiation has been proven efficient in tackling the interplay of cell fate decisions and cell environment.

In the following study the advantages of IBM were exploited by recording each individual cell fate in order to address the question of cell plasticity in MSC derived colonies. Based on the validated parameter set resulting from modeling growth and differentiation, average transition times to stem cell states and differentiated states provide first predictions of cell

plasticity of MSC *in vitro*. Also predictions on the oxygen-dependent regeneration of the differentiation structure in MSC populations have been made closely following a protocol for a similar experiment on hematopoietic progenitor cells. Fluctuations and outlier cells turn out to be the important aspect for understanding this biological system. Regeneration of the differentiation structure of the whole population from the subpopulation of differentiated cells at high oxygen depends on single cells that escape the quiescent differentiated states by naturally occurring fluctuations while most of the cells stay quiescent. These outliers enter proliferative states and give rise to the progeny that populates less differentiated states. This scenario represents a good example for the usefulness of IBM approaches, since it is based on fluctuations that differential equations for a population average would not include. Additionally, the variation of biophysical parameters links biophysical to biological phenomena and facilitates an explanation for effects seen in confluent cell culture, which again is based on the spatial biophysical representation. Finally, the possibility to distinguish between individual cells has led to predictions on the composition of the stem cell pool, which can be expected to be important for thorough a understanding of the underlying organization principles. Following the IBM approach these *in silico* experiments have generated predictions that anticipate results of currently developed single cell tracking and formulate hypotheses to be purposefully addressed.

However, a basic property of MSC cultures, the persistent clonal heterogeneity of MSC *in vitro* and the radial gradient in differentiation marker expression found in large colonies of human MSCs, was not covered by the model. Additionally, the concept of aging as a 'memory' of cells was introduced and takes further advantage of the IBM concept by introducing an inheritable individual property. Motivated by recent results on epigenetics, it was assumed that cell divisions destabilize stem cell states, while the average noise level is set by the environment. With this extension the experimentally observed heterogeneities, both spatial and clonal, could be reproduced by the model. Following this concept of aging as a destabilization of stem cell states, the results suggest, that an optimal age for differentiation of MSCs exists. Additionally, the model yielded results of *in vivo* aging of MSC that captures the results on rat MSCs qualitatively. Realization of this aging concept is based on the inheritable property 'age', which represents another individual quality, that in contrast to differentiation fluctuations can not vanish but develops growing differences between individual cells. The success of modeling such a complex phenomenon like the heterogeneity of clones therefore is strongly facilitated by the IBM approach and agrees with the concept of epigenetics as an individualization of biological cells.

After the phenomenological approach to cell differentiation, a detailed molecular mechanism of individual cellular regulation was studied. Glutamine synthetase activity, a key enzyme in the liver, is restricted to a precise pattern, which is crucial for liver function. Expression of the gene for glutamine synthetase is regulated by the wnt pathway. A model for the transport of the involved signaling molecules and for the pathway itself extended the IBM approach towards including the molecular level by direct representation of the interactions of the key molecular components. Modeling the *in vitro* co-culture experiments generated some easily testable predictions on the influence of culture geometry and a possible explanation for *in vivo* zonation. Especially for modeling the emergence of this spatial pattern in hepatocytes the IBM approach with its spatial representation of single cells has turned out to be the generic approach that takes the individuality of cells into account.

This thesis has shown that this IBM approach which employs a simple spatial representation of cells permits a surprisingly detailed modeling of biological phenomena that involve a spatial variation of environmental conditions. Considering the very distinct regulatory states of different cells apart from their varying environment every single cell has to be regarded a

decision making entity. Their interplay guarantees - for example - the orchestration observed in metazoa. On the other hand, for understanding the biological systems, e.g. the regeneration experiments, an understanding and modeling of the fluctuations that are inherent is clearly crucial. Consequently, combining the IBM approach with a spatial representation and stochastic regulation principles has generated interesting and unexpected results. Importantly, the resulting predictions can be tested in the 'wet lab', because all simulations followed closely *in vitro* protocols. This close interplay of hypothesis-driven research has been proven very useful in this thesis and represents a basic demand of the interdisciplinary research aimed at systems-level understanding of biological processes.

Acknowledgements

Here I want to thank all the people who have contributed to this thesis in one way or the other:

In the first place I want to thank my supervisor Dr. Dirk Drasdo, who made this thesis possible and who had always time and advice for me. His exceptional ability to find the right words and funding in the most hopeless situations deserves special mention.

A perfect roommate for scientific discussion and beyond has been Dr. Joerg Galle, also in other locations (somewhere and sometime on the KarLi...). Thank you for your uncomplicated way of making fun out of terribly serious and interesting science.

Further thanks go to Prof. Peter Stadler and his secretary Petra Pregel for their completely extraordinary way to handle problems, 'Personal-Dezernat' and parties.

I also want to thank Dr. Hans Binder and his secretary Corinna Dittman for taking care about the administration side of my position. The same to Sylvia Henger, with whom sharing the office was a pleasure.

Many thanks go to my collaborators in the 'wet labs', Michael Zscharnack at the BBZ and Alexandra Stolzing at the Fraunhofer Institute, and at the computer Martin Hoffmann, who is (hopefully) having a good time in Maastricht.

Of course, many, many thanks to all the bioinformaticians in this group for having fun, food and fresh 'bierinformatik' together, which includes studying this drink in many places and occasions. But the activities within the group stretch from games to cooking, from barbecue to wine testing, from table tennis to 'Umzug tragen', from climbing to classical music in the Gewandhaus. Thanks to Sonja Prohaska, Sven Findeiß, Dr. Dr. Steve Hoffmann, Alex Donath, Manja Lindemayer Marz (yes this thesis took a while), Henry Wirth, Axel 'Lutz' Mosig-'Rittberger', Guido *cough* Fritzsich, Anke Busch, Konstantin Klemm, of course, AT and Börni from Vienna and all the others...

And finally, special thanks go to my already doctorified girl friend Paula for her sensitive mixture of patience and motivation (she knew what I was talking about) and my family for keeping me going.

Appendix

A.1 Abbreviations

2D/3D	two-/three-dimensional
DAH	Differential Adhesion Hypothesis
FACS	Fluorescence Activated Cell Sorting
GS	Glutamine Synthetase
IBM	Individual (cell) Based Model(ing)
MSD	Mean Square Displacement
MSC	Mesenchymal Stem Cells
PDE	Partial Differential Equation
pO_2	Oxygen Tension = Oxygen Partial Pressure
ROS	Reactive Oxygen Species

A.2 Details of Implementation

Time step control

Dynamic control of the time step in the simulations was required to guarantee numerical stability. Too big displacements result in e.g. non-physical penetrations of cells and oscillations. To avoid these big displacements the equation of motion (1.21) is solved again for a smaller time step $\Delta t' = \Delta t/2$, if any displacement $|\Delta \vec{x}_i|$ in an update exceeds a certain threshold Δx_{\max} , which is chosen relative to the smallest cell radius. To facilitate as fast simulations as possible the time step is doubled $\Delta t' = 2\Delta t$ in the next time step, if in a simulation step no displacement greater than a lower threshold Δx_{\min} occurs.

Solving the sparse matrix system

Regarding the linear system $Ax = B$ to solve, the non-diagonal entries coupling the equations are caused by cell-cell contacts (remember $\gamma_r = \gamma_t$). Since the interactions are symmetric, this results in a symmetric matrix A , which is also strictly diagonal dominant for non-vanishing contribution of cell-substrate or cell-medium friction. For the cell numbers of interest, $\approx 10^3 - 10^5$, and the limited number of neighbors n for each cell (in dense sphere packing it is $n = 12$) the matrix is very sparse. The matrix' properties of symmetry, strictly diagonal dominance and very sparse occupancy enables the use of time and memory saving algorithms. Because the non-diagonal entries represent direct cell-cell contacts, the system is very sparse allowing the use of memory and time saving optimized libraries for sparse matrices [231, 232].

Solving the reaction-diffusion equation

Eq. (1.24) was solved on a cubic lattice using the Forward Euler Method because of its simplicity. The very limiting stability criterion for the time step Δt_{diff} can be compensated by parallelization. The lattice constant was set to the maximal cell diameter.

A.3 Materials and Methods

Isolation and cultivation of MSCs from ovine bone marrow aspirates.

Bone marrow aspirates were obtained with 15-gauge Jamshidi needles from the iliac crest of 18-24 months old Merino sheep. Heparinized aspirates (500 I.E. per ml; Ratiopharm Ulm, Germany) were diluted 1:3 with phosphate buffered saline (PBS; Gibco, Karlsruhe, Germany) and agglutinates were removed by filtration with a 70 μm pore filter.

The samples were carefully poured into a Leucosep® tube with a porous barrier (Greiner Bio-one, Frickenhausen, Germany), onto a Ficoll separating solution (density 1.077 g/ml; Biochrom, Berlin, Germany) and centrifuged 10 min at $1000 \times g$ at 20°C . Enriched mononuclear cells including MSCs above the porous barrier were harvested and washed twice with PBS by centrifugation for 5 min at $500 \times g$. Cells were resuspended and seeded at $2 \times 10^4 \text{ cells/cm}^2$ in tissue culture flasks with high glucose Dulbecco's modified Eagle's medium (DMEM; Gibco, Karlsruhe, Germany) supplemented with 10% FCS, 100 U/ml penicillin, and 100 $\mu\text{g/ml}$ streptomycin (both Biochrom). Cultures were maintained at 37°C in a humidified atmosphere containing 95% air and 20% O_2 - 5% CO_2 or 5% O_2 - 5% CO_2 balanced with N_2 in a tri-gas incubator (Thermo Fisher Scientific, Dreieich, Germany). Medium was changed twice weekly. After 14 days at near confluence of the cultures the cells were detached by trypsin/EDTA (0.25%/ 0.05 mM; Biochrom) and used for single cell cloning (see below) or for subcultivation. For that, cells were passaged at 5000 cells/ cm^2 and cultured to reach 80-90% confluence of passage two before the final trypsinization and use for chondrogenic differentiation in pellet culture.

Spargue dawley rats of an age between 3 weeks and 12 month were purchase from the University breeding house or Charles River. Bone marrow cells were obtained centrifugally from tibias and femurs according to [233] and MSC isolated according to [195].

Passage (P0): Cultures were maintained at 37°C in a humidified atmosphere containing 95% C air and 20% O_2 - 5% CO_2 or 11% O_2 - 5% CO_2 or 5% O_2 - 5% CO_2 balanced with N_2 in a tri- gas incubator (Thermo Fisher Scientific, Dreieich, Germany). Medium was changed twice weekly. After 14-18 days the cells were trypsinized (Biochrom) and used for single cell cloning (see below) or sub-cultivation. For that, cells were passaged at 5.000 cells/ cm^2 and cultured to reach about 90% confluence of the respective passage.

Clonal expansion assay

Single cell clones were generated by using limited dilution method. Therefore, cells were seeded at one cell per well in a 96 well plate at 5% and 20% pO_2 . Each well was checked and all wells that contain just a single cell were marked. After 5 days, the cell numbers of 30 single cell derived clones of 5% and 20% pO_2 cultures were counted by microscopy.

Comparison of single cell derived clones with mixed population

Single cell clones were generated by clonal expansion assay (see above). After sub-cultivation in 12 well plates (P2) clones were cultivated in 75 cm^2 flasks (P3) for following chondrogenic

differentiation in pellet culture (see below). In parallel 8 of 36 clones from P2 were randomly chosen and seeded as well as P2 cells of the mixed population at 1000/cm² in 48 well plates with expansion medium. Cells were counted after six days in triplicate.

Analysis of spontaneous differentiation

The analysis of spontaneous differentiation of ovine cells was performed on cytopsin samples from P1. Per sample 2×10^4 cells were re-suspended in 100 μ l DMEM and centrifuged with a Shandon Cytospin®4 Cytocentrifuge [Thermo Fisher Scientific, Waltham, USA] on a glass slide (1.000 rpm, 3 min). After drying for 30-60 min the samples were stained by immunocytochemistry (see below). The analysis of spontaneous differentiation of rat and human cells was performed in well plates using aggrecan staining. The single cell clones were selected and further cultured in 24-well plates in normal medium. Cells were fixed in 4% paraformaldehyde for 10 min and washed in PBS. Cells were stained with a 1:50 dilution of anti-aggrecan (Acris Antibodies, Herford, Germany) for 60 min at RT. After washing and incubation for 45 min with a secondary antibody (for rat MSCs: Cy3, [Jackson ImmunoResearch, 1:750]; for human MSCs: Alexa Fluor®488 goat anti-mouse [Invitrogen, Karlsruhe, Germany, 1:1000]), the cells were washed again and analysed using a fluorescent microscope (Olympus).

Detection by 3-amino-9-ethyl-carbazol substrate (AEC). The cryosections (8 μ m) or cytopsin were blocked with allogenic serum (1:10 diluted in PBS) for 30 min at 37°C followed by incubation with the primary antibody (collagen type II: mouse monoclonal antibody [Clone: II- 4C11; MP Biomedicals, USA], diluted 1:2000 in PBS; aggrecan: monoclonal mouse antibody [Acris Antibodies, Herford, Germany], diluted 1:50 in PBS; Sox9: rabbit polyclonal antibody [Millipore, Schwalbach, Germany], diluted 1:200 on PBS). After washing with PBS, the secondary antibody of peroxidase-conjugated goat-anti-mouse (or anti rabbit) IgG (Jackson ImmunoResearch, Cambridgeshire, UK; diluted 1:50 in PBS) was added for 1h at 37°C. Immunostaining was developed by AEC substrate. Cell nuclei were counterstained with Meyer's hematoxylin (Lillie's Modification; DakoCytomation, Hamburg, Germany).

Detection by fluorescence staining. The sections were fixed in 4% formaldehyde for 20 min and in 100% ice-cold methanol for 10 min. Following, samples were washed with PBS, blocked for 30 min with allogenic serum (1:10 diluted in PBS). Sections were incubated with the aggrecan primary antibody (see above), diluted in PBS/0.3% Triton X, overnight at 4°C. After washing with PBS, the secondary antibodies Alexa Fluor®488 goat anti-mouse IgG, diluted 1:1000 in 0.1 μ g/ml DAPI/PBS/0.3% Triton X-Solution, were added for 1 h at 37°C. Finally, after washing with PBS, sections were coated with 90% Glycerol in aqua dest. for fluorescence stabilization. The fluorescence was examined by microscopy (Carl Zeiss Axiovert 200).

CFU-F assays

Ovine/human MSC: After isolation of mononuclear fraction from bone marrow by Ficoll density gradient centrifugation, 2×10^4 mononuclear cells/cm² were seeded in 10cm Petri dishes. After 14 days colonies were washed twice with PBS and fixed with methanol for 5 min. After removal and air drying (5 min) cultures were incubated for 5 min in giemsa stain solution (1:2 in aqua dest; Sigma-Aldrich, Deisenhofen, Germany). Cultures were washed twice with water and colonies with more than 50 cells were counted.

Rat MSC: The CFU-F assay was performed according to the technique described by Kuznetsov *et al.* [234] with modifications. 2×10^6 mononuclear bone marrow cells were

suspended in 0.5ml media and plated on 55cm² petri dishes in DMEM/low glucose medium (10% serum). Medium was first changed after 5 days and then regularly every 3 days. After 14 days the cells were washed with PBS, fixed with ethanol, stained with methylen blue, photographed and analysed as previously described [235].

Pellet preparation and culture

Pellets were prepared according to the protocols by Mackay *et al.* [236] and Yoo *et al.* [237]. Briefly, a total of 0.5×10^5 MSCs were placed in a 15 ml conical polypropylene tube, centrifuged at $500 \times g$ for 5 min at 20°C and re-suspended in DMEM without serum for washing. After a further centrifugation step the cells were re-suspended in serum-free, chondrogenic medium (Chondrogenic Differentiation BulletKit®) supplemented with 10 ng/ml TGF- β 3 (both Lonza, Wuppertal, Germany) and cultivated for 2, 7 and 14 days. The chondrogenic medium was changed twice a week.

Immunohistochemistry

Immunohistochemistry of cryosections (8 μ m) were performed according to the two step indirect method. The sections were fixed in 4% formaldehyde for 20 min and in 100% ice-cold methanol for 10 min. Following, samples were washed three times with PBS and then blocked for 30min with sheep serum (1:10 diluted in PBS). Sections were incubated with primary antibody overnight at 4°C (collagen type II: mouse monoclonal antibody [Clone: II-4C11; MP Biomedicals, USA], diluted 1:2000 in PBS/0.3% Triton X; SOX 9: mouse monoclonal antibody [Millipore, Schwabach, Germany], diluted 1:200 in PBS/0.3% Triton X). After washing with PBS, the secondary antibodies Alexa Fluor®488 goat anti-mouse IgG (Invitrogen, Karlsruhe, Germany) for collagen type II and Alexa Fluor®555 goat anti-rabbit IgG (Invitrogen) for SOX 9, diluted 1:1000 in 0.1 μ g/ml DAPI/PBS/0.3% Triton X-Solution) were added for 1 h at 37°C. Finally, after washing with PBS, sections were coated with 90% Glycerol in aqua dest. for fluorescence stabilization. The fluorescence was examined by microscopy (Carl Zeiss Axiovert 200). For staining with peroxidase-conjugated secondary antibody after incubation with the primary collagen type II antibody (see above) and washing with PBS a secondary antibody of peroxidase-conjugated goat-anti-mouse IgG (Jackson ImmunoResearch, Cambridgeshire, UK; diluted 1:50 in PBS) was added for 1 h at 37°C. Immunostaining was developed by 3-amino-9-ethyl-carbazol substrate. Cell nuclei were counterstained with Mayer's hematoxylin (Lillie's Modification; DakoCytomation, Hamburg, Germany).

DNA quantification of pellet cultures (PicoGreen assay)

To assess proliferation of the MSCs within pellet cultures the DNA concentration was measured by Quant-iT™ PicoGreen® dsDNA Assay Kit (Molecular Probes, Eugene, USA) according to the manufacturer's instructions. For preparation, each pellet sample was re-suspended in 200 μ l papain digestion buffer and digested for 16 h at 60°C. After digestion, samples were diluted in Tris Borat EDTA-buffer for DNA measurement. For quantification, a well-defined DNA stock solution (Lambda-DNA Molecular Probes) was used. The fluorescence of negative, cell-free controls was subtracted from the fluorescence values of samples. Sulfated Glycosaminoglycan (sGAG) quantification Pellets were digested in 0.2 ml papain digestion buffer (5 mM L-cysteine, 5 mM EDTA, 100 mM Na₂HPO₄, pH 6.5) and incubated for 16 h at 60°C in a thermomixer (Eppendorf, Hamburg, Germany) with 5 μ l papain-solution (10 mg/ml; Sigma-Aldrich). Samples of 40 μ l were assayed for the

proteoglycan contents by quantifying the sulfated GAG content using 500 μ l of the 1,9-dimethyl-methylene blue dye (0.016 g/l DMMB, 5 ml/l C₂H₅OH, 2 g/l NaCOOH, 2 ml HCOOH, pH 3.0) binding assay (Roche, Basel, Switzerland). Absorbance was determined at 595 nm in a photometer and the concentration of GAG was extrapolated from a standard curve based on shark chondroitin sulfate within a range of 10-100 μ g/ml. The sGAG quantities of pellet cultures were normalized to DNA content, measured by PicoGreen assay.

Statistical analysis

Experiments were accomplished using MSCs from at least four donors. The results were expressed as mean \pm standard deviation (SD). The significance of the results were analysed by Student's t-test, with $p < 0.05$ considered as significant.

A.4 Simulation Parameters

A.4.1 Parameters used in Chapter 3

Model	Parameter		Value	Sim	Source
stem cell dynamics	Randomization Rate	R	$2.5e - 4 \text{ s}^{-1}$	2D/3D	Fitted
	Stem Cell Fluctuation Strength	σ_0	0.15	2D	Fitted
	Differentiation Threshold	α_d	0.85	2D/3D	Set
		$(\alpha_s = 1 - \alpha_d)$			
	Hill Coefficient	n	5	2D/3D	Set
	Dissociation Constant	k	0.3	2D/3D	Set
	Minimal Number of Neighbours	N_c	6	3D	Set
	Transition Rate	W_0	0.01 s	3D	Fitted
	Transition Threshold	α_c	0.15, 0.5, 0.85	3D	Set
IBM	Minimal Cell Radius	R_0	$8 \mu\text{m}$	2D/3D	Measured
	Minimal Cell Volume	V_0	$V(R_0)$	2D/3D	
	Proliferation Rate	r	$1.5 - 2.1/\text{day}^*$	2D	Fitted
	Young's Modulus	E	450 Pa	2D/3D	[238]
	Contact Inhibition Threshold	F_c	$1 \times 10^{-9} \text{ N}$	2D/3D	Fitted
	Poisson's Ratio	ν	0.4	2D/3D	[239]
	Friction Constant	η_{ij}	$3 \times 10^7 \text{ Ns/m}$	2D/3D	Set
	Cellular Diffusion Coefficient	D_C	$4 \times 10^{-12} \text{ cm}^2/\text{s}$	2D/3D	[106]
	Cell-Cell Anchorage	ϵ_{cc}	$6 \times 10^{-5} \text{ N/m}$	2D/3D	[91]
	Cell-Substrate Anchorage	ϵ_{cs}	$6 \times 10^{-5} \text{ N/m}$	2D/3D	[91]
diffusion	Oxygen Diffusion Coefficient	D_{O_2}	$0.175 \times 10^{-9} \text{ m}^2/\text{s}$	3D	[149]
	Oxygen Consumption Rate	C_{O_2}	$30 - 65 \text{ fmol/cell/h}$	3D	[149]

Table A.1: Parameters used in the simulations. *The fit of the CFU-F data was achieved assuming a proliferation rate for all cells of 1.5/day for 20% pO₂ and a 1:1 mixture of cells with proliferation rates of 1.5/day and 2.1/day for 5% pO₂.

A.4.2 Parameters used in Chapter 4

Model	Parameter		Value	Source	
Intracellular	Randomization Rate	R	$2.5 \times 10^4 \text{ s}^{-1}$	Fitted	
Regulation	Stem Cell Fluctuation Strength	σ_0	0.15	Fitted	
	Differentiation Threshold	$\alpha_d (\alpha_d = 1 - \alpha_s)$	0.85	Set	
	Hill Coefficient	n	5	Set	
	Dissociation Constant	k	0.3	Set	
Biomechanical Model	Minimal Cell Radius	R_0	$5 \mu\text{m}$	Measured	
	Minimal cell Volume	V_0	$V(R_0)$		
	Proliferation Rate	r	1.9 d^{-1}	Fitted	
	Young's modulus	E	450 Pa	[238]	
	Contact Inhibition Threshold	F_{max}	$1 \times 10^{-9} \text{ N}$	Fitted	
	Poisson's Ratio	μ	0.4	[239]	
	Friction Coefficient		γ_{ij}	$3 \times 10^7 \text{ Ns/m}^3$	
				$1 \times 10^{11} \text{ Ns/m}^{3*}$	[8]
	Cellular Diffusion coefficient	D_{Cell}		$4 \times 10^{-12} \text{ cm}^2/\text{s}$	[106]
	Cell-Cell anchorage	ϵ_{cc}		$6 \times 10^{-5} \text{ N/m}$	[91]
	Cell-Plane anchorage	ϵ_{cp}		$6 \times 10^{-5} \text{ N/m}$	[91]
Qiescent Threshold	F_q		$6 \times 10^{-5} \text{ N/m}$	[91]	

Table A.2: Simulation Parameters used in Chapter 4. * The high friction coefficient η_{ij} was used in 'population regeneration' simulations Sec. 4.3.2 in order to study the influence of biophysical properties on stem cell plasticity.

A.4.3 Parameters used in Chapter 5

Parameter	Value	Model
Initial stem cell noise amplitude σ_0	0.100 0.050	pastic adherence <i>in vivo</i>
Mean noise amplitude σ_E	5% 11% 20% pO ₂ 0.110 0.090 0.075 – – 0.075	human, rat ovine
Randomisation rate R	5.0e-3/s 1.0e-3/s	human, rat ovine
Proliferation rate r	1.47/day 1.90/day	human, rat ovine
Aging rate r_D	2.5e-3/division	all
Differentiation threshold $\alpha_d = 1 - \alpha_s$	0.85	all

Table A.3: Aging related simulation parameters used in chapter 5

Model	Parameter	Value
Chondrogenic differentiation	minimal number of neighbors N_c	6
	transition rate W_0	0.01 / s
	transition threshold α_c	0.5
IBM	minimal cell radius R_0	8 μ m
	minimal cell volume V_0	4/3 πR_0^3
	Young modulus E	450 Pa
	contact inhibition threshold F_c	1 $\times 10^{-9}$ N
	Poisson ratio ν	0.4
	Friction constant η_{ij}	3 $\times 10^7$ Ns/m ³
	cellular diffusion coefficient D_C	4 $\times 10^{-12}$ cm ² /s
	cell-cell anchorage ϵ_{cc}	6 $\times 10^{-5}$ N/m
cell-substrate anchorage ϵ_{cs}	6 $\times 10^{-5}$ N/m	
diffusion	oxygen diffusion coefficient D_{O_2}	0.175 $\times 10^{-9}$ m ² /s
	oxygen consumption rate C_{O_2}	30 – 65 fmol/cell/h

Table A.4: Biophysical and lineage related parameter used in Chapter 5.

A.4.4 Parameters used in Chapter 6

General		
cellnumber	N	1457
Cell Radius	R	$5\mu\text{m}$
Simulation Space		$500 \times 500 \times 20\mu\text{m}$
wnt		
Production Rate	$k_{\text{dwnt}}^{\text{syn}}$	$1\text{e-}2\text{s}^{-1}$
Degradation Rate	$k_{\text{wnt}}^{\text{deg}}$	$1\text{e-}4\text{s}^{-1}$
Receptor Binding Rate	$k_{\text{wnt}}^{\text{on}}$	$1\text{e-}3\text{s}^{-1}$
Receptor Unbinding Rate	$k_{\text{wnt}}^{\text{off}}$	$1\text{e-}1\text{s}^{-1}$
Diffusion coefficient	D_{wnt}	$1\text{e-}14\text{m}^2\text{s}^{-1}$
Contact Hopping Rate	$k_{\text{wnt}}^{\text{hop}}$	$1\text{e-}3\text{s}^{-1}$
Enter Cell Contact Rate	$k_{\text{wnt}}^{\text{in}}$	$1\text{e-}3\text{s}^{-1}$
Leave Cell Contact Rate	$k_{\text{wnt}}^{\text{out}}$	$1\text{e-}3\text{s}^{-1}$
β-catenin		
Production Rate	k_{β}^{syn}	5s^{-1}
Maximal Reaction Rate	V_{max}	15s^{-1}
Michaelis-Menten constant	K_m	30
Inhibitor Dissociation Constant	k_{inh}	10
Transcription Threshold	$\beta\text{-}c_c$	100
Glutamine Synthetase		
Production Rate	$k_{\text{GS}}^{\text{syn}}$	$1\text{e-}2\text{s}^{-1}$
Degradation Rate	$k_{\text{GS}}^{\text{deg}}$	$1\text{e-}4\text{s}^{-1}$
Dkk		
Production Rate	$k_{\text{dkk}}^{\text{syn}}$	$1\text{e-}2\text{s}^{-1}$
Degradation Rate	$k_{\text{dkk}}^{\text{deg}}$	$1\text{e-}4\text{s}^{-1}$
Receptor Binding Rate	$k_{\text{dkk}}^{\text{on}}$	$3\text{e-}3\text{s}^{-1}$
Receptor Unbinding Rate	$k_{\text{dkk}}^{\text{off}}$	$5\text{e-}2\text{s}^{-1}$
Diffusion coefficient	D_{dkk}	$1\text{e-}12\text{m}^2\text{s}^{-1}$
Contact Hopping Rate	$k_{\text{dkk}}^{\text{hop}}$	$2\text{e-}3\text{s}^{-1}$
Enter Cell Contact Rate	$k_{\text{dkk}}^{\text{in}}$	$2\text{e-}4\text{s}^{-1}$
Leave Cell Contact Rate	$k_{\text{dkk}}^{\text{out}}$	$2\text{e-}4\text{s}^{-1}$

Table A.5: Simulation parameters used in the reference simulation in Chapter 6 leading to a layer of 5-6 GS positive hepatocytes in concentric co-culture.

List of Figures

1	Length scales in Systems Biology	2
2	Iterative hypothesis-driven research	3
3	Fluorescence micrograph of endothelial cells	4
4	Cell differentiation	5
5	Goblet cells in the villus	6
1.1	Spherical tumor cells	14
1.2	Modified Hertz Potential and Derived Force	16
1.3	Trajectory of a hematopoietic CD133+ cell	17
1.4	Cell Cycle in the Model	21
2.1	Characteristics of simulated Single Cell Motion	24
2.2	Filopodia of Macrophages	25
2.3	Agreement of Langevin and the alternative filopodia approach	25
2.4	Histograms of forces for the Langevin and the filopodia approach	26
2.5	Scaling of the filopodia force with filopodia number	27
2.6	Mean square displacements of 2d simulations for varying cell densities	27
2.7	Average neighbor distance and onset of linear regime of MSD	28
2.8	Equidistant patterning by filopodia action	30
2.9	Neighbor numbers in a typical sorting process	31
2.10	Cell sorting of 3×200 cells in 2D	32
2.11	Scheme of compressed aggregate and generalized Kelvin-body model	33
2.12	Equilibrium shape and fit of compression force	34
2.13	Sensitivity of compression to model parameter	35
3.1	Differentiation Dynamics and Lineage Commitment	42
3.2	Growth dynamics of MSC populations at different oxygen tensions	44
3.3	Experimental results on chondrogenic differentiation of MSCs at 20% pO ₂	45
3.4	Properties of the chondrogenic pellet culture	46
3.5	Simulated chondrogenic differentiation of MSCs in pellet culture at 20% pO ₂	47
3.6	Lineage specification of MSCs in pellet culture at 20% pO ₂	48
3.7	Simulation of low oxygen induced de-differentiation of MSCs	49
3.8	Chondrogenic differentiation at 2% pO ₂	49
3.9	Dependence of the distribution of differentiation states on the proliferation rate	50
3.10	Dependence of the terminal differentiation on the lineage specification threshold	51
3.11	Dependence of the terminal differentiation on the lineage transition rate and oxygen consumption rate.	52
4.1	Noise profiles and typical genealogies of expanding clones	56

4.2	Individual cell dynamics	57
4.3	Simulated regeneration of the population structure	58
4.4	Clonal development during the regeneration	59
4.5	Impact of contact inhibition of growth on regeneration	60
4.6	Simulated clonal competition in the stem cell pool	61
5.1	Properties of single cell-derived MSC clones	65
5.2	MSC clones grow independently	66
5.3	Spatial heterogeneity of human MSC colonies	67
5.4	Model of population heterogeneity	68
5.5	Simulated age-structure of MSC	69
5.6	Simulated properties of single cell-derived MSC clones.	70
5.7	Simulating and monitoring <i>in vivo</i> aging	71
6.1	APC and GS activity after tamoxifen induced APC knockout	74
6.2	GS regeneration after CCl ₄ intoxication	75
6.3	GS <i>de novo</i> expression in hepatocytes in co-culture with RL-ET 14 cells	75
6.4	Simplified scheme of wnt-pathway and its feedback loop	76
6.5	Solutions of 1D activator-inhibitor PDE approach	78
6.6	Geometries used in the Simulations	80
6.7	Lattice of intercellular spaces and morphogen related processes	81
6.8	Competitive enzyme inhibition	85
6.9	Details of the dynamics of all pathway components	87
6.10	Resulting GS pattern of simulations in concentric geometry	88
6.11	GS activity in concentric colony resembling the experiment	89
6.12	GS activity in lobule-like geometry	89
6.13	Resulting pattern of random order simulations	90

List of Tables

2.1	Mean free path length and onset of linear behavior of MSD for varying cell numbers.	28
2.2	Parameter of the reference simulation.	35
6.1	Parameter of 1D PDEs for wnt and Dkk	77
A.1	Simulation Parameters used in Chapter 3	104
A.2	Simulation Parameters used in Chapter 4	105
A.3	Aging related simulation parameters used in chapter 5	106
A.4	Biophysical and lineage related parameter used in Chapter 5	106
A.5	Simulation parameters used in the reference simulation in Chapter 6	107

Bibliography

- [1] <http://www.ncbi.nlm.nih.gov/sites/entrez?db=genomeprj>.
- [2] Kandpal, R., Saviola, B., and Felton, J. (2009) The era of 'omics unlimited. *Biotechniques*, **46**, 351–2, 354–5.
- [3] Spivey, A. (2004) Systems biology: the big picture. *Environ Health Perspect*, **112**, A938–A943.
- [4] Kitano, H. (2002) Systems biology: a brief overview. *Science*, **295**, 1662–1664.
- [5] Hsu, P. W. C., Huang, H.-D., Hsu, S.-D., Lin, L.-Z., Tsou, A.-P., Tseng, C.-P., Stadler, P. F., Washietl, S., and Hofacker, I. L. (2006) mirnamap: genomic maps of microrna genes and their target genes in mammalian genomes. *Nucleic Acids Res*, **34**, D135–D139.
- [6] Bartlett, A. I. and Radford, S. E. (2009) An expanding arsenal of experimental methods yields an explosion of insights into protein folding mechanisms. *Nat Struct Mol Biol*, **16**, 582–588.
- [7] Major, F. and Griffey, R. (2001) Computational methods for rna structure determination. *Curr Opin Struct Biol*, **11**, 282–286.
- [8] Galle, J., Loeffler, M., and Drasdo, D. (2005) Modeling the effect of deregulated proliferation and apoptosis on the growth dynamics of epithelial cell populations in vitro. *Biophys J*, **88**, 62–75.
- [9] Drasdo, D. and Hoehme, S. (2005) A single-cell-based model of tumor growth in vitro: monolayers and spheroids. *Phys Biol*, **2**, 133–147.
- [10] Arai, K., Lee, K., Berthiaume, F., Tompkins, R. G., and Yarmush, M. L. (2001) Intrahepatic amino acid and glucose metabolism in a d-galactosamine-induced rat liver failure model. *Hepatology*, **34**, 360–371.
- [11] Scholz, M., Engel, C., and Loeffler, M. (2005) Modelling human granulopoiesis under poly-chemotherapy with g-csf support. *J Math Biol*, **50**, 397–439.
- [12] Kitano, H. (2002) Computational systems biology. *Nature*, **420**, 206–210.
- [13] Consortium, E. N. C. O. D. E. P. (2007) Identification and analysis of functional elements in 1% of the human genome by the encode pilot project. *Nature*, **447**, 799–816.

- [14] Burnette, W. N. (1981) "western blotting": electrophoretic transfer of proteins from sodium dodecyl sulfate–polyacrylamide gels to unmodified nitrocellulose and radiographic detection with antibody and radioiodinated protein a. *Anal Biochem*, **112**, 195–203.
- [15] Welsch, U. and Johannes, S. (2006) *Zytologie, Histologie, mikroskopische Anatomie*. Elsevier, Urban & Fischer.
- [16] Pawley, J. B. (ed.) (2006) *Handbook of Biological Confocal Microscopy*. Springer, Berlin.
- [17] Alberts, B., Johnson, A., Lewis, J., Raff, M., Roberts, K., and Walker, P. (2002) *Molecular Biology of the cell*, vol. 4. Garland Science.
- [18] Lodish, H., Berk, A., Matsudaira, P., Kaiser, C. A., Krieger, M., P., S. M., Zipursky, S. L., and Darnell, J. (2004) *Molecular Cell Biology*. W.H.Freeman and Company, fifth edn.
- [19] Sauer, B. (1998) Inducible gene targeting in mice using the cre/lox system. *Methods*, **14**, 381–392.
- [20] Hayashi, S. and McMahon, A. P. (2002) Efficient recombination in diverse tissues by a tamoxifen-inducible form of cre: a tool for temporally regulated gene activation/inactivation in the mouse. *Dev Biol*, **244**, 305–318.
- [21] Shao, J.-Y., Xu, G., and Guo, P. (2004) Quantifying cell-adhesion strength with micropipette manipulation: principle and application. *Front Biosci*, **9**, 2183–2191.
- [22] Ikai, A., Afrin, R., Sekiguchi, H., Okajima, T., Alam, M. T., and Nishida, S. (2003) Nano-mechanical methods in biochemistry using atomic force microscopy. *Curr Protein Pept Sci*, **4**, 181–193.
- [23] Guck, J., Ananthakrishnan, R., Mahmood, H., Moon, T. J., Cunningham, C. C., and Käs, J. (2001) The optical stretcher: a novel laser tool to micromanipulate cells. *Biophys J*, **81**, 767–784.
- [24] Kamanyi, A., Ngwa, W., Betz, T., Wannemacher, R., and Grill, W. (2006) Combined phase-sensitive acoustic microscopy and confocal laser scanning microscopy. *Ultrasonics*, **44 Suppl 1**, e1295–e1300.
- [25] Suresh, S., Spatz, J., Mills, J. P., Micoulet, A., Dao, M., Lim, C. T., Beil, M., and Seufferlein, T. (2005) Connections between single-cell biomechanics and human disease states: gastrointestinal cancer and malaria. *Acta Biomater*, **1**, 15–30.
- [26] Virchow, R. (1858) *Die Cellularpathologie in ihrer Begründung und in ihrer Auswirkung auf die physiologische und pathologische Gewebelehre*. Verlag A.Hirschwald, Berlin.
- [27] http://arbl.cvms.colostate.edu/hbooks/pathphys/misc_topics/goblet_pas.jpg.
- [28] de Crombrughe, B., Lefebvre, V., Behringer, R. R., Bi, W., Murakami, S., and Huang, W. (2000) Transcriptional mechanisms of chondrocyte differentiation. *Matrix Biol*, **19**, 389–394.

- [29] Sturgeon, C. M., Lai, L. C., and Duffy, M. J. (2009) Serum tumour markers: how to order and interpret them. *BMJ*, **339**, b3527.
- [30] Jenuwein, T. and Allis, C. D. (2001) Translating the histone code. *Science*, **293**, 1074–1080.
- [31] Reik, W. (2007) Stability and flexibility of epigenetic gene regulation in mammalian development. *Nature*, **447**, 425–432.
- [32] Albert, R. (2005) Scale-free networks in cell biology. *J Cell Sci*, **118**, 4947–4957.
- [33] Dalby, M. J., Gadegaard, N., Tare, R., Andar, A., Riehle, M. O., Herzyk, P., Wilkinson, C. D. W., and Oreffo, R. O. C. (2007) The control of human mesenchymal cell differentiation using nanoscale symmetry and disorder. *Nat Mater*, **6**, 997–1003.
- [34] Tuli, R., Tuli, S., Nandi, S., Huang, X., Manner, P. A., Hozack, W. J., Danielson, K. G., Hall, D. J., and Tuan, R. S. (2003) Transforming growth factor-beta-mediated chondrogenesis of human mesenchymal progenitor cells involves n-cadherin and mitogen-activated protein kinase and wnt signaling cross-talk. *J Biol Chem*, **278**, 41227–41236.
- [35] Fleming, J. L., Huang, T. H.-M., and Toland, A. E. (2008) The role of parental and grandparental epigenetic alterations in familial cancer risk. *Cancer Res*, **68**, 9116–9121.
- [36] Probst, A. V., Dunleavy, E., and Almouzni, G. (2009) Epigenetic inheritance during the cell cycle. *Nat Rev Mol Cell Biol*, **10**, 192–206.
- [37] Foty, R. A. and Steinberg, M. S. (2005) The differential adhesion hypothesis: a direct evaluation. *Dev Biol*, **278**, 255–263.
- [38] Galle, J., Hoffmann, M., and Aust, G. (2009) From single cells to tissue architecture—a bottom-up approach to modelling the spatio-temporal organisation of complex multicellular systems. *J Math Biol*, **58**, 261–283.
- [39] Galle, J., Sittig, D., Hanisch, I., Wobus, M., Wandel, E., Loeffler, M., and Aust, G. (2006) Individual cell-based models of tumor-environment interactions: Multiple effects of cd97 on tumor invasion. *Am J Pathol*, **169**, 1802–1811.
- [40] Balaban, N. Q., et al. (2001) Force and focal adhesion assembly: a close relationship studied using elastic micropatterned substrates. *Nat Cell Biol*, **3**, 466–472.
- [41] Schwarz, U. S., Erdmann, T., and Bischofs, I. B. (2006) Focal adhesions as mechanosensors: the two-spring model. *Biosystems*, **83**, 225–232.
- [42] Ingber, D. E. (2008) Tensegrity-based mechanosensing from macro to micro. *Prog Biophys Mol Biol*, **97**, 163–179.
- [43] Carragher, N. O. and Frame, M. C. (2004) Focal adhesion and actin dynamics: a place where kinases and proteases meet to promote invasion. *Trends Cell Biol*, **14**, 241–249.
- [44] Aplin, A. E., Howe, A. K., and Juliano, R. L. (1999) Cell adhesion molecules, signal transduction and cell growth. *Curr Opin Cell Biol*, **11**, 737–744.

- [45] Discher, D., Dong, C., Fredberg, J. J., Guilak, F., Ingber, D., Janmey, P., Kamm, R. D., Schmid-Schöhretznbein, G. W., and Weinbaum, S. (2009) Biomechanics: cell research and applications for the next decade. *Ann Biomed Eng*, **37**, 847–859.
- [46] Cavalcanti-Adam, E. A., Volberg, T., Micoulet, A., Kessler, H., Geiger, B., and Spatz, J. P. (2007) Cell spreading and focal adhesion dynamics are regulated by spacing of integrin ligands. *Biophys J*, **92**, 2964–2974.
- [47] Rehfeldt, F., Engler, A. J., Eckhardt, A., Ahmed, F., and Discher, D. E. (2007) Cell responses to the mechanochemical microenvironment—implications for regenerative medicine and drug delivery. *Adv Drug Deliv Rev*, **59**, 1329–1339.
- [48] Engler, A. J., Sen, S., Sweeney, H. L., and Discher, D. E. (2006) Matrix elasticity directs stem cell lineage specification. *Cell*, **126**, 677–689.
- [49] Rodan, G. A. (1997) Bone mass homeostasis and bisphosphonate action. *Bone*, **20**, 1–4.
- [50] Wang, Y. and Nathans, J. (2007) Tissue/planar cell polarity in vertebrates: new insights and new questions. *Development*, **134**, 647–658.
- [51] Ridley, A. J., Schwartz, M. A., Burridge, K., Firtel, R. A., Ginsberg, M. H., Borisy, G., Parsons, J. T., and Horwitz, A. R. (2003) Cell migration: integrating signals from front to back. *Science*, **302**, 1704–1709.
- [52] Galliot, B., Quiquand, M., Ghila, L., de Rosa, R., Miljkovic-Licina, M., and Chera, S. (2009) Origins of neurogenesis, a cnidarian view. *Dev Biol*, **332**, 2–24.
- [53] Wootton, J. T. (2001) Local interactions predict large-scale pattern in empirically derived cellular automata. *Nature*, **413**, 841–844.
- [54] Gillett, N. P. and Thompson, D. W. J. (2003) Simulation of recent southern hemisphere climate change. *Science*, **302**, 273–275.
- [55] Grimm, V., Revilla, E., Berger, U., Jeltsch, F., Mooij, W. M., Railsback, S. F., Thulke, H.-H., Weiner, J., Wiegand, T., and DeAngelis, D. L. (2005) Pattern-oriented modeling of agent-based complex systems: lessons from ecology. *Science*, **310**, 987–991.
- [56] Macy, M. W. and Willer, R. (2002) From factors to actors: Computational sociology and agent-based modeling. *Annual Review of Sociology*, **28**, 143–166.
- [57] Bonabeau, E. (2002) Agent-based modeling: methods and techniques for simulating human systems. *PNAS*, **99 Suppl 3**, 7280–7287.
- [58] Merelli, E., et al. (2007) Agents in bioinformatics, computational and systems biology. *Brief Bioinform*, **8**, 45–59.
- [59] Thorne, B. C., Bailey, A. M., and Peirce, S. M. (2007) Combining experiments with multi-cell agent-based modeling to study biological tissue patterning. *Brief Bioinform*, **8**, 245–257.
- [60] Russell, S. and Norvig, P. (1995) *Artificial Intelligence-A modern approach*. Prentice Hall.

- [61] Sick, S., Reinker, S., Timmer, J., and Schlake, T. (2006) Wnt and dkk determine hair follicle spacing through a reaction-diffusion mechanism. *Science*, **314**, 1447–1450.
- [62] Scadden, D. T. (2006) The stem-cell niche as an entity of action. *Nature*, **441**, 1075–1079.
- [63] González, P. P., Cárdenas, M., Camacho, D., Franyuti, A., Rosas, O., and Lagúnez-Otero, J. (2003) Cellulat: an agent-based intracellular signalling model. *Biosystems*, **68**, 171–185.
- [64] D’Inverno, M. and Prophet, J. (2004) *Fourth International Workshop on Network Tools and Applications, NETTAB 2004*, chap. Modelling, simulation and visualisation of adult stem cells, pp. 105–116.
- [65] Block, M., Schoell, E., and Drasdo, D. (2007) Classifying the expansion kinetics and critical surface dynamics of growing cell populations. *Phys Rev Lett*, **99**.
- [66] Glazier, J. A. and Graner, F. (1993) Simulation of the differential adhesion driven rearrangement of biological cells. *Phys Rev E*, **47**, 2128–2154.
- [67] Moreira, J. and Deutsch, A. (2005) Pigment pattern formation in zebrafish during late larval stages: A model based on local interactions. *Developmental Dynamics*, **232**, 33–42.
- [68] Galle, J., Loeffler, M., and Drasdo, D. (2003) *On the temporal-spatial organisation of epithelial cell populations in vitro*, pp. 413–420. Progetto Leonardo.
- [69] Drasdo, D. and Hoehme, S. (2003) Individual-based approaches to birth and death in avascular tumors. *Math Comp Mod*, **37**, 1163–1175.
- [70] Schaller, G. and Meyer-Hermann, M. (2005) Multicellular tumor spheroid in an off-lattice voronoi-delauny cell model. *Phys. Rev. E*, **71**, 051910.
- [71] Drasdo, D. and Loeffler, M. (2001) Individual-based models to growth and folding in one-layered tissues: intestinal crypts and early development. *Nonlinear Analysis*, **47**, 245–256.
- [72] Meineke, F. A., Potten, C. S., and Loeffler, M. (2001) Cell migration and organization in the intestinal crypt using a lattice-free model. *Cell Prolif*, **34**, 253–266.
- [73] Drasdo, D. and Forgacs, G. (2000) Modeling the interplay of generic and genetic mechanisms in cleavage, blastulation, and gastrulation. *Dev Dyn*, **219**, 182–191.
- [74] Dallon, J. C. and Othmer, H. G. (2004) How cellular movement determines the collective force generated by the dictyostelium discoideum slug. *J Theor Biol*, **231**, 203–222.
- [75] Palsson, E. (2000) A three-dimensional model of cell movement in multicellular systems. *Fut. Gen. Comp. Sys.*, **17**, 2750.
- [76] Palsson, E. and Othmer, H. G. (2000) A model for individual and collective cell movement in dictyostelium discoideum. *PNAS*, **97**, 10448–10453.
- [77] Hooke, R. (1665) *Micrographia: or, Some physiological descriptions of minute bodies made by magnifying glasses*. J. Martyn and J. Allestry.

- [78] Kölsch, V., Charest, P. G., and Firtel, R. A. (2008) The regulation of cell motility and chemotaxis by phospholipid signaling. *J Cell Sci*, **121**, 551–559.
- [79] Drubin, D. G. and Nelson, W. J. (1996) Origins of cell polarity. *Cell*, **84**, 335–344.
- [80] Gurski, L. A., Jha, A. K., Zhang, C., Jia, X., and Farach-Carson, M. C. (2009) Hyaluronic acid-based hydrogels as 3d matrices for in vitro evaluation of chemotherapeutic drugs using poorly adherent prostate cancer cells. *Biomaterials*, **30**, 6076–6085.
- [81] Radmacher, M., Fritz, M., Kacher, C. M., Cleveland, J. P., and Hansma, P. K. (1996) Measuring the viscoelastic properties of human platelets with the atomic force microscope. *Biophys J*, **70**, 556–567.
- [82] Hofmann, U. G., Rotsch, C., Parak, W. J., and Radmacher, M. (1997) Investigating the cytoskeleton of chicken cardiocytes with the atomic force microscope. *J Struct Biol*, **119**, 84–91.
- [83] Hertz, H. (1881) über die berührung fester elastischer körper. *Journal für die reine und angewandte Mathematik*, **92**, 156–171.
- [84] Landau, L. and Lifschitz, E. (1986) *Theory of Elasticity, 3.Rev.* Pergamon Press, Oxford.
- [85] Ananthkrishnan, R., Guck, J., Wottawah, F., Schinkinger, S., Lincoln, B., Romeyke, M., Moon, T., and Käs, J. (2006) Quantifying the contribution of actin networks to the elastic strength of fibroblasts. *J Theor Biol*, **242**, 502–516.
- [86] Dintwa, E., Tijskens, E., and Ramon, H. (2007) On the accuracy of the hertz model to describe the normal contact of soft elastic spheres. *Granular Matter*, **10**, 209–221.
- [87] Kasza, K. E., Rowat, A. C., Liu, J., Angelini, T. E., Brangwynne, C. P., Koenderink, G. H., and Weitz, D. A. (2007) The cell as a material. *Curr Opin Cell Biol*, **19**, 101–107.
- [88] Drasdo, D., Hoehme, S., and Block, M. (2007) On the role of physics in the growth and pattern formation of multi-cellular systems: What can we learn from individual-cell based models? *Journal of Statistical Physics*, **128**, 287–345.
- [89] Schwartz, M. A. and DeSimone, D. W. (2008) Cell adhesion receptors in mechanotransduction. *Curr Opin Cell Biol*, **20**, 551–556.
- [90] Kullander, K. and Klein, R. (2002) Mechanisms and functions of eph and ephrin signalling. *Nat Rev Mol Cell Biol*, **3**, 475–486.
- [91] Frisch, T. and Thoumine, O. (2002) Predicting the kinetics of cell spreading. *J Biomech*, **35**, 1137–1141.
- [92] Mombach and Glazier (1996) Single cell motion in aggregates of embryonic cells. *Phys Rev Lett*, **76**, 3032–3035.
- [93] Schienbein, Franke, and Gruler (1994) Random walk and directed movement: Comparison between inert particles and self-organized molecular machines. *Phys Rev E*, **49**, 5462–5471.

- [94] Dieterich, P., Klages, R., Preuss, R., and Schwab, A. (2008) Anomalous dynamics of cell migration. *PNAS*, **105**, 459–463.
- [95] Langevin, P. (1908) *Comptes Rendues*, **146**, 530.
- [96] Alison, M. and Sarraf, C. (1998) *Understanding Cancer*. Cambridge University Press, Cambridge.
- [97] Krinner, A., Zscharnack, M., Bader, A., Drasdo, D., and Galle, J. (2009) Impact of oxygen environment on mesenchymal stem cell expansion and chondrogenic differentiation. *Cell Prolif*, **42**, 471–484.
- [98] Van Kampen, N. G. (2007) *Stochastic Processes in Physics and Chemistry*. North-Holland Personal Library, Elsevier, 2nd edn.
- [99] Shemesh, T., Geiger, B., Bershadsky, A. D., and Kozlov, M. M. (2005) Focal adhesions as mechanosensors: a physical mechanism. *PNAS*, **102**, 12383–12388.
- [100] Christley, S., Alber, M. S., and Newman, S. A. (2007) Patterns of mesenchymal condensation in a multiscale, discrete stochastic model. *PLoS Comput Biol*, **3**, e76.
- [101] Hoehme, S., et al. (submitted) Cell alignment along micro-vessels as order principle to restore tissue architecture during liver regeneration: from experiment to virtual tissues and back.
- [102] Joussineau, C. D., Soulé, J., Martin, M., Anguille, C., Montcourrier, P., and Alexandre, D. (2003) Delta-promoted filopodia mediate long-range lateral inhibition in drosophila. *Nature*, **426**, 555–559.
- [103] Ruthmann, A. and Terwelp, U. (1979) Disaggregation and reaggregation of cells of the primitive maeatzoon *Trichoplax adhaerens*. *Differentiation*, **13**, 185–198.
- [104] Technau, U. and Holstein, T. W. (1992) Cell sorting during the regeneration of hydra from reaggregated cells. *Dev Biol*, **151**, 117–127.
- [105] Steinberg, M. S. (1970) Does differential adhesion govern self-assembly processes in histogenesis? equilibrium configurations and the emergence of a hierarchy among populations of embryonic cells. *J Exp Zool*, **173**, 395–433.
- [106] Beysens, D., Forgacs, G., and Glazier, J. (2000) Cell sorting is analogous to phase ordering in fluids. *PNAS*, **97**, 9467.
- [107] Foty, R. A., Pflieger, C. M., Forgacs, G., and Steinberg, M. S. (1996) Surface tensions of embryonic tissues predict their mutual envelopment behavior. *Development*, **122**, 1611–1620.
- [108] Forgacs, G., Foty, R. A., Shafir, Y., and Steinberg, M. S. (1998) Viscoelastic properties of living embryonic tissues: a quantitative study. *Biophys J*, **74**, 2227–2234.
- [109] Foty, R. A., Forgacs, G., Pflieger, C. M., and Steinberg, M. S. (1994) Liquid properties of embryonic tissues: Measurement of interfacial tensions. *Phys Rev Lett*, **72**, 2298–2301.
- [110] Graner, F. and Glazier, J. A. (1992) Simulation of biological cell sorting using a two-dimensional extended potts model. *Phys Rev Lett*, **69**, 2013–2016.

- [111] Mombach, Glazier, Raphael, and Zajac (1995) Quantitative comparison between differential adhesion models and cell sorting in the presence and absence of fluctuations. *Phys Rev Lett*, **75**, 2244–2247.
- [112] Jiang, Y., Levine, H., and Glazier, J. (1998) Possible cooperation of differential adhesion and chemotaxis in mound formation of dictyostelium. *Biophys J*, **75**, 2615–2625.
- [113] Mombach, J., Robert, D., Graner, F., Gillet, G., Thomas, G., Idiart, M., and Rieu, J.-P. (2005) Rounding of aggregates of biological cells: Experiments and simulations. *Physica A*, **352**, 525–534.
- [114] Ramis-Conde, I., Drasdo, D., Anderson, A. R. A., and Chaplain, M. A. J. (2008) Modeling the influence of the e-cadherin-beta-catenin pathway in cancer cell invasion: a multiscale approach. *Biophys J*, **95**, 155–165.
- [115] Roeder, I., Horn, M., Glauche, I., Hochhaus, A., Mueller, M. C., and Loeffler, M. (2006) Dynamic modeling of imatinib-treated chronic myeloid leukemia: functional insights and clinical implications. *Nat Med*, **12**, 1181–1184.
- [116] Guptasarma, P. (1995) Does replication-induced transcription regulate synthesis of the myriad low copy number proteins of escherichia coli? *Bioessays*, **17**, 987–997.
- [117] McAdams, H. H. and Arkin, A. (1999) It’s a noisy business! genetic regulation at the nanomolar scale. *Trends Genet*, **15**, 65–69.
- [118] Elowitz, M. B., Levine, A. J., Siggia, E. D., and Swain, P. S. (2002) Stochastic gene expression in a single cell. *Science*, **297**, 1183–1186.
- [119] Korobkova, E., Emonet, T., Vilar, J. M. G., Shimizu, T. S., and Cluzel, P. (2004) From molecular noise to behavioural variability in a single bacterium. *Nature*, **428**, 574–578.
- [120] Chang, H. H., Hemberg, M., Barahona, M., Ingber, D. E., and Huang, S. (2008) Transcriptome-wide noise controls lineage choice in mammalian progenitor cells. *Nature*, **453**, 544–547.
- [121] Raser, J. M. and O’Shea, E. K. (2005) Noise in gene expression: origins, consequences, and control. *Science*, **309**, 2010–2013.
- [122] Zwaka, T. P. (2006) Keeping the noise down in es cells. *Cell*, **127**, 1301–1302.
- [123] Hunziker, E. B. (2002) Articular cartilage repair: basic science and clinical progress. a review of the current status and prospects. *Osteoarthritis Cartilage*, **10**, 432–463.
- [124] Song, L., Webb, N. E., Song, Y., and Tuan, R. S. (2006) Identification and functional analysis of candidate genes regulating mesenchymal stem cell self-renewal and multipotency. *Stem Cells*, **24**, 1707–1718.
- [125] Schulz, R. M. and Bader, A. (2007) Cartilage tissue engineering and bioreactor systems for the cultivation and stimulation of chondrocytes. *Eur Biophys J*, **36**, 539–568.
- [126] Heng, B. C., Cao, T., and Lee, E. H. (2004) Directing stem cell differentiation into the chondrogenic lineage in vitro. *Stem Cells*, **22**, 1152–1167.

- [127] Cross, M., Alt, R., and Niederwieser, D. (2008) The case for a metabolic stem cell niche. *Cells Tissues Organs*, **188**, 150–159.
- [128] D'Ippolito, G., Diabira, S., Howard, G. A., Roos, B. A., and Schiller, P. C. (2006) Low oxygen tension inhibits osteogenic differentiation and enhances stemness of human MIAMI cells. *Bone*, **39**, 513–522.
- [129] Ren, H., et al. (2006) Proliferation and differentiation of bone marrow stromal cells under hypoxic conditions. *Biochem. Biophys. Res Commun.*, **347**(1), 12–21.
- [130] Lennon, D. P., Edmison, J. M., and Caplan, A. I. (2001) Cultivation of rat marrow-derived mesenchymal stem cells in reduced oxygen tension: effects on in vitro and in vivo osteochondrogenesis. *J Cell Physiol*, **187**, 345–355.
- [131] Grayson, W. L., Zhao, F., Izadpanah, R., Bunnell, B., and Ma, T. (2006) Effects of hypoxia on human mesenchymal stem cell expansion and plasticity in 3d constructs. *J Cell Physiol*, **207**, 331–339.
- [132] Martin-Rendon, E., et al. (2007) Transcriptional profiling of human cord blood cd133+ and cultured bone marrow mesenchymal stem cells in response to hypoxia. *Stem Cells*, **25**, 1003–1012.
- [133] Xu, Y., Malladi, P., Chiou, M., Bekerman, E., Giaccia, A. J., and Longaker, M. T. (2007) In vitro expansion of adipose-derived adult stromal cells in hypoxia enhances early chondrogenesis. *Tissue Eng*, **13**, 2981–2993.
- [134] Malladi, P., Xu, Y., Chiou, M., Giaccia, A. J., and Longaker, M. T. (2006) Effect of reduced oxygen tension on chondrogenesis and osteogenesis in adipose-derived mesenchymal cells. *Am J Physiol Cell Physiol*, **290**, C1139–C1146.
- [135] Wang, D. W., Fermor, B., Gimble, J. M., Awad, H. A., and Guilak, F. (2005) Influence of oxygen on the proliferation and metabolism of adipose derived adult stem cells. *J Cell Physiol*, **204**, 184–191.
- [136] Sengers, B. G., Taylor, M., Please, C. P., and Oreffo, R. O. C. (2007) Computational modelling of cell spreading and tissue regeneration in porous scaffolds. *Biomaterials*, **28**, 1926–1940.
- [137] Deasy, B. M., Jankowski, R. J., Payne, T. R., Cao, B., Goff, J. P., Greenberger, J. S., and Huard, J. (2003) Modeling stem cell population growth: incorporating terms for proliferative heterogeneity. *Stem Cells*, **21**, 536–545.
- [138] Lemon, G., Waters, S. L., Rose, F. R., and King, J. R. (2007) Mathematical modelling of human mesenchymal stem cell proliferation and differentiation inside artificial porous scaffolds. *Journal of Theoretical Biology*, **249**, 543–553.
- [139] Hoffmann, M., Chang, H. H., Huang, S., Ingber, D. E., Loeffler, M., and Galle, J. (2008) Noise-driven stem cell and progenitor population dynamics. *PLoS ONE*, **3**, e2922.
- [140] Glauche, I., Cross, M., Loeffler, M., and Roeder, I. (2007) Lineage specification of hematopoietic stem cells: mathematical modeling and biological implications. *Stem Cells*, **25**, 1791–1799.

- [141] Loeffler, M. and Roeder, I. (2004) Conceptual models to understand tissue stem cell organization. *Curr Opin Hematol*, **11**, 81–87.
- [142] Lécuyer, E., Yoshida, H., Parthasarathy, N., Alm, C., Babak, T., Cerovina, T., Hughes, T. R., Tomancak, P., and Krause, H. M. (2007) Global analysis of mrna localization reveals a prominent role in organizing cellular architecture and function. *Cell*, **131**, 174–187.
- [143] Brown, G., Drayson, M. T., Durham, J., Toellner, K. M., Hughes, P. J., Choudhry, M. A., Taylor, D. R., Bird, R., and Michell, R. H. (2002) H160 cells halted in g1 or s phase differentiate normally. *Exp Cell Res*, **281**, 28–38.
- [144] Lefebvre, V. and Smits, P. (2005) Transcriptional control of chondrocyte fate and differentiation. *Birth Defects Res C Embryo Today*, **75**, 200–212.
- [145] Efroni, S., et al. (2008) Global transcription in pluripotent embryonic stem cells. *Cell Stem Cell*, **2**, 437–447.
- [146] Malda, J., Rouwkema, J., Martens, D. E., Comte, E. P. L., Kooy, F. K., Tramper, J., van Blitterswijk, C. A., and Riesle, J. (2004) Oxygen gradients in tissue-engineered pegt/pbt cartilaginous constructs: measurement and modeling. *Biotechnol Bioeng*, **86**, 9–18.
- [147] Zhao, F., Pathi, P., Grayson, W., Xing, Q., Locke, B. R., and Ma, T. (2005) Effects of oxygen transport on 3-d human mesenchymal stem cell metabolic activity in perfusion and static cultures: experiments and mathematical model. *Biotechnol Prog*, **21**, 1269–1280.
- [148] Zscharnack, M., Poesel, C., Galle, J., and Bader, A. (2009) Low oxygen expansion improves subsequent chondrogenesis of ovine bone-marrow-derived mesenchymal stem cells in collagen type i hydrogel. *Cells Tissues Organs*, **190**, 81–93.
- [149] Nehring, D., Adamietz, P., Meenen, N. M., and Pörtner, R. (2007) Perfusion cultures and modelling of oxygen uptake with three-dimensional chondrocyte pellets. *Biotechnology Techniques*, **13**, 701–706.
- [150] Tsuchiya, H., Kitoh, H., Sugiura, F., and Ishiguro, N. (2003) Chondrogenesis enhanced by overexpression of sox9 gene in mouse bone marrow-derived mesenchymal stem cells. *Biochem Biophys Res Commun*, **301**, 338–343.
- [151] Grimshaw, M. J. and Mason, R. M. (2001) Modulation of bovine articular chondrocyte gene expression in vitro by oxygen tension. *Osteoarthritis Cartilage*, **9**, 357–364.
- [152] O’Driscoll, S. W., Fitzsimmons, J. S., and Commisso, C. N. (1997) Role of oxygen tension during cartilage formation by periosteum. *J Orthop Res*, **15**, 682–687.
- [153] Fink, T., Abildtrup, L., Fogd, K., Abdallah, B. M., Kassem, M., Ebbesen, P., and Zachar, V. (2004) Induction of adipocyte-like phenotype in human mesenchymal stem cells by hypoxia. *Stem Cells*, **22**, 1346–1355.
- [154] Potier, E., Ferreira, E., Andriamanalijaona, R., Pujol, J.-P., Oudina, K., Logeart-Avramoglou, D., and Petite, H. (2007) Hypoxia affects mesenchymal stromal cell osteogenic differentiation and angiogenic factor expression. *Bone*, **40**, 1078–1087.

- [155] Sengers, B. G., Donkelaar, C. C. V., Oomens, C. W. J., and Baaijens, F. P. T. (2004) The local matrix distribution and the functional development of tissue engineered cartilage, a finite element study. *Ann Biomed Eng*, **32**, 1718–1727.
- [156] Zon, L. I. (2008) Intrinsic and extrinsic control of haematopoietic stem-cell self-renewal. *Nature*, **453**, 306–313.
- [157] Okazaki, K. and Maltepe, E. (2006) Oxygen, epigenetics and stem cell fate. *Regen Med*, **1**, 71–83.
- [158] Chang, H. H., Oh, P. Y., Ingber, D. E., and Huang, S. (2006) Multistable and multistep dynamics in neutrophil differentiation. *BMC Cell Biol*, **7**, 11.
- [159] van Kampen, N. (2004) *Stochastic processes in physics and chemistry*. Elsevier.
- [160] Eilken, H. M., Nishikawa, S.-I., and Schroeder, T. (2009) Continuous single-cell imaging of blood generation from haemogenic endothelium. *Nature*, **457**, 896–900.
- [161] Lo Celso, C., Fleming, H. E., Wu, J. W., Zhao, C. X., Miake-Lye, S., Fujisaki, J., Côté, D., Rowe, D. W., Lin, C. P., and Scadden, D. T. (2009) Live-animal tracking of individual haematopoietic stem/progenitor cells in their niche. *Nature*, **457**, 92–96.
- [162] DeLise, A. M., Fischer, L., and Tuan, R. S. (2000) Cellular interactions and signaling in cartilage development. *Osteoarthritis Cartilage*, **8**, 309–334.
- [163] Reya, T., Morrison, S. J., Clarke, M. F., and Weissman, I. L. (2001) Stem cells, cancer, and cancer stem cells. *Nature*, **414**, 105–111.
- [164] Loeffler, M. and Roeder, I. (2002) Tissue stem cells: definition, plasticity, heterogeneity, self-organization and models—a conceptual approach. *Cells Tissues Organs*, **171**, 8–26.
- [165] Stolzing, A. and Scutt, A. (2006) Age-related impairment of mesenchymal progenitor cell function. *Aging Cell*, **5**, 213–224.
- [166] Gregory, C. A., Ylostalo, J., and Prockop, D. J. (2005) Adult bone marrow stem/progenitor cells (mscs) are preconditioned by microenvironmental "niches" in culture: a two-stage hypothesis for regulation of msc fate. *Sci STKE*, **2005**, pe37.
- [167] Komori, T. (2006) Regulation of osteoblast differentiation by transcription factors. *J Cell Biochem*, **99**, 1233–1239.
- [168] Brooke, G., et al. (2007) Therapeutic applications of mesenchymal stromal cells. *Semin Cell Dev Biol*, **18**, 846–858.
- [169] Dazzi, F. and Horwood, N. J. (2007) Potential of mesenchymal stem cell therapy. *Curr Opin Oncol*, **19**, 650–655.
- [170] D'Ippolito, G., Diabira, S., Howard, G. A., Menei, P., Roos, B. A., and Schiller, P. C. (2004) Marrow-isolated adult multilineage inducible (miami) cells, a unique population of postnatal young and old human cells with extensive expansion and differentiation potential. *J Cell Sci*, **117**, 2971–2981.
- [171] Sorrentino, A., Ferracin, M., Castelli, G., Biffoni, M., Tomaselli, G., Baiocchi, M., Fatica, A., Negrini, M., Peschle, C., and Valtieri, M. (2008) Isolation and characterization of cd146+ multipotent mesenchymal stromal cells. *Exp Hematol*, **36**, 1035–1046.

- [172] Suva, D., Garavaglia, G., Menetrey, J., Chapuis, B., Hoffmeyer, P., Bernheim, L., and Kindler, V. (2004) Non-hematopoietic human bone marrow contains long-lasting, pluripotential mesenchymal stem cells. *J Cell Physiol*, **198**, 110–118.
- [173] Sethe, S., Scutt, A., and Stolzing, A. (2006) Aging of mesenchymal stem cells. *Ageing Res Rev*, **5**, 91–116.
- [174] Rombouts, W. J. C. and Ploemacher, R. E. (2003) Primary murine msc show highly efficient homing to the bone marrow but lose homing ability following culture. *Leukemia*, **17**, 160–170.
- [175] Stolzing, A., Jones, E., McGonagle, D., and Scutt, A. (2008) Age-related changes in human bone marrow-derived mesenchymal stem cells: consequences for cell therapies. *Mech Ageing Dev*, **129**, 163–173.
- [176] Wagner, W., et al. (2008) Replicative senescence of mesenchymal stem cells: a continuous and organized process. *PLoS One*, **3**, e2213.
- [177] Kretlow, J. D., Jin, Y.-Q., Liu, W., Zhang, W. J., Hong, T.-H., Zhou, G., Baggett, L. S., Mikos, A. G., and Cao, Y. (2008) Donor age and cell passage affects differentiation potential of murine bone marrow-derived stem cells. *BMC Cell Biol*, **9**, 60.
- [178] Wagner, W., et al. (2009) Aging and replicative senescence have related effects on human stem and progenitor cells. *PLoS One*, **4**, e5846.
- [179] Sharpless, N. E. and DePinho, R. A. (2007) How stem cells age and why this makes us grow old. *Nat Rev Mol Cell Biol*, **8**, 703–713.
- [180] Ruzankina, Y. and Brown, E. J. (2007) Relationships between stem cell exhaustion, tumour suppression and ageing. *Br J Cancer*, **97**, 1189–1193.
- [181] Fehrer, C., Brunauer, R., Laschober, G., Unterluggauer, H., Reitingner, S., Kloss, F., Gilly, C., Gassner, R., and Lepperdinger, G. (2007) Reduced oxygen tension attenuates differentiation capacity of human mesenchymal stem cells and prolongs their lifespan. *Ageing Cell*, **6**, 745–757.
- [182] Serakinci, N., Guldborg, P., Burns, J. S., Abdallah, B., Schrødder, H., Jensen, T., and Kassem, M. (2004) Adult human mesenchymal stem cell as a target for neoplastic transformation. *Oncogene*, **23**, 5095–5098.
- [183] Kolf, C. M., Cho, E., and Tuan, R. S. (2007) Mesenchymal stromal cells. biology of adult mesenchymal stem cells: regulation of niche, self-renewal and differentiation. *Arthritis Res Ther*, **9**, 204.
- [184] Zhou, S., Greenberger, J. S., Epperly, M. W., Goff, J. P., Adler, C., Leboff, M. S., and Glowacki, J. (2008) Age-related intrinsic changes in human bone-marrow-derived mesenchymal stem cells and their differentiation to osteoblasts. *Ageing Cell*, **7**, 335–343.
- [185] Lapi, S., et al. (2008) Different media and supplements modulate the clonogenic and expansion properties of rabbit bone marrow mesenchymal stem cells. *BMC Res Notes*, **1**, 53.
- [186] Oakley, E. J. and Zant, G. V. (2007) Unraveling the complex regulation of stem cells: implications for aging and cancer. *Leukemia*, **21**, 612–621.

- [187] Orford, K., Kharchenko, P., Lai, W., Dao, M. C., Worhunsky, D. J., Ferro, A., Janzen, V., Park, P. J., and Scadden, D. T. (2008) Differential h3k4 methylation identifies developmentally poised hematopoietic genes. *Dev Cell*, **14**, 798–809.
- [188] Tan, J., Huang, H., Huang, W., Li, L., Guo, J., Huang, B., and Lu, J. (2008) The genomic landscapes of histone h3-lys9 modifications of gene promoter regions and expression profiles in human bone marrow mesenchymal stem cells. *J Genet Genomics*, **35**, 585–593.
- [189] Noer, A., Lindeman, L. C., and Collas, P. (2009) Histone h3 modifications associated with differentiation and long-term culture of mesenchymal adipose stem cells. *Stem Cells Dev*, **18**, 725–736.
- [190] Sinclair, D. A. and Oberdoerffer, P. (2009) The ageing epigenome: damaged beyond repair? *Ageing Res Rev*, **8**, 189–198.
- [191] Dröge, W. (2003) Oxidative stress and aging. *Adv Exp Med Biol*, **543**, 191–200.
- [192] Aguiari, P., et al. (2008) High glucose induces adipogenic differentiation of muscle-derived stem cells. *PNAS*, **105**, 1226–1231.
- [193] Wang, N., Xie, K., Huo, S., Zhao, J., Zhang, S., and Miao, J. (2007) Suppressing phosphatidylcholine-specific phospholipase c and elevating ros level, nadph oxidase activity and rb level induced neuronal differentiation in mesenchymal stem cells. *J Cell Biochem*, **100**, 1548–1557.
- [194] Lin, T.-M., Tsai, J.-L., Lin, S.-D., Lai, C.-S., and Chang, C.-C. (2005) Accelerated growth and prolonged lifespan of adipose tissue-derived human mesenchymal stem cells in a medium using reduced calcium and antioxidants. *Stem Cells Dev*, **14**, 92–102.
- [195] Sekiya, I., Larson, B. L., Smith, J. R., Pochampally, R., Cui, J.-G., and Prockop, D. J. (2002) Expansion of human adult stem cells from bone marrow stroma: conditions that maximize the yields of early progenitors and evaluate their quality. *Stem Cells*, **20**, 530–541.
- [196] Clevers, H. (2006) Wnt/beta-catenin signaling in development and disease. *Cell*, **127**, 469–480.
- [197] Nusse, R. (2005) Wnt signaling in disease and in development. *Cell Res*, **15**, 28–32.
- [198] Nusse, R. (2008) Wnt signaling and stem cell control. *Cell Res*, **18**, 523–527.
- [199] Cadigan, K. M. (2008) Wnt-beta-catenin signaling. *Curr Biol*, **18**, R943–R947.
- [200] Naito, A. T., Shiojima, I., Akazawa, H., Hidaka, K., Morisaki, T., Kikuchi, A., and Komuro, I. (2006) Developmental stage-specific biphasic roles of wnt/beta-catenin signaling in cardiomyogenesis and hematopoiesis. *PNAS*, **103**, 19812–19817.
- [201] Ueno, S., Weidinger, G., Osugi, T., Kohn, A. D., Golob, J. L., Pabon, L., Reinecke, H., Moon, R. T., and Murry, C. E. (2007) Biphasic role for wnt/beta-catenin signaling in cardiac specification in zebrafish and embryonic stem cells. *PNAS*, **104**, 9685–9690.
- [202] Lee, E., Salic, A., Krüger, R., Heinrich, R., and Kirschner, M. W. (2003) The roles of apc and axin derived from experimental and theoretical analysis of the wnt pathway. *PLoS Biol*, **1**, E10.

- [203] Gebhardt, R., Baldysiak-Figiel, A., Krügel, V., Ueberham, E., and Gaunitz, F. (2007) Hepatocellular expression of glutamine synthetase: an indicator of morphogen actions as master regulators of zonation in adult liver. *Prog Histochem Cytochem*, **41**, 201–266.
- [204] Benhamouche, S., et al. (2006) Apc tumor suppressor gene is the "zonation-keeper" of mouse liver. *Dev Cell*, **10**, 759–770.
- [205] Burke, Z. D., Reed, K. R., Pheese, T. J., Sansom, O. J., Clarke, A. R., and Tosh, D. (2009) Liver zonation occurs through a beta-catenin-dependent, c-myc-independent mechanism. *Gastroenterology*, **136**, 2316–2324.e1–3.
- [206] Badger, D. A., Sauer, J. M., Hoglen, N. C., Jolley, C. S., and Sipes, I. G. (1996) The role of inflammatory cells and cytochrome p450 in the potentiation of ccl4-induced liver injury by a single dose of retinol. *Toxicol Appl Pharmacol*, **141**, 507–519.
- [207] Schöls, L., Mecke, D., and Gebhardt, R. (1990) Reestablishment of the heterogeneous distribution of hepatic glutamine synthetase during regeneration after ccl4-intoxication. *Histochemistry*, **94**, 49–54.
- [208] Schrode, W., Mecke, D., and Gebhardt, R. (1990) Induction of glutamine synthetase in periportal hepatocytes by cocultivation with a liver epithelial cell line. *Eur J Cell Biol*, **53**, 35–41.
- [209] Gebhardt, R., pers.comm.
- [210] Zeng, X., et al. (2008) Initiation of wnt signaling: control of wnt coreceptor lrp6 phosphorylation/activation via frizzled, dishevelled and axin functions. *Development*, **135**, 367–375.
- [211] González-Sancho, J. M., Aguilera, O., García, J. M., Pendás-Franco, N., Pena, C., Cal, S., de Herreros, A. G., Bonilla, F., and Munoz, A. (2005) The wnt antagonist dickkopf-1 gene is a downstream target of beta-catenin/tcf and is downregulated in human colon cancer. *Oncogene*, **24**, 1098–1103.
- [212] Bafico, A., Liu, G., Yaniv, A., Gazit, A., and Aaronson, S. A. (2001) Novel mechanism of wnt signalling inhibition mediated by dickkopf-1 interaction with lrp6/arrow. *Nat Cell Biol*, **3**, 683–686.
- [213] Neumann, S., Coudreuse, D. Y. M., van der Westhuyzen, D. R., Eckhardt, E. R. M., Korswagen, H. C., Schmitz, G., and Sprong, H. (2009) Mammalian wnt3a is released on lipoprotein particles. *Traffic*, **10**, 334–343.
- [214] Lin, X. (2004) Functions of heparan sulfate proteoglycans in cell signaling during development. *Development*, **131**, 6009–6021.
- [215] Lakkaraju, A. and Rodriguez-Boulan, E. (2008) Itinerant exosomes: emerging roles in cell and tissue polarity. *Trends Cell Biol*, **18**, 199–209.
- [216] Zhu, Y., et al. (2009) Human mesenchymal stem cells inhibit cancer cell proliferation by secreting dkk-1. *Leukemia*, **23**, 925–933.
- [217] Deb, A., Davis, B. H., Guo, J., Ni, A., Huang, J., Zhang, Z., Mu, H., and Dzau, V. J. (2008) Sfrp2 regulates cardiomyogenic differentiation by inhibiting a positive transcriptional autofeedback loop of wnt3a. *Stem Cells*, **26**, 35–44.

- [218] Braeuning, A., Menzel, M., Kleinschnitz, E.-M., Harada, N., Tamai, Y., Köhle, C., Buchmann, A., and Schwarz, M. (2007) Serum components and activated ha-ras antagonize expression of perivenous marker genes stimulated by beta-catenin signaling in mouse hepatocytes. *FEBS J*, **274**, 4766–4777.
- [219] Kim, D., Rath, O., Kolch, W., and Cho, K.-H. (2007) A hidden oncogenic positive feedback loop caused by crosstalk between wnt and erk pathways. *Oncogene*, **26**, 4571–4579.
- [220] Bollenbach, T., Kruse, K., Pantazis, P., González-Gaitán, M., and Jülicher, F. (2007) Morphogen transport in epithelia. *Phys Rev E*, **75**, 011901.
- [221] Höhme, S., Hengstler, J., Brulport, M., Schäfer, M., A., B., Gebhardt, R., and Drasdo, D. (2007) Mathematical modelling of liver regeneration after intoxication with ccl4. *Chemico-Biological Interaction*, **168**, 74–93.
- [222] Bisswanger, H. (2002) *Enzyme Kinetics: Principles and Methods*. Wiley-VCH.
- [223] Gebhardt, R. and Mecke, D. (1983) Heterogeneous distribution of glutamine synthetase among rat liver parenchymal cells in situ and in primary culture. *EMBO J*, **2**, 567–570.
- [224] Burke, Z. D., Thowfeequ, S., and Tosh, D. (2006) Liver specification: a new role for wnts in liver development. *Curr Biol*, **16**, R688–R690.
- [225] McLin, V. A., Rankin, S. A., and Zorn, A. M. (2007) Repression of wnt/beta-catenin signaling in the anterior endoderm is essential for liver and pancreas development. *Development*, **134**, 2207–2217.
- [226] Matsumoto, K., Miki, R., Nakayama, M., Tatsumi, N., and Yokouchi, Y. (2008) Wnt9a secreted from the walls of hepatic sinusoids is essential for morphogenesis, proliferation, and glycogen accumulation of chick hepatic epithelium. *Dev Biol*, **319**, 234–247.
- [227] Aulehla, A. and Pourquié, O. (2008) Oscillating signaling pathways during embryonic development. *Curr Opin Cell Biol*, **20**, 632–637.
- [228] Aulehla, A., Wiegraebe, W., Baubet, V., Wahl, M. B., Deng, C., Taketo, M., Lewandoski, M., and Pourquié, O. (2008) A beta-catenin gradient links the clock and wave-front systems in mouse embryo segmentation. *Nat Cell Biol*, **10**, 186–193.
- [229] Tolwinski, N. S. and Wieschaus, E. (2001) Armadillo nuclear import is regulated by cytoplasmic anchor axin and nuclear anchor dtcf/pan. *Development*, **128**, 2107–2117.
- [230] Zaret, K. S. (2002) Regulatory phases of early liver development: paradigms of organogenesis. *Nat Rev Genet*, **3**, 499–512.
- [231] Schenk, O. and Gärtner, K. (2006) On fast factorization pivoting methods for sparse symmetric indefinite systems. *Electronic Transactions on Numerical Analysis*, **23**, 158–179.
- [232] Schenk, O. and Gärtner, K. (2004) Solving unsymmetric sparse systems of linear equations with pardiso. *Journal of Future Generation Computer Systems*, **20**, 475–487.

- [233] Dobson, K. R., Reading, L., Haberey, M., Marine, X., and Scutt, A. (1999) Centrifugal isolation of bone marrow from bone: an improved method for the recovery and quantitation of bone marrow osteoprogenitor cells from rat tibiae and femuræ. *Calcif Tissue Int*, **65**, 411–413.
- [234] Kuznetsov, S. A., Krebsbach, P. H., Satomura, K., Kerr, J., Riminucci, M., Benayahu, D., and Robey, P. G. (1997) Single-colony derived strains of human marrow stromal fibroblasts form bone after transplantation in vivo. *J Bone Miner Res*, **12**, 1335–1347.
- [235] Scutt, A. and Bertram, P. (1995) Bone marrow cells are targets for the anabolic actions of prostaglandin e2 on bone: induction of a transition from nonadherent to adherent osteoblast precursors. *J Bone Miner Res*, **10**, 474–487.
- [236] Mackay, A. M., Beck, S. C., Murphy, J. M., Barry, F. P., Chichester, C. O., and Pittenger, M. F. (1998) Chondrogenic differentiation of cultured human mesenchymal stem cells from marrow. *Tissue Eng*, **4**, 415–428.
- [237] Yoo, J. U., Barthel, T. S., Nishimura, K., Solchaga, L., Caplan, A. I., Goldberg, V. M., and Johnstone, B. (1998) The chondrogenic potential of human bone-marrow-derived mesenchymal progenitor cells. *J Bone Joint Surg Am*, **80**, 1745–1757.
- [238] Pan, W., Petersen, E., Cai, N., Ma, G., Lee, J. R., Feng, Z., Liao, K., and Leong, K. (2005) Viscoelastic properties of human mesenchymal stem cells. *Conf Proc IEEE Eng Med Biol Soc*, **5**, 4854–4857.
- [239] Wu, J. Z. and Herzog, W. (2002) Elastic anisotropy of articular cartilage is associated with the microstructures of collagen fibers and chondrocytes. *J Biomech*, **35**, 931–942.

Curriculum Vitae

Personal Details

Name	Axel Krinner
Mail	Fockestr. 21, 04275 Leipzig
Email	krinner@izbi.uni-leipzig.de
Birthday and place	11.11.1976, Munich, Germany
Nationality	German
Family status	single

Education

1982-1986	Primary School Herrenschole, Munich
1986-1995	Secondary School, Luitpold-Gymnasium, Munich

Scientific Education

1997-1999	Study of Physics, University of Leipzig
1999-2000	Study of Physics, Technical University of Vienna
2000-2004	Study of Physics, University of Leipzig
09/2004	Certificate: Diploma Physics Diploma Thesis: Nature of Phase Transitions in a Generalized Complex Ginzburg-Landau Model.
12/2004-01/2005	PhD Scholarship within the post graduate programme "Diffusion in porous Materials" at Universität of Leipzig.
02/2005-03/2005	Research Assistant at the University of Leipzig.
04/2005-02/2008	Research Assistant at the Interdisciplinary Center for Bioinformatics, University of Leipzig.
03/2008-06/2008	Research Assistant at the Leibniz Research Center for Working Environment and Human Factors, Technical University of Dortmund
07/2008-06/2009	Research Assistant at the Interdisciplinary Center for Bioinformatics, University of Leipzig.
since 07/2009	Research Assistant at the Institute for Medical Informatics, Statistics and Epidemiology, University of Leipzig.

Languages

ANSI C / C++, Perl, Sed, Awk, Commandline basierte Hilfssprachen/programme, LaTeX

English, Spanish, Basic French

Selbständigkeitserklärung nach §7 der Prüfungsordnung

Hiermit erkläre ich, die vorliegende Dissertation selbständig und ohne unzulässige fremde Hilfe angefertigt zu haben. Ich habe keine anderen als die angeführten Quellen und Hilfsmittel benutzt und sämtliche Textstellen, die wörtlich oder sinngemäß aus veröffentlichten oder unveröffentlichten Schriften entnommen wurden, und alle Angaben, die auf mündlichen Auskünften beruhen, als solche kenntlich gemacht. Ebenfalls sind alle von anderen Personen bereitgestellten Materialien oder erbrachten Dienstleistungen als solche gekennzeichnet.

Leipzig, den 3. Februar 2010

Axel Krinner